DIPLOMA THESIS

Nanoscale studies of ferroptosis-induced phospholipid peroxidation in membranes of T-cell acute lymphoblastic leukaemia cells

submitted by

Lena Neubauer

11810831

under supervision of:

Univ.Prof. Dipl.-Ing. Dr.techn. Bernhard Lendl
Associate Prof., PhD Ariane Deniset-Besseau
Univ.Ass. Dipl.-Ing. Dr.techn. Georg Ramer

executed at

Institut de Chimie Physique, Université Paris Saclay and
Institute of Chemical Technologies and Analytics, Technical University of Vienna

Vienna, July, 2024

[redacted]

Lena Neubauer

Statutory Declaration

I hereby declare that I have completed this diploma thesis independently and that no other aids have been used than those I have cited as sources. Literal and analogous quotations have been marked accordingly.

Vienna, July, 2024

Lena Neubauer

Acknowledgement

First of all, I would like to thank Ariane Deniset-Besseau for accepting me at ICP in Orsay. Without her support during the planning phase as well as the experimental realisation and writing of the thesis this process wouldn't have been as coordinated. This master study abroad also wouldn't have been possible without my supervisors in Vienna, Bernhard Lendl and Georg Ramer and their initial proposal to go to France.

My thanks also go to Alexander Dazzi and Jeremie Mathurin for their expertise whenever I encountered measurement problems and their impromptu lectures on the theoretical background of AFM-IR. I am also very grateful for the support of Guillaume Andrieu, Martina Failla and Jerome Doss from research institute INSERM (Hospital Necker) for the provision of the biological sample material as well as their explanations regarding all my biomedical questions.

I would also like to thank my colleagues in both the ICP and the CAVS research group for the time we spent together. Special thanks to Pily for her help during the organisation of this stay abroad.

This diploma thesis has received financial support provided by the European Union's Horizon 2020 research and innovation programme under Grant No. 953234 (Tumor-LN-oC) and from European Union's Erasmus+ internship program.

Last but not least, I want to thank my family and friends for their help and support during my bachelor and master studies.

Abstract

T-cell acute leukaemia (T-ALL) is a haematological cancer disease. In the last decade survival rates significantly improved, but still cancer cells resistant to treatment pose serious problems leading to drastically reduced overall survival rates under 25%. Novel treatment options are therefore essential. The research institute of hospital Necker is working on a novel approach to reach resistant cells. They propose to increase the production of reactive oxygen species inside the resistant cancer cells to induce a specific cell death called ferroptosis. This regulated, non-apoptotic cell death is initiated by iron-mediated phospholipid peroxidation through increased reactive oxygen radical production, via various cell metabolism pathways. By artificially increasing the ROS production in those T-cells via exogenous initiator molecules, the utilisation of this mechanism to eliminate refractory cancer cells could represent a new generation of cancer therapeutics. This strategy is promising but yet not well understood.

The introduction of atomic force microscopy coupled with infrared spectroscopy (AFM-IR) allows the chemical identification of these treatment-dependent membrane changes in mid-IR spectral at nanoscale. In this work, a protocol for the optimisation of the sample preparation, the acquisition of global IR signatures of the peroxidation process by O-PTIR and the investigation of membrane degradation via AFM-IR was established. The methodology protocol was validated on two immortal cell lines, spiked with two known ferroptosis-inducing reagents to induce cell death. Hotspots responding to a characteristic vibration band for phospholipid peroxidation were identified on the model T-ALL cells. Local spectra on these prominent points demonstrated several IR bands, assignable to different oxidised phospholipid peroxidation end products in the membranes.

Zusammenfassung

Akute T-Zell-Leukämie (T-ALL) ist eine hämatologische Krebserkrankung. In den letzten zehn Jahren haben sich die Überlebensraten deutlich verbessert, doch behandlungsresistente Krebszellen stellen nach wie vor ein ernstes Problem dar und führen zu drastisch reduzierten Überlebensraten von unter 25%. Neue Behandlungsmöglichkeiten sind daher von entscheidender Bedeutung. Das Forschungsinstitut des Krankenhauses Necker arbeitet an einem neuen Therapieansatz, welcher gezielt behandlungsresistente Zellen ansprechen soll. Durch Erhöhung der Produktion von reaktiven Sauerstoffspezies in den resistenten Krebszellen könnte ein spezifischer Zelltod namens Ferroptose ausgelöst werden. Dieser regulierte, nicht-apoptotische Zelltod wird durch Eisen-katalysierte Phospholipidperoxidation anhand erhöhter Produktion reaktiver Sauerstoffradikale (ROS) über verschiedene Zellstoffwechselwege eingeleitet. Indem die ROS-Produktion in diesen T-Zellen durch exogene Initiatormoleküle künstlich erhöht wird, könnte die Nutzung dieses Mechanismus zur Bekämpfung refraktärer Krebszellen eine neue Generation von Krebstherapeutika darstellen. Diese Strategie ist vielversprechend, das Verhalten einzelner Reaktionsschritte ist jedoch noch nicht vollständig aufgeklärt.

Die Einführung der Rasterkraftmikroskopie gekoppelt mit Infrarotspektroskopie (AFM-IR) ermöglicht die chemische Identifizierung dieser Ferroptose-induzierten abhängigen Membranveränderungen im mittleren IR-Spektralbereich mit Nanometergenauigkeit. In dieser Arbeit wurde ein optimiertes Protokoll für die Probenvorbereitung, die Erfassung globaler IR-Signaturen des Peroxidationsprozesses mittels O-PTIR und die Untersuchung des Membranabbaus mittels AFM-IR erstellt. Das Methodeprotokoll wurde anhand von zwei unsterblichen Zelllinien validiert, welche mit zwei bekannten Ferroptose-induzierenden Reagenzien versetzt wurden, um den Zelltod einzuleiten. Auf diesen T-ALL Zellen konnten Hotspots mit charakteristischer Schwingungsbande für Phospholipidperoxidation identifiziert werden. Lokale Spektren an diesen markanten Punkten zeigten mehrere IR-Banden, die verschiedenen oxidierten Phospholipidperoxidations-Endprodukten in den Membranen zugeordnet werden konnten.

Table of Contents

1 Introduction

This subject is the result of a collaboration between two research institutions. The research group at ICP - Institut de Chimie Physique, Université Paris-Saclay specialises in a novel technique named atomic force microscopy coupled with infrared spectroscopy (AFM-IR). This hybrid system is able to perform label-free chemical analysis at the nanoscale. The research team at Necker hospital explores the potential of different ferroptosis inducer as successful therapy option for T-cell leukaemia on model cell lines *in vitro* via classic biophysical and biochemical methods to monitor, inter alia, lipid peroxidation.

One of the most intensely researched topics of the team 'Normal and pathological lymphoid differentiation" at Necker is the exploration of potential new cancer treatments. The type of haematological cancer important for this work is called T-cell acute lymphoblastic leukaemia ('blood cancers'). Although a positive success rate was achieved in combating this type of cancer, particular treatment-resistant cells or relapsing cells represent a major challenge. This gives rise to the development of new therapeutic options which seem to have been found with the emerging discovery of the programmed cell death mechanism called ferroptosis. This mechanism is characterized by an increase in radical oxygen species and uncontrollable lipid peroxidation leading to irreparable disruption of the cell integrity. Classic biochemical methods lack the possibility to study the localisation of therapy-induced changes at nanometric scale while simultaneously performing chemical analysis.

One possibility to overcome these limitations is the application of AFM-IR. This technique is using an AFM cantilever to detect the photothermal response of a sample after non-destructive excitation. In doing so, chemical analysis at nanometric resolution can be achieved. Hence, we propose AFM-IR to investigate ferroptosis-induced lipid peroxidation on model cell lines at the nanoscale.

In order to apply this technique to ferroptosis- induced cells and utilise it as an additional tool to answer open biological questions, a protocol covering all involved procedures has to be established. The research question of this thesis therefore addresses the development of a robust methodology including sample preparation as well as the instrumental settings for the investigation. These protocols have to be optimized as well as validated to investigate the local distribution of artificially ferroptosis-induced plasma membrane changes like phospholipid peroxidation at the nanoscale and in T-ALL model cell lines.

The work is structured starting with an introductory description of the biological context regarding T-ALL in general, ferroptosis and lipid peroxidation. This is followed by an explanation of the choice of analysis methods, their advantages and limitations before presenting the experimental protocol. This includes the gradual optimisation progression of the methodology development leading to the final procedure. The achieved results include overall tests addressing the global analysis of the cell, followed by demonstrative measurements of two chosen ferroptosis inducers used on the selected model cell lines via two different AFM-IR instruments.

2 Biological Context: New Therapeutic Strategies

The primary objective of this study is to investigate ferroptosis-induced lipid peroxidation on plasma cell membranes. This requires a detailed understanding of the biological characteristics and processes of the lymphocyte cells themselves as well as the involved biochemical pathways and reactions.

2.1 Haematopoiesis and Cell Structure of T-Cell Lymphocytes

Thymus (T) lymphocyte cells are formed and specialised from pluripotent hematopoietic stem cells (HSC) during haematopoiesis in the bone marrow. HSC are generally the development origin of red blood cells and immune cells. Originating from HSC (see Figure 1 (a)), a cascade differentiation of the cells via lymphoid stem cells and lymphoblasts (blasts, immature white blood cells) launches. During this process genetic modifications may occur. Lymphoblasts finally differentiate into T lymphocytes (marked in red, dotted rectangle in Figure 1 (a)).[1,2]

These cells belong to white blood cells and form together with B lymphocytes the acquired immune system. T-cells themselves are again divided into maturated subspecies like regulatory T-cells (T_{reg}), helper or cytotoxic T-cells, natural T killer cells and memory T-cells. To become these specialised ('mature') species, T cells migrate from the bone marrow to the thymus gland, hence their name thymus lymphocyte.[1,2] This maturation involves the formation of customised antigen receptors on the T-cell surface, accounting for the immune response upon contact with antigens in blood and peripheral lymphoid tissue. Each cell has a unique composition of receptors, so all cells as a whole have an extensive repertoire of different antigen-binding sites (Figure 1 (b)).[3]

Alterations during the differentiation process can result in malignant cells. This is characterised by a substantial rise in leukemic cells in bone marrow, with further release into peripheral blood. Depending on the stage of maturation and the cell type involved, leukaemia can be divided into lymphoblastic and myeloid leukaemia, again subdivided into acute and chronic categories. Chronic leukaemia is characterised by an overproduction of semi-mature blasts. Acute types on the other hand are dominated by a blockade of hematopoietic differentiation and leading to an excess of immature blasts. The T-cell acute lymphoblastic leukaemia discussed in this thesis belongs to the acute types, as the name suggests.[4,5]

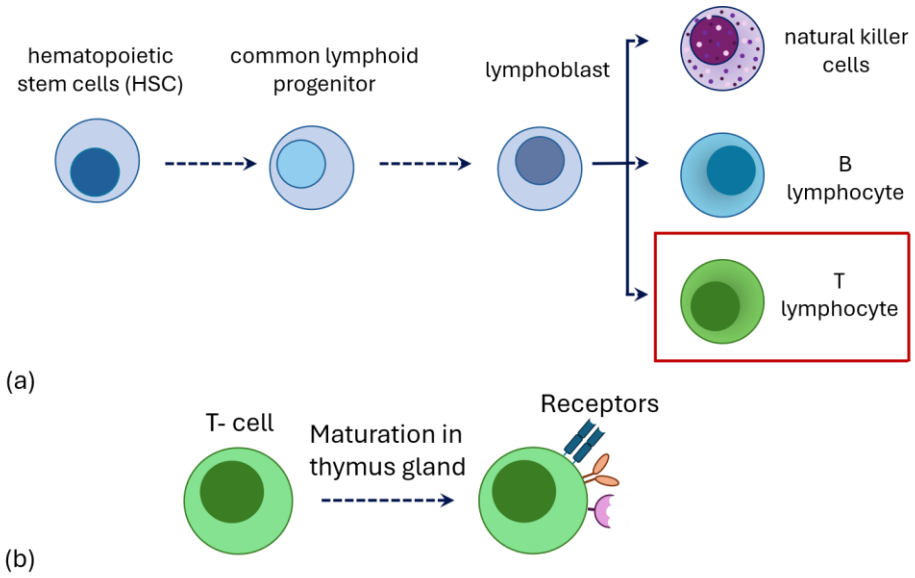

Figure 1: Haematopoiesis and maturation of T-lymphocytes
(a) During haematopoiesis, pluripotent haematopoietic stem cells differentiate via lymphoid progenitor cells and lymphoblasts into natural killer cells and B or T lymphocytes. (b) For maturation of the T cells, specific receptors are attached to their plasma membrane in the thymus gland, depending on their subtype.
Created after [3]

2.2 T-cell Acute Lymphoblastic Leukaemia (T-ALL)

T-ALL derives from by malignant transformation of progenitor T-lymphocyte cells as a part of the hematopoietic T-cell development.[6] This disease is one of the most invasive forms of haematological cancer and accounts for almost a quarter of ALL cases (25% adult and 10-15% paediatric).[6,7]

T-ALL treatments are long, intense and complex. These include potentially hazardous treatments containing personalised multiagent chemotherapy including at least four different medications targeting separate attack points. Chemotherapy is accompanied by cranial radiation therapy, immunotherapy and stem cell transplantation.[7,8] The therapeutic approach must be effective enough to ensure a complete cure, excessive therapies on the other hand increase the morbidity and mortality of the patients.[9]

Despite initially being associated with a high relapse rate, success rates and prognoses have been continuously improved, so that today event-free 5-year survival rates of up to 85% in risk-based paediatric clinical trials were achieved.[8] The overall cure rate for adult cancer cases remains poor, with currently under 50% overall survival rates, due to increased treatment-related toxicities.[10] However, if individual cells or cell groups resist primary therapy or the disease relapses (mostly within 2 years), further prognoses are poor (survival rate < 25%) and only a limited pool of additional treatment

options is available. For this reason, therapy research targeting those cases while disposing a higher effectivity, but lower toxicity in the treatments, is being promoted.[6,8]

A characteristic feature of T-ALL is a high white blood cell count, together with potential organomegaly (abnormal, pathological enlargement of one or more organs) as well as diffuse infiltration of immature T-cells in bone marrow or in the nervous system.[6] Another particular attribute is its broad immunophenotypic diversity with multiple genetic deviations.[8] Genetic analysis via PCR, DNA cloning, electrophoresis or blotting have provided a deeper understanding of the genetic mutations, oncogenes and transcription factors of T-ALL, including the NOTCH1 signalling pathway.[11]

The differentiation process from HSC to T-cells is finely regulated, therefore minuscule genetic alterations can cause major consequences. The NOTCH1 pathway is of particular importance as it plays a major role in cell signalling networks as well as the development and equilibrium maintenance (homeostasis) of multiple tissues and organs, cell fate decisions and embryonal development.[12] In T-ALL, NOTCH1 signalling is responsible for the T-cell progenitor development but also acts as an oncogene. Oncogenes are gene groups, possibly enhancing abnormal behaviour of malignant cancer cells. NOTCH1 can display mutations in 50% of all T-ALL cases and is suspected of having a major influence on pathogenesis, disease progression and treatment effectivity, rendering it a therapeutic target worth studying. Promising results are particularly suggested for refractory T-ALL patients.[7,11]

NOTCH1 also plays a role in p53 regulation.[13] The cellular tumour antigen protein p53, transcribed from gene tp53, acts as tumour suppressor (in wild-type conformation) as well as transcription factor directly transactivating up to 500 target genes. These have an indispensable role regarding DNA repair, or the initiation of cell death.[14,15] The p53 protein can be mutated in up to 50% cases of human cancer diseases and act as oncogene. It is regularly overexpressed and normally activated upon DNA damage.[14,16,17] The large number of target genes gives p53 a strongly context-dependent influence on cell death (ferroptosis) promotion or prevention.[18]

Based on these influences of the mentioned signalling pathway mutations on T-ALL cells, Necker's research focuses in particular on these oncogenic factors, either by directly inducing gene mutations or by targeting the present pathways via exogenous molecules. In this study we will use exogenous molecules as new therapy approach for objecting the forementioned cell pathways to activate ferroptotic cell death. Despite their simple chemical structure, they have a major effect on internal cell processes.

2.3 Ferroptosis

When we want to treat diseases like ischemia, cardiac illnesses or neurodegenerative disorders the objective is normally to prevent ferroptotic cell death. In leukaemia on the other hand, we want to considerably increase ferroptosis.

Ferroptosis itself is a programmed, non-apoptotic cell death, initiated by iron-mediated phospholipid peroxidation through increased (lethal) accumulation of reactive oxygen species (ROS) . This cell death process can be activated via several metabolic pathways and is upon activation quickly resulting in the destruction of certain cell species.[19] Although labelled as programmed cell death, it must be strictly separated from necrosis, autophagy or apoptosis.[20]

Ferroptotic cell death is especially associated with abnormal and lethal accumulation of lipid peroxides due to ROS-driven lipid peroxidation.[14,19] A critical point for all cells is their reaction to oxidative stress, which can be caused by extended oxidative damage to the cell membranes.[18,21] A characteristic feature of ferroptosis is lipid peroxidation involving phospholipids of the plasma membrane. This leads to a weakening of the phospholipid bilayer and possible membrane damages. Ultimately leading to irreversible cell death due to impairment and disruption of cell integrity.[22] However, it is still unclear at which cell locations lipid peroxidation originates and answering this question requires more detailed investigations. AFM-IR can contribute to the expertise in this area by investigating the resulting effects at the nanoscale.[23]

2.3.1 Metabolic Pathway and Regulation

Regulation of the metabolic pathways in ferroptosis is complex and still under investigation. We focus on specific regulation pathways affecting antioxidant stress responses via the enzyme GPX4 and its cofactor GHS or the x_c^- system.

Certain forms of regulatory instances, like the enzyme glutathione peroxidase (GPX4), are present in the cell to prevent an overexpression of peroxides. GPX4 belongs to the selenoproteins, acts as antioxidant and protects the cell from oxidative stress. It enzymatically reduces phospholipid hydroperoxides (PLOOH species) and hydrogen peroxide in mammalian cells to water and alcohols. The additional electrons required for this reduction are usually provided by its cofactor, the enzyme glutathione (GSH). Without this detoxification process, lipid peroxidation is initiated and rapidly propagated. This makes GPX4 an indispensable controller of ferroptosis. It is therefore speculated, that an artificial suppression of the GPX4 enzyme results in a calculated iron-dependent accumulation of (lipidic) ROS and eventually in ferroptosis and inflammation.[18,24]

The x_c^- system is an amino acid antiporter (integral membrane protein) and regulates the cystine import of cells. p53 can potentially influence this intake by controlling the transcription of a x_c^- subunit and therefore enhancing ferroptotic cell death. By suppression of the cystine intake, a disruption of the GHS synthesis is obtained. The GHS synthesis can also be directly impeded. In both cases the antioxidant defence in the cell is interrupted, which results in the disintegration of the peroxide reduction in the cell, since GPX4 no longer receives the electrons required for it.[19,25]

We can influence these pathways with various exogenous molecules, like the GPX4-blocker RSL3, causing ferroptotic lipid peroxidation.[26]

2.3.2 Lipid and Phospholipid Peroxidation

Lipid peroxidation is the oxidative destruction of lipids, caused by the electron intake of free radicals (like ROS). from unsaturated fatty acids (PUFAs). PUFAs form a component of the bilayer of the plasma membrane. The phospholipid bilayer is important for the function of all cells to ensure an adequate membrane integrity, since membrane degradation presents a precarious exposure against external influences. The plasma membrane, as presented in Figure 2, acts as separator and protector. The presence of the phosphate group in addition to the (un)saturated fatty acids on the basic glycerol molecule causes both hydrophilic and hydrophobic molecular sections. These enable an automatic orientation of the cell membrane with hydrophobic layer facing inwards.[27]

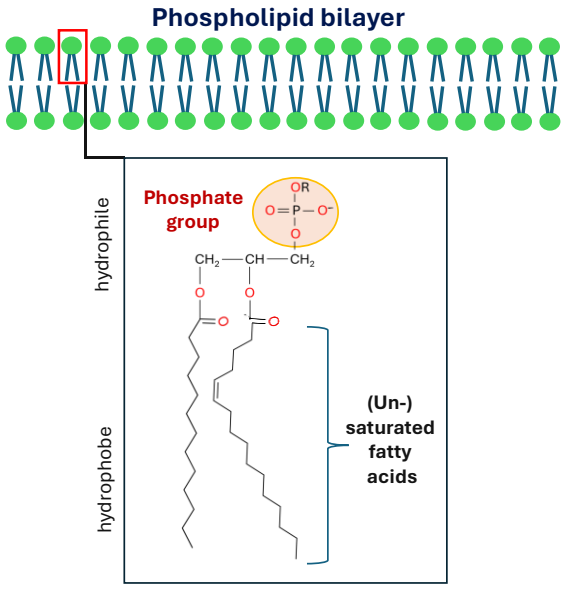

Figure 2: Phospholipid bilayer – Plasma membrane
In addition to the glycerol backbone and two apolar fatty acid residues, phospholipids consist of a polar phosphate group. The molecules align as bilayers in the cell due to the hydrophobic and hydrophilic components.

The oxidative lipid destruction leads to the formation of lipid radicals pushing the process further and triggering a chain reaction. Lipid peroxidation itself has multiple influence sources and is not only limited to a ferroptotic response.[18] Cancer cells are increasingly exposed to membrane stress due to their motility and oxidative stress levels.[27]

ROS (radical oxygen species) is a general term for an assortment of oxygen radicals including superoxide ($O_2^{\bullet -}$), peroxides (H_2O_2 /RO-OH/ROO-OH) or free radicals ($HO^{\bullet}$/$RO^{\bullet}$).[28] While iron plays a catalytic role in several enzymatic processes, among others in H_2O_2-destroying enzyme catalase or also in ROS-producing enzymes, oxygen is the most important electron acceptor.[18] Molecular oxygen, ROS and iron are all essential for a regulated course of cell processes. Only if the concentration of one or more of these compounds changes rapidly, an imbalance occurs, which causes cell degeneration.[28]

Iron can occur in small amounts as labile redox-active ('free") Fe^{2+} ions in the cytosol or lysosome, which allows non-enzymatic, direct catalytic production of free radicals via Fenton reaction. The Fenton reaction is the reaction of peroxides with Fe^{2+} which results in either soluble hydroxyl ($HO^{\bullet}$) or lipid alkoxyls ($RO^{\bullet}$) see Figure 3 (a). This formation of lipidic ROS can again be prevented by GPX4. Superoxides or H_2O_2 can damage iron-containing proteins [Fe-S bounds], which form even more redox-active iron (see Figure 3 (b)). In turn, H_2O_2, lipid peroxides or molecular oxygen can be converted at the formed Fe^{2+} to generate new ROS (mainly $HO^{\bullet}$). An additional effect is the inactivation of said proteins.[23,28]

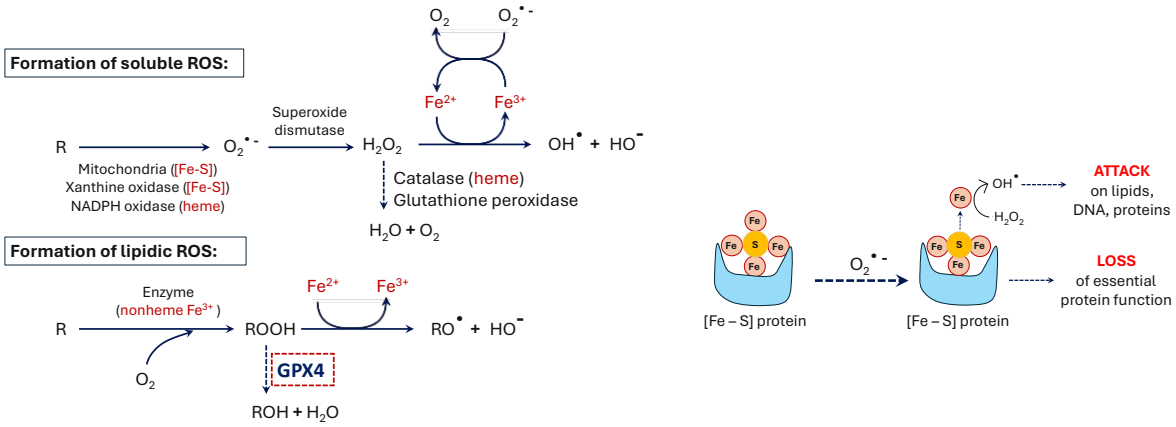

(a) (b)

Figure 3: Fenton reaction

(a) Reaction sequence of Fenton reaction for the formation of soluble and lipidic ROS. The present form of iron in each step is marked in red (b) Production of labile Fe^{2+} ions by the attack of H_2O_2 on iron-containing sulfuric proteins.

Reproduced with permission from Springer Nature, Dixon et. al. [28]

Lipid peroxidation is initiated enzymatically and non-enzymatically by free radical mediated dissociation of hydrogen in phospholipids (PL) (Figure 4). These carbon-centred phospholipid radicals (PL•) can react with molecular oxygen to form highly reactive phospholipid peroxyl radicals (PLOO•), which in turn react with PL and initiate a chain reaction. In addition, phospholipid hydroperoxides (PLOOH) are formed by taking a hydrogen atom from another polyunsaturated fatty acid (PUFA), which are converted by Fenton reaction into hydroxyl and PL-alkoxyl radicals (HO• and PLO•) and therefore further enhance the chain reaction. A possibility to reduce lipid peroxides in this process is the regulation by GPX4. Eventually, not only lipid peroxides formed, but also oxidised proteins.[23,29]

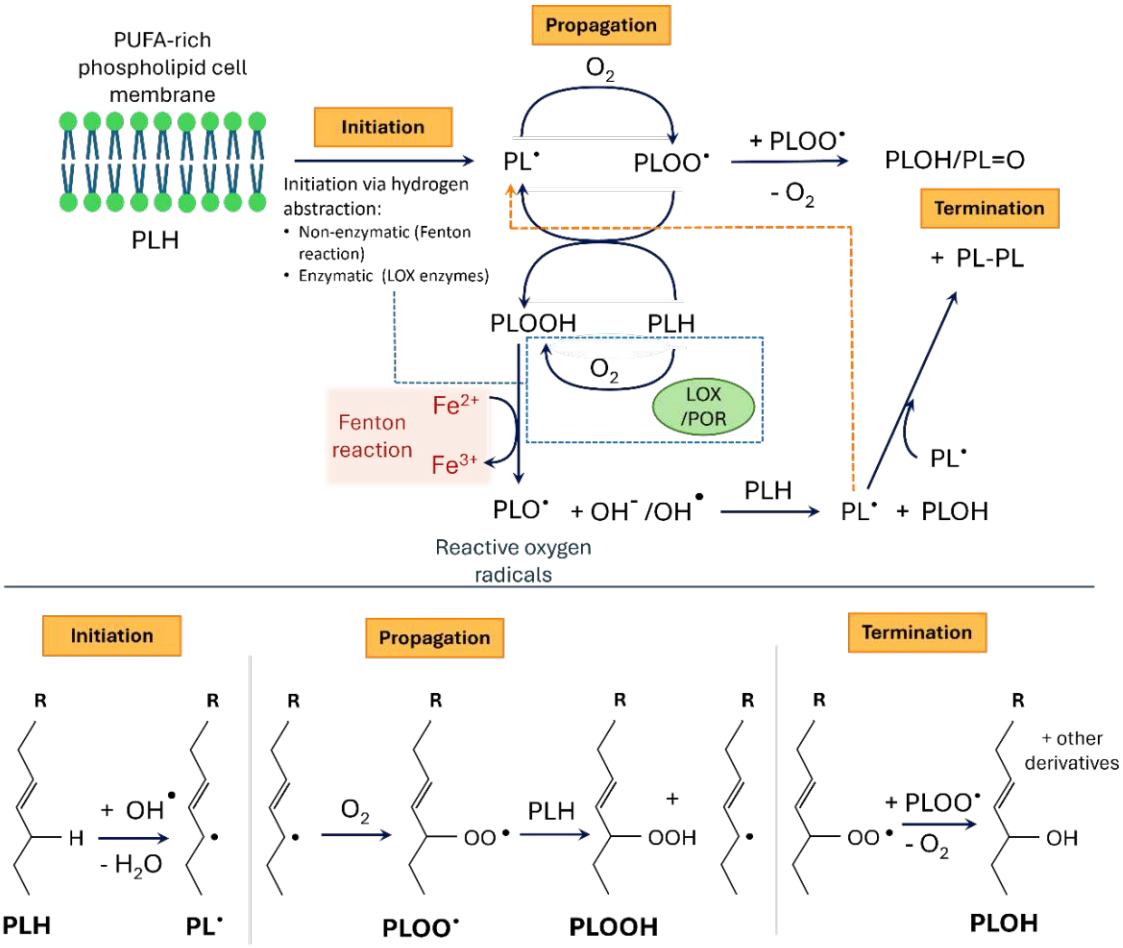

Figure 4: Mechanism of lipid peroxidation leading to ferroptosis.
At the cell membranes, hydrogen is abstracted from phospholipids PLH in an initiation step (enzymatic or non-enzymatic). After this initiation, PL• can react with molecular oxygen (propagation), which leads to the formation of highly reactive peroxyl radicals (PLOO•). These are reactive against PLH, which triggers a chain reaction. Further secondary products such as PL• and PL hydroperoxides (PL-OOH) are formed. These are further transferred to alkoxyl and hydroxyl radicals from PLOOH by Fenton reaction. Termination of the chain reaction can end, among others, by haemolytic dissociation of adjacent carbon-carbon bonds, dimerization of two PL radicals or PLOO radicals.
Created after Jiang et. al.[18] and Rodriguez et.al.[23]

When the GPX4 antioxidant is blocked, PLOOHs persist longer and are converted by Fenton chemistry to produce even more PLO• radicals as well as PLOO• and PLOOH. The ever-progressing chain reaction now involves more and more PUFAs of the plasma membrane until it weakens and impairment of the phospholipid bilayer is achieved.[18]

Figure 5 summarises the ferroptotic process again. Increased ROS and PUFA-PLs levels influenced by cell metabolism lead to phospholipid peroxidation in connection with the transition metal iron. The peroxidation reaction can be inactivated or influenced at various target points such as by GPX4 (RSL3). Phospholipid peroxidation can cause multiple types of damage in the cell, which ultimately results in ferroptotic cell death. This pathway is the cause of various diseases. However, it can also be utilised to kill specific cells.[18]

This hypothesis led to newly emerging ideas to investigate the ferroptotic cell death against leukaemia.[30] For cancer treatments the therapeutic relevance lies in inducing and enhancing ferroptotic cell death.[18] Ferroptosis as cancer treatment is particular interesting, since already therapy-resistant malignant cancer cells exhibit a strong sensitivity to this cell death mechanism due to the role of iron in cancer progression, their enhanced metabolism, natural high loads of ROS and their oncogene mutations.[18,21,23] Especially the commonly mutated tumour antigen p53 represses, when activated, the cystine intake and therefore increases the sensitivity of the cells to ferroptosis.[31] The focus on cancer treatment via the NOTCH1 pathway is already a widely researched topic. The Necker Research Institute hypothesises in this context that NOTCH1-mutated cells have a higher sensitivity to ferroptotic cell death, due to NOTCH1s' role in promoting cell proliferation. Results from Failla [32] demonstrated that the activation of NOTCH1 induces metabolic pressure on the cells mitochondria, which results in higher ROS accumulation and further peroxidised lipids. Both effects lead to a reduction in potency of antioxidant defences and increase oxidative stress in the cells. This makes NOTCH1 oncogenic-activated cells more susceptible to ferroptosis.[32]

The mechanism is still under intense study, as the actual chemical 'point of no return', responsible for ferroptosis-cell death, is not confirmed yet. It is verified that uncontrolled peroxidation of PUFA-phospholipids plays a crucial role in cell degradation and may be associated with nanoscale hotspots of peroxidised phospholipids causing membrane damage, lipid cross-linking to limit membrane fluidity or impairing membrane integrity by pore formation.[18]

In order to understand the consequences on the cell leading to ferroptosis more precisely, one must first take a closer look at the occurring phospholipid peroxidation itself.

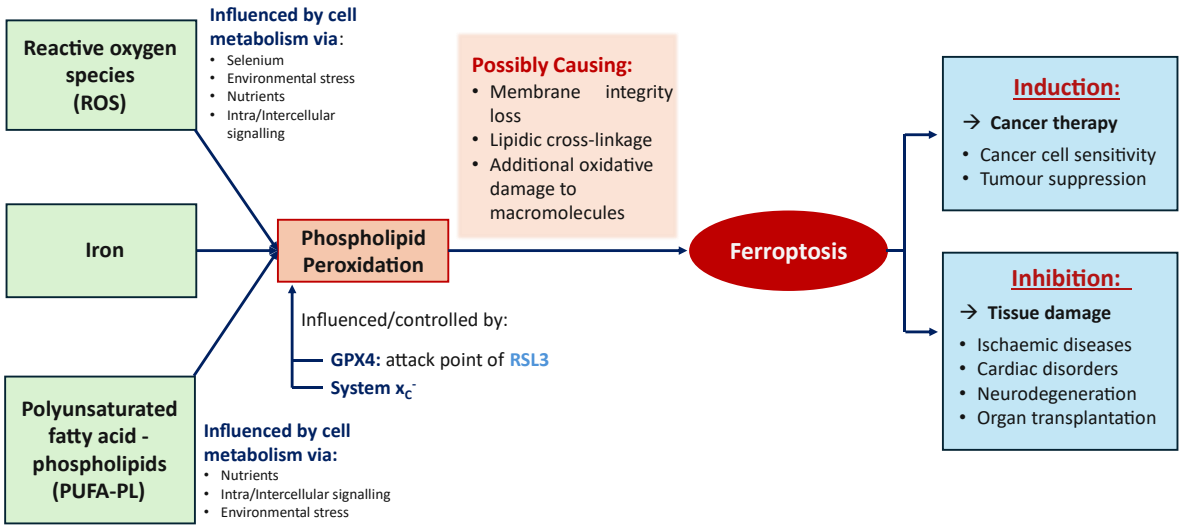

Figure 5: Schematic representation of ferroptotic cell death
Ferroptosis is caused by phospholipid peroxidation based on increased levels of reactive oxygen species (ROS), which convert polyunsaturated fatty acid phospholipids (PUFA-PLs) via iron into radicals. This process can be influenced by internal control systems such as GPX4 or the x_c^- system. The ROS and PUFA-PL levels themselves can be affected by internal metabolism processes. The phospholipid peroxidation can cause different cell impairments ultimately leading to ferroptotic cell death. This can either be intentionally desired and induced (cancer therapy) or cause diseases that need to be prevented.
Reproduced with permission from Springer Nature, Jiang et.al. [18]

2.4 Therapeutic Strategies

The actual implementation of artificially induced ferroptosis must first be investigated in cell cultures. This is needed to obtain additional knowledge about the lipid peroxidation processes and their effects on the membranes.

2.4.1 Ferroptosis Inducer

One of the first observed exogenous molecules by Dolma et. al.[26] and Yang and Stockwell[33] to artificially induce ferroptosis was RAS-selective lethal 3 (RSL3), followed by many more in last years. Interestingly, different inducers trigger contrasting cellular pathways causing ferroptotic cell death. One may conclude therefore that the activation of ferroptosis is not limited to the presence of one certain factor.[19,25]

Multiple inducers were tested from different regulation groups. In this study we focus on two of them from different families: The activator RSL3 and a molecule called APR-246. They have been proven as potent ferroptosis-inducers, partly already in use in preclinical studies.[14]

RSL3

RAS-selective lethal 3 (RSL3), structure displayed in Figure 6, is a selective and effective ferroptosis activator directly repressing phospholipid glutathione peroxidase 4 (GPX4). This happens in a dose- and time-depended manner by binding GPX4 and amending the iron transport in the cells. Sui et. al.[24] reported consequently an RSL3-dependend increase of intracellular ROS and LIP (labile iron pool) level for 24 h incubation periods after addition of RSL3 to *in vitro* cell cultures. Phospholipid hydroperoxides (PLOOHs) accumulate after the RSL3 suppression of GPX4 and cause immediate and irreversible membrane impairment resulting finally in ferroptotic cell death.[18,29,34]

Institute Neckers' investigations established a high potency, which made its use obvious in the investigations.

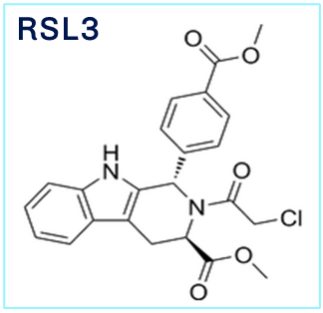

Figure 6: Chemical structure of ferroptosis-inducer RSL3
IUPAC notation: methyl (1S,3R)-2-(2-chloroacetyl)-1-(4-methoxycarbonylphenyl)-1,3,4,9-tetrahydropyrido[3,4-b]indole-3-carboxylate)

APR-246

PRIMA-1 is a drug leading to p53 re-activation and induction of apoptosis. It has been already tested in several clinical trials together with additional treatment medication for malignant cancer cell therapy. APR-246 (chemical structure in Figure 7) is a methylated derivative of PRIMA-1 and seems to have a wide range of action, but with less specificity. However, it induces ferroptosis in an efficient manner.[14,15]

Its functionality was formerly assumed to be connected to a mutation of the cellular tumour antigen p53, since APR-246 leads to a covalent modification of the p53 core domain through alkylation of thiol groups. This resets the conformation of the mutated p53 protein, to a wild type ('wt') conformation. The refolding leads to the restoration of the p53 protein, which is able to inhibit tumour growth, stagnation of the cell cycle and ultimately cell death.[14,15] The tumour suppression is caused by blocking the x_c^- system through preventing the x_c^- subunit transcription. As a reminder, p53 also has a highly context-depending role in initiating ferroptosis, either promoting or preventing it by regulating target

genes.[18] However, APR-246 can also impact other intracellular proteins. It has been proven to interfere with oxidative cellular stress reactions by affecting the antioxidative metabolic pathways via modifying (seleno)cysteines of the enzyme glutathione reductase. This enzyme is necessary for the formation of GSH, the cofactor of GPX4. The existence of this multitude of attack options gives it an extensive manoeuvrability in its actions.[35]

Recent studies reported that APR-246 may kill malignant cancer cells regardless of the mutation status of p53. Further results also highlighted that multiple programmed cell death pathways like apoptosis, necroptosis or ferroptosis can be initiated depending on the cancer cell type and the initiated concentration of the treatment reagent.[14,36] Results reported in Wang et. al. indicate that APR-24 dependent apoptotic or necroptotic cell death mechanism can cooperate with ferroptosis in certain cases. This results regardless of the combination of the individual cell deaths in plasma membrane impairment of the malignant cancer cells.[14]

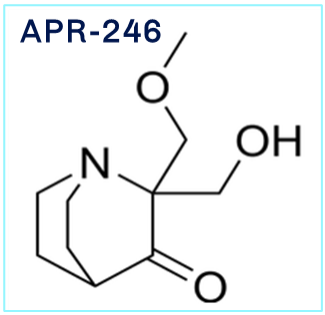

Figure 7: Chemical structure of cell death inducer APR-246
IUPAC notation: 2-(hydroxymethyl)-2-(methoxymethyl)-1-azabicyclo[2.2.2]octan-3-one

2.4.2 Model Cell Lines

To understand ferroptotic cell death and its accompanied lipid peroxidation, the two following immortal model cell lines with the following specifications for investigations, were proposed to be studied in this diploma thesis:

Jurkat

Jurkat is an immortalized, pseudodiploid human model cell line of T – lymphoblasts generated from peripheral blood of a male, 14-year-old T-cell acute leukaemia patient by Schneider et al.[37] for 3D cell culture, immune system disorder research and immunology. This tumour cell line from type Jurkat exhibits a NOTCH1-mutation.[38] NOTCH1-altered T-ALL cells exhibited a higher cell death rate compared to wild-type NOTCH1 T-ALL cells, based on initial results from the INSERM Necker Institute.[32] The mutation should increase the sensitivity to the ferroptosis inducers used in this study.

Loucy

This immortalized human cell line was isolated from peripheral blood of a white female, 38-year-old T-cell acute leukaemia patient in 1987 and is used in immunology and immune system disorder research. It displays an overexpressed p53+ oncogene (regulates cellular response cell stress) with an GTG to ATG mutation at codon 272. NOTCH1 is defined as wild-type for Loucy.[39] According to preliminary results, this cell line exhibits a lower sensitivity to the ferroptosis inducers APR-246 and RSL3. Loucy was therefore defined as reference cell line for this study.

One can follow the effects of lipid peroxidation of ferroptosis treatments on the model cell lines with several techniques, such as fluorescence spectroscopy, classical biochemistry methods or via lipidomics (albeit difficult). The problem with all these methods is that no assertion can be made about the distribution of the lipid peroxidation occurrences on the cell itself, caused by their lack of spatial resolution. Also, no local chemical specificity can be determined in these investigations. Since these methods are partly of destructive nature, individual treated cells cannot be examined with several complementary methods.

These facts dictate the need for a non-destructive, label-free and chemically specific technique providing higher spatial resolved chemical information. Atomic force microscopy coupled with infrared spectroscopy (AFM-IR) fulfils all these requirements, hence it was used for the investigation of ferroptosis-induced lipid peroxidation in this thesis.

However, to obtain these results a new protocol for the investigation of nanoscale hotspots of peroxidised phospholipids due to different ferroptosis inducers via AFM-IR had to be established first.

3 Investigation of Lipid Peroxidation by Mid-Infrared Spectroscopy Based Techniques

As AFM-IR is an IR based-technique, a general presentation of IR techniques used for the study as well as the methodology will be explained.

3.1 Infrared Analysis of Biological Samples

Infrared radiation (IR) is part of the electromagnetic radiation spectrum located between the visible and the microwave region. Especially interesting for organic and biochemical research is the Mid-IR region between the wavenumbers 4000 and 400 cm^{-1} (wavelength 2.5 – 25 µm). The strong fundamental vibrations of organic molecules lie in this spectral region. This makes it possible for mid-IR spectroscopy to examine molecular vibrations with high sensitivity.[40–42]

IR spectroscopy utilises the molecules' ability to absorb radiation of certain energies in the infrared spectral range, due to a quantization of energy levels on a molecular scale. The absorption corresponds to the frequencies at which their molecular vibrations occur. When the energy of a photon $\left(E = h \cdot \frac{c}{\lambda}\right)$ equals the energy difference between the ground and the excited state $\left(\Delta E = h \cdot \nu \cdot \left(\nu \cdot \frac{1}{2}\right)\right)$ and the dipole moment of the whole molecule changes during vibration, then absorption can take place. These vibrations include among others symmetric and antisymmetric stretching as well as planar-based bending vibrations, depending on the number of atoms in the molecule and their bond structure. Generally, more energy is required for stretching than bending, which is why stretching-based vibrations are in the 4000 – 1500 cm^{-1} spectral range and stretching-bending couples are between 1500 and 400 cm^{-1}.[40]

Advantages of IR spectroscopy are its ability to perform direct, non-contact and non-destructive measurements. The molecules do not have to be modified or labelled beforehand and little sample preparation is required. Especially the introduction of Fourier-transform principle (FT) to IR spectroscopy introduced rapid scanning speeds, increased sensitivity and enhanced data-treatment options.[41]

Absorption spectra of organic compounds consist of multiple absorption bands with varying intensities at different wavenumbers characteristic for the structural attribute of the molecule. This results in unique absorption spectra for every existing compound, especially regarding the 'fingerprint" region (1500 – 675 cm^{-1}). In the case of localised vibration only the motion of a few atoms occurs. In this case the frequency of the vibration can be approximated by a harmonic oscillator whose frequency can be

expressed by $\nu = \frac{1}{2} \cdot \pi \cdot \sqrt{\frac{k}{m_R}}$ with k being the force constant of a band connecting two vibrating atoms with the reduced mass m_R. These localized vibrations are characteristic for functional groups present in a molecule. The chemical environment may affect the force constant of chemical bonds. Therefore, inductive as well as mesomeric effects, present in a molecule will cause a shift of the vibration frequency and thus, also of the wavelength (wavenumber) where an absorption is observed. Similarly, also H-bonds as well as inter- and intramolecular interactions can affect the band position of vibration in the mid-IR spectrum of a molecule.[40]

In biology, IR is extensively used towards evaluation of cell functionality, the detection of specific molecules in tissue as well as the examination of the cell architecture, clinical screening for the diagnosis of diseases or the analysis of the secondary structures of protein.[42,43]

A typical absorption spectrum of cells is displayed in Figure 8 with characteristic bands assigned to characteristic substance classes. Mid-IR bands can be assigned to proteins, lipids, DNA/RNA and carbohydrates. Mammalian cells consist on average of 60% (w/w%) proteins, 10-15% lipids, 6-8% carbohydrates and about 25% nucleic acids (ratio DNA/RNA 1:5) but may vary depending on tissue type, cell division type and nutrition.[44]

Since not only individual components exist in cells, but rather families of components with a huge diversity of environment, IR absorption spectra exhibit broad bands. From 1745-1725 cm^{-1}, C=O stretching vibrations of the ester moiety present in lipids and phospholipids can be found. Next to it two pronounced composite bands, composed of the vibrational influences of several molecular bonds, appear. At 1655 cm^{-1} the amide I band consisting of ~80% C=O stretching vibration, ~10% C-N stretching vibration and ~10% N-H bending vibration is located. The amide II band 1543 cm^{-1} is a composite of N-H bending vibrations (~60%) and C-N stretching vibrations (~40%). Both derive from the peptide band present in protein.[45] Changes of the band maxima and possible band shoulders occur depending on the secondary structure of said protein, due to different degrease of H-bonds and dipol-dipol coupling for different secondary structures such as α-helix, β-sheet and random coil.[46]

The band ranging between 1468–1455 cm^{-1} is associated with antisymmetric CH_3 stretching vibrations and CH_2 bending modes of lipids and proteins.[47,48] For 1400-1386 cm^{-1} an overlapping band corresponding to symmetric $RCOO^-$ stretching and symmetric CH_3 bending of amino acids, free fatty acids and lipids occurs.[46,47] The regions between 1250-1220 cm^{-1} and 1085-1080 cm^{-1} can be assigned to antisymmetric PO_2^- and symmetric PO_2^- stretching modes from organic and inorganic phosphate groups like phospholipids or nucleic acids.[46]

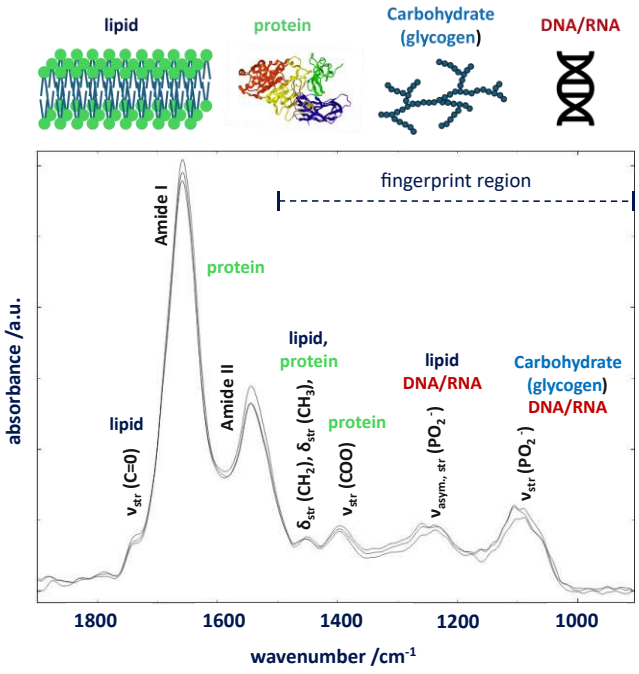

Figure 8: Typical IR cellular absorbance spectrum.
The characteristic responses originate primarily from proteins, lipids, DNA/RNA and carbohydrates. As these are component families, very broad bands are apparent in the absorbance spectrum.

In the following Table 1, the typical IR absorption bands in biological samples are listed.

Table 1: Typical IR bands occurring in a cellular absorption spectrum and their respective origin molecule class

wavenumber /cm^{-1}	assignment	origin molecule
1740	C=O stretching	lipids, phospholipids[45,49]
1715	C=O stretching	carbonic acids[44]
1715-1680	C=O stretching	nucleic acids (DNA/RNA)[44]
1685-1675	antiparallel ß-sheet, ß-turns	proteins[50]
1655	amide I	proteins[45,46,51]
1638	parallel and antiparallel ß-sheet	proteins[50]
1610-1550	$RCOO^-$ antisymmetric stretching	free fatty acids, lipids[45,50]
1543	amide II	proteins[45,51]
1468 – 1455	CH_2 scissoring CH_3 antisymmetric bending	lipids[47] proteins[48]
1400	$RCOO^-$ symmetric stretching	amino acid side chains, free fatty acids[44,46]
1386	CH_3 symmetric bending	lipids[47]
1400-1335	CH_2 wagging	[48]
1310-1240	amide III	proteins[44]
1250 - 1220	PO_2^- antisymmetric stretching	phospholipids, nucleic acids[46]
1179 - 1160	CO-O-C antisymmetric stretching	(cholesteryl) ester bonds[47,52] carbohydrates[48]
1085	PO_2^- symmetric stretching	phospholipids[46] DNA (Phosphate backbone)[53]
1045-1041	C-O-P stretching C-O stretching	phospholipids[45] glycogen, nucleic acids[47]
1200-900	bending vibrations C-O-C, C-C, C-OH, C-O	carbohydrates, peptide backbone[44,46]
965	phosphodiester of DNA backbone links	DNA/RNA[45]

As previously explained, peroxides with a specific IR response appear during ferroptosis.

The peroxides and hydroperoxides formed during lipid peroxidation contain distinct structural units, one C-O and a O-O group. The stretching vibrations associated C-O are located between 1300 and 1000 cm^{-1}. The O-O stretching vibration reveals a band at 900-800 cm^{-1} in all peroxides. Other appearances can be caused by carbonyl (C=O) groups of oxidized products. These can include ketones, aldehydes or alcohols and esters formed during lipid peroxidation. The carbonyl band centred at 1740 cm^{-1} is especially associated with peroxidised phospholipids and is indicative for the oxidation progress. [45,54,55]

In Table 2 the wavenumbers of oxidised and peroxidised molecular species are listed.

Table 2: Wavenumbers of oxidised and peroxidised cell molecule classes extracted from [45] and [54]

wavenumber /cm^{-1}	spectral assignment and description	origin molecule
1780	C=O	aliphatic peroxides
1740	C=O stretching	phospholipids, esters[44]
1785-1755	C=O stretching	peroxyacids
1760-1735	C=O stretching	carboxylic peroxyacids
1460-1430	O-H bending (CO-OOH)	peroxyacids[1]
1300-1050	C-O stretching (CO-OOH)	peroxyacids
1260-1250	C-O stretching	lipid hydroperoxides
1175	C-O stretching	peroxyacids
1150-1130	C-O stretching	alkyl peroxides
1000	C-O stretching	aryl peroxides
900-800	O-O stretching	peroxides[2]

[1] shifted towards 1430 cm^{-1} for linear, long-chain acids
[2] ~ 865 cm^{-1} for peroxyacids

1657 cm^{-1} (Amide I) was gathered representative for the total protein content whereas 1740 cm^{-1} was proposed as the characteristic wavenumber of lipid peroxidation (C=O stretching vibration of phospholipids).

The main drawback of conventional IR microscopes is the limited spatial resolution they provide over the whole spectral range due to the wavenumber-dependent Rayleigh criterion.[56–58]

The theoretical resolution δ of a microscope is given by the Rayleigh criterion as described in Eq. (1):

$$\delta = 0.61 \frac{\lambda}{n \cdot \sin(\alpha)} = 0.61 \frac{\lambda}{N\,A} \qquad \textit{Eq. (1)}$$

Where n is the refractive index of the surrounding medium, α is the objective's half-opening angle and λ is the applied wavelength. The term n · sin(α) is also known as the numerical aperture N A of the optical imaging system.[56–58]

For a typical numerical aperture of 0.7 and a refractive index of 1.5 for the spectral range 2000 to 1000 cm^{-1} (5 – 10 µm) the calculated spectral resolution ranges between 4.4 and 8.7 µm. The size of living T-ALL cells is around 10 – 20 µm. That makes it impossible to investigate sub-micrometric or nanometric intracellular structures for the given T-ALL cells via IR spectroscopy alone.[56,59]

Figure 9 compares the size of a single T-ALL cell with a typical pixel size in an FTIR microscope (experimental lateral transmission resolution: 10-30 µm). This results in a large-area coverage of a single cell with one pixel, which means that two distinct locations on this cell cannot be distinguished.

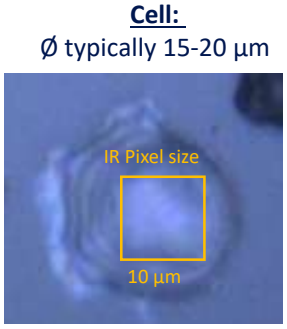

Figure 9: Cell superimposed with IR pixel (µFT-IR)
Highlighting the difficulties of conventional µFT-IR resolution on a microscopic image of one cell by superimposing one IR pixel on the cell.

The technical limits can be improved by changing the radiation source. Either synchrotron radiation or new generations of quantum cascade laser (QCL) present a way to enhance the pixel resolution, but not as sufficient as required for investigating subcellular structures. Quantum cascade lasers (QCLs) are electrically pumped semiconductor lasers, whereby the emission of coherent Mid-IR radiation is caused by electron transitions within the semiconductor conduction band.[60] We propose to use novel experimental approaches with submicrometric resolution to analyse lipid-peroxide accumulations on cell membranes.[61]

3.2 Super Resolution IR Techniques

To overcome the diffraction limit, alternative techniques based on the detection of the photothermal effect that occurs within the sample after absorption of IR radiation, were invented.

A material can absorb IR radiation at specific, material-dependent wavenumbers, causing a local temperature change and shifts of the refractive index. It also results in a sub-nanometric thermal expansion of the sample material.[62] The power absorbed by the material is proportional to its imaginary part of the complex refractive index, but also strongly dependent of its inner electric field.[63]

The detection of the photothermal expansion requires techniques to register the sub-nanometric expansion. In case these can be detected with a high spatial resolution also spatially highly resolved measurements possible. This, however, requires other techniques for read-out of the photothermal sample response than the mid-IR excitation radiation. These have gradually emerged during the last decades. Among them are optical photothermal infrared spectroscopy (O-PTIR) and atomic fore microscopy coupled with infrared spectroscopy (AFM-IR), which use vis-radiation and a cantilever tip respectively, for detecting the photothermal expansion.

Both methods use sampling technique, different from mid-IR radiation, so the spatial resolution is no longer dependent on the wavenumber of the excitation radiation in mid-IR spectral range. Instead, the

spatial resolution depends on the individual probing principle. Figure 10 visualizes the lateral resolution of both methods compared to conventional FT-IR microscopes. The lateral resolution of O-PTIR can reach sub-micrometric values [64], while AFM-IR can distinguish single locations around 10 nm.

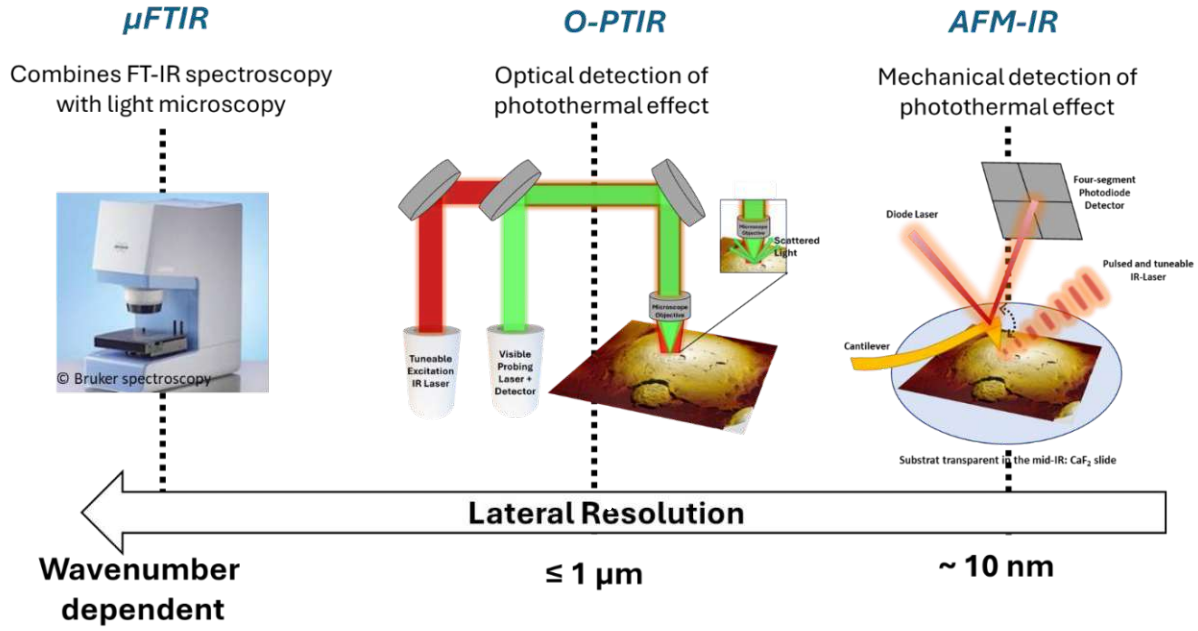

Figure 10: Comparison of the lateral resolution between µFT-IR, O-PTIR and AFM-IR
The lateral resolution of a conventional µFT-IR setup (measurement of absorption/transmission spectra) is dependent on the wavenumber. O-PTIR and AFM-IR detect the consequences of the photothermal effect, after absorption of IR radiation. In the O-PTIR system the detection is performed optically and in AFM-IR via mechanical scanning.

3.2.1 O-PTIR – Submicrometric Resolution

Optical photothermal infrared spectroscopy (O-PTIR) can measure IR spectra with sub-micrometric resolution. A pulsed, tuneable IR laser and a continuous probing laser beam with fixed wavelength in the vis or NIR range (532, 758 nm) are colinearly focused on the sample surface. If the wavelength of the IR radiation corresponds to an absorption band of the sample, the according sample region rapidly heats up and causes a photothermal response. The rapid increase of temperature induces a modulation of the reflective index of the sample and the air around it along with a sample expansion. Both effects will impact the reflected green laser beam. The measurement of this laser beam reflection signal gives access to the infrared absorption of the sample. The spatial resolution depends due to this sampling technique on the wavelength of the probing laser.[65,66]

The mIRage® instrument (Photothermal Spectroscopy Corp.) uses a pulsed 100 kHz tuneable IR laser, illuminating a larger sample area. Together with a collinear visible, green probing laser, both are focused by a microscope objective on the acquired surface (see instrumentation setup Figure 11). The continuous green visible laser beam (fixed wavelength: mainly 532 nm) is probing a smaller surface

area than the excitation IR laser. The system set-up allows the mIRage to operate without mechanical contact with the sample.[65,66]

The exact theoretical background of the instruments' measuring mechanism is still under investigation.[67]

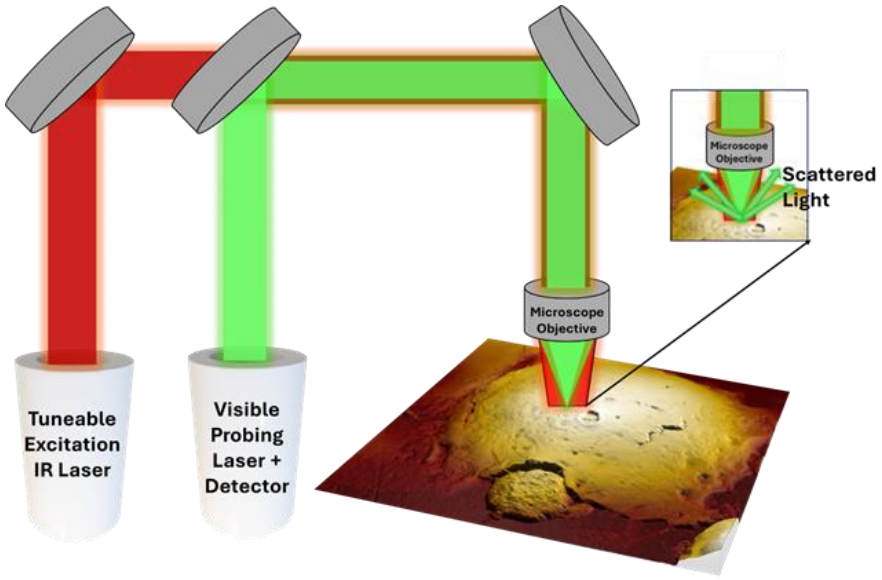

Figure 11: O-PTIR principle
The utilised O-PTIR set-up included a tuneable excitation laser (red) and visible probing laser (green, 532 nm). Both are focused via a microscopic objective on the sample surface. The photothermal response based on the absorbed radiation of the sample leads to modulations of the sample and its surrounding airs reflective index. These modulations result in scattering and deflection of the probing laser which is going to be measured.

This instrumentation set-up can be used with two different laser sources to record spectra in varying spectral ranges. The usage of mIRages® built-in quantum cascade lasers (QCL) results in a spectral range between 1900 – 900 cm^{-1} whereas optical parametric oscillators (OPO) allow the analysis of functional groups between 3600 - 2700 cm^{-1}. The probe laser remains in both cases unchanged. [65,66]

Since the spatial resolution is no longer dependent on the wavenumber of the IR excitation laser, but on the probing laser (532 nm), it can be reduced to submicrometric level while scanning the whole IR laser range. The resolution was evaluated in the team at ICP and found to be around 0.86 µm.[67]

3.2.2 AFM-IR – Nanometric Resolution

AFM-IR is a hybrid technique combining the advantages of atomic force microscopy and infrared spectroscopy.

3.2.2.1 AFM principle

Atomic force microscopy is an analysis tool for studying surface structures with nanometric resolution in nanometre-scale and is part of the so called 'scanning probe near-field technique' family. Instead of using light or electrons, AFM recreates a topography image by probing the surface roughness with a sharp tip at the apex of a cantilever. This principle is schematically illustrated in Figure 12 (a).[68]

An AFM consist of a cantilever including a tip, a diode laser, four-quadrant photodiode and a controller feedback-loop. The tip is in the vicinity of the sample, undergoing interaction with the surface (Figure 12 (b)). The interaction force induces a bending of the cantilever detected by an optical four-quadrant photodiode system. The diode is focused on the top of the cantilever and reflected towards a four-quadrant detector. The deviation of the beam is directly linked to the deflection of the cantilever and the interaction force between the tip and the surface. By measuring the deflection during the movement of the tip in xy-direction or along the z-axis, this instrument provides access to the topography of the surface (Figure 12 (c)) or its mechanical properties.[68,69]

Due to this sampling mode, the maximum size scanned by the piezoelectric actuator is instrument dependent. Little or no sample preparation is needed, vacuum does not have to be applied and a spatial resolution in nanometre-scale can be achieved. This is possible due to the size of the tip apex being in the nanometre range.[68]

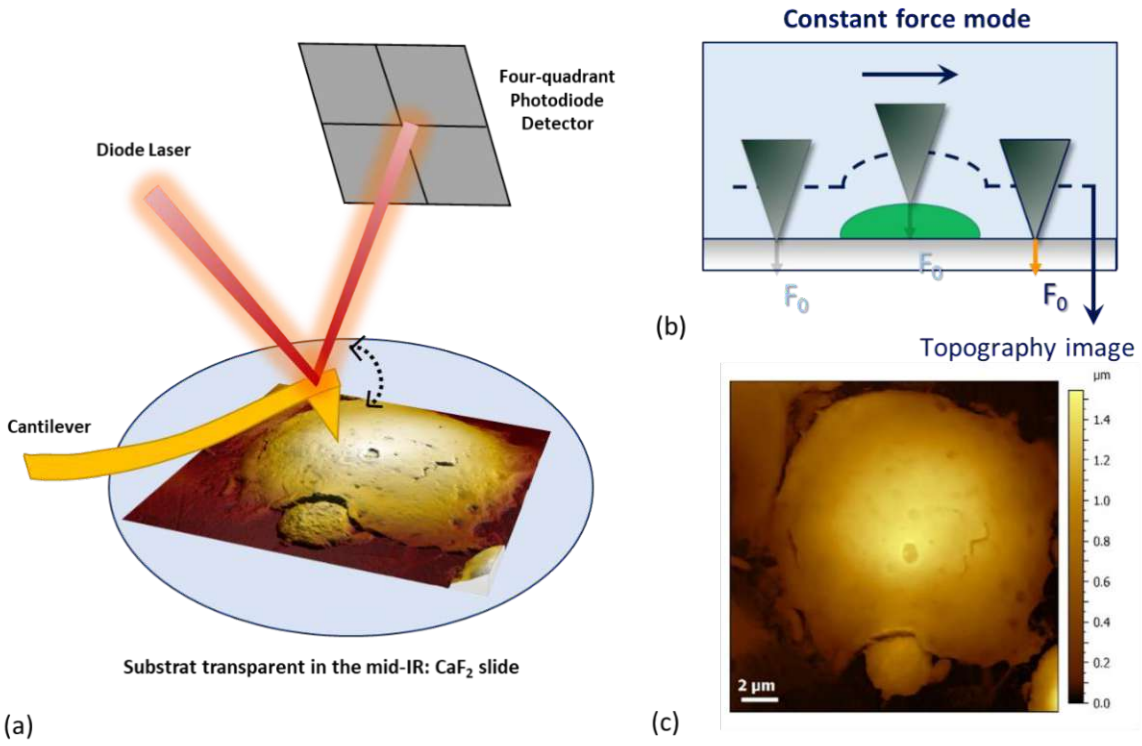

Figure 12: AFM principle
(a) Schematic view of an AFM setup in contact mode scan. During the measurement, the sample-dependent deflection of the cantilever is recorded by a location-sensitive four-quadrant photodetector. (b) Tip position and its height progression when crossing an object in constant force mode. (c) Visualisation of a characteristic cell topography levelling illustrated as 2D image. In accordance with the colourbar, the lowest substrate surface is presented in black, while the cell appears lighter brown with increasing height

AFM can be operated in multiple different operation modes. Among those is contact mode, where the cantilever tip is in permanent contact with the surface during the sample scanning, or tapping mode, where the cantilever is oscillating at one of its resonance frequencies to repetitively tap the surface in intermitted contact.[68] For this work only contact mode was used. The interaction force between the tip and the surface is maintained constant. The direct measurement of the cantilever deflection (including adjustment of the tip z-position to maintain the force constant) leading to the topography image makes it also the fastest AFM mode.[68,70]

To approach the tip to the surface the following procedure is applied. When a cantilever approaches the surface (zero deflection) it experiences an attractive force and jumps into contact with the sample ('snap-in'). The stronger the cantilever tip is impelled onto the surface, the more it experiences a repulsive force, is bent and applies force to the sample surface. For the scanning process the tip-sample interaction is held at a user selected 'set-point' in the repulsive force range causing a constant deflection of the cantilever during the analysis. As the applied forces between the tip and the surface can be high, lateral forces will appear during the scanning and may damage the surface or the tip. The

scanning results may also produce a deceptive image. A stable attachment of the object on the carrier is necessary to avoid additional sample movement during scanning.[68,70]

This now allows to scan and create topographical sample images but at this stage no chemical analysis can be performed. To do that, a coupling of this method with an additional analysis tool is necessary.

3.2.2.2 AFM-IR

AFM-IR is a hybrid technique which uses an atomic force microscope to detect IR absorption.

The combination of AFM (nanoscale spatial resolution) and IR spectroscopy (chemical selectivity) overcomes both method's limitations and enables measurements to study a materials chemical composition. This can be done with a resolution higher than determined by the diffraction limit considering mid-IR radiation.[71] The technique was first described in 2005 by Dazzi et. al.[59] and is based on thermal expansion of a material after being illuminated with a pulsed IR laser. That response is mechanically registered via a cantilever tip. While for the first version of the system a bottom illumination setting was used, current set-ups possess a top-down illumination.[70]

A schematic representation is illustrated in Figure 13 (a). A pulsed and tuneable IR laser (for example an external cavity quantum cascade laser) is focused on a region of interest on the sample close to the tip. Regarding the sample substrates planar IR-transparent materials can be used like CaF_2 or ZnSe.[70]

When individual sample regions absorb light and thus energy corresponding to one of their absorption bands, their thermal expansion after the IR pulse shock the cantilever into oscillation. This thermal response can be measured by tracking the resulting oscillating cantilever deflection, which is proportional to the absorbance.[59,63] The thermal expansion is, as attested by Dazzi et. al. in 2012[53], directly proportional to the absorption coefficient of the material at the associated wavenumber: The amplitude of the cantilever oscillation, and therefore the detected AFM-IR signal, is proportional to the thermal expansion, which in turn is proportionate to the IR absorption at the corresponding wavenumber. This renders the locally recorded AFM-IR spectra comparable with common FT-IR spectra.[53] Regarding the spatial resolution its magnitude now depends on the contact radius of the cantilever tip instead of the IR wavenumber.[59]

Two different solutions can be considered for IR laser excitation. When using low repetition rates (1-10 kHz), the cantilever response to several pulses are averaged. As described by Lu and Belkin[72], one can also use of several pulses in succession at a higher repetition rate. In this second case the repetition rate is set to match a contact resonance of the cantilever. The resonances of one cantilever are illustrated in Figure 13 (b). In this so-called resonance enhanced mode, the expansion energy is transferred to the selected mode (see Figure 13 (c)). The recorded amplitude of the resonant

cantilever vibration is then proportional to the absorbance of the sample at the excitation wavelength. Mechanical differences in the sample can induce a frequency shift of the mode, which results in the necessity to track the laser repetition rate via a lock-in system.[70,72,73] One example can be phase-locked loop (PLL). This oscillator tracking system is keeping the frequency of the generated output signal constant to an input signal, by fixing the phase of the input and output signal relative to each other.[74]

AFM-IR not only detects the most external layers but also signal from structures beneath the surface. To distinguish the signal coming from the very surface and the rest of the volume, it is possible to use the propagation properties of the acoustic wave generated in the sample after IR absorption. Dazzi et al. (Analytical Chemistry, under revision) and Quaroni[75] refers to these properties.

The resonance frequency in that case has an impact on the probing depth. When the frequency increases, the probing depth decreases. There is also a strong correlation between the probing depth and the lateral resolution, as the thermal expansion exhibits a higher dispersion at deeper sampled volumes. A distinct evaluation of the probing depth is difficult to estimate, since it significantly depends on the mechanical properties of the sample. It is estimated to be up to several hundred nanometres in contact mode. To limit the probing volume, one has to use higher frequency modes. This is of particular interest for cells, since the plasma membrane in which lipid peroxidation is assumed to occur corresponds to the outermost surface layers (average thickness plasma membrane 4-10 nm).[73,76]

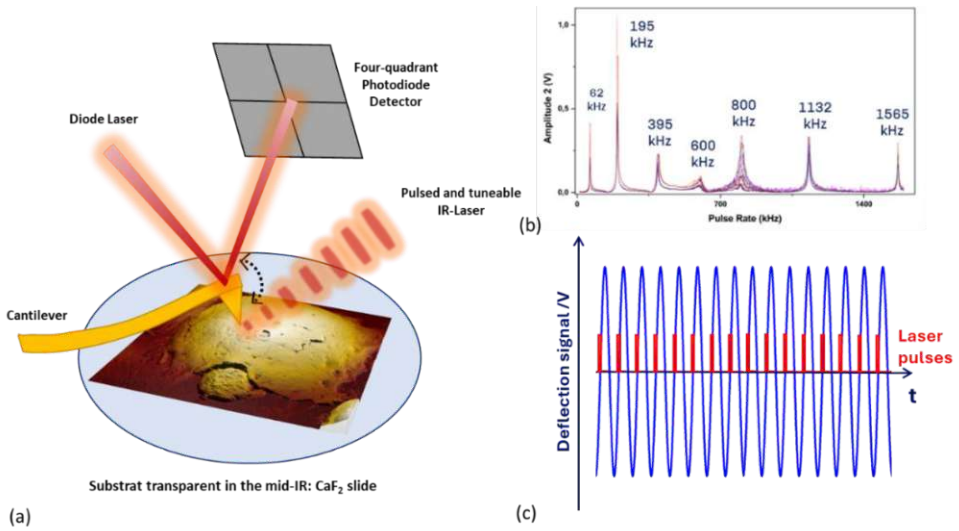

Figure 13: AFM-IR principle

(a) *Illustration of a top-illuminated AFM-IR setup. The basic setup is identical to the AFM before, with the addition of a pulsed and tuneable IR excitation laser focussed on the position under the cantilever tip. (b) Resonance modes of one cantilever give the range 0 – 2 MHz. (c) Representation of a resonance enhanced mode cycle with individual pulses plotted in red and the resulting in the oscillating amplitude of the deflection when choosing one cantilever resonance modes, in blue.*

Two types of measurement or configuration can be chosen to obtain measurements using AFM-IR. The first is chemical mapping, where topography and IR maps are simultaneously recorded by fixing the laser wavenumber to a specific value and then scanning the relevant sample region with the probing tip. This generates a response of the sample to one particular wavenumber, displays the spatial distribution of the absorption intensity and thus the spatial variation of the concentration of absorbing materials (Figure 14 (a) and (b)).[77] To acquire local IR spectra, the tip position is fixed at a specific location while the whole spectral range of the excitation IR laser is scanned. Those local IR spectra are comparable to conventional IR absorbance spectra. (Figure 14 (c)).[53,78]

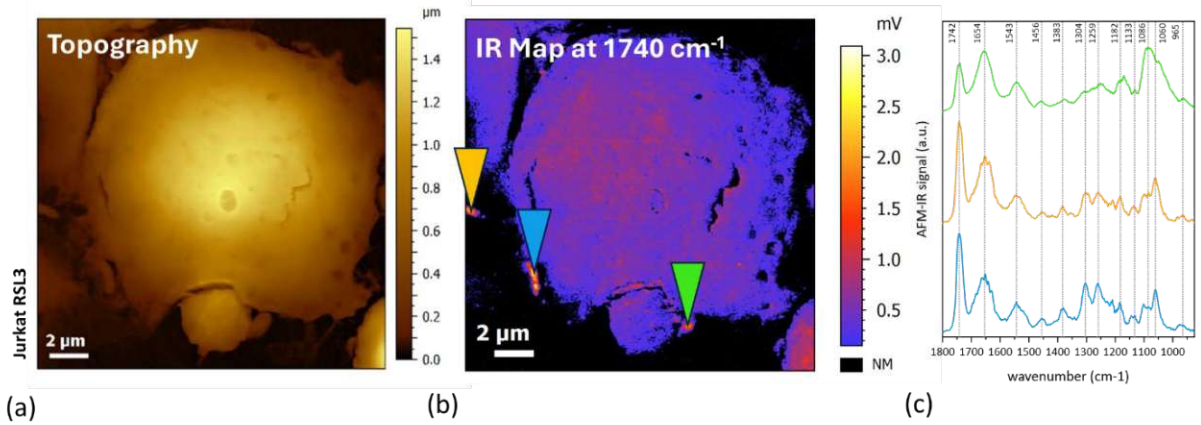

Figure 14: Measurement modes – AFM-IR
(a) *Topography image of a cell acquired in contact mode. (b) IR map of a cell corresponding to wavenumber 1740 cm^{-1}. (c) Local spectra on specific locations, providing precise chemical information at said positions. The individual spectra locations are marked in the IR map in (b).*

It is also possible to acquire hyperspectral data. In this method a full spectrum on each point is acquired. This provides a three-dimensional data array (hyperspectral data cube): Two dimensions containing spatial characteristics and one dimension representing each wavenumber of the spectral range. However, the acquisition requires a longer time period. That means small measurement regions are feasible, which have to be precisely selected.[79] A map containing band heights at 1740 cm^{-1} extracted from recorded AFM-IR spectra compared to an IR map at the respective wavenumber is displayed in Figure 15.

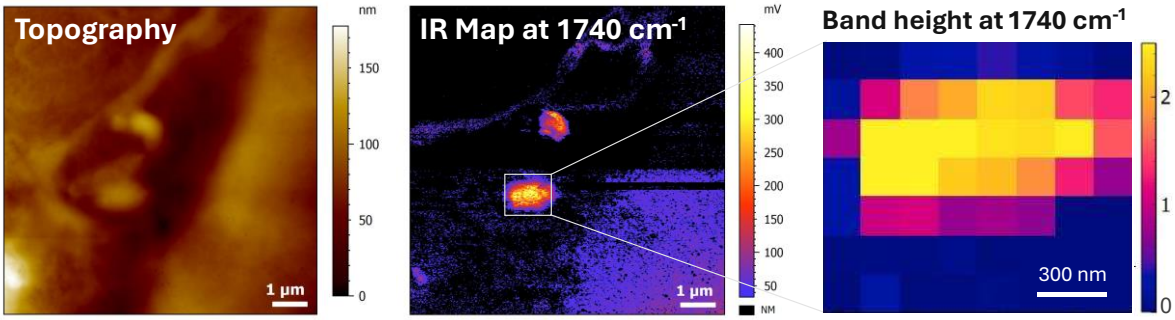

Figure 15: Heatmap at 1740 cm^{-1}
(a) Topography of a cell section of the peripheral cell area (pseudopodia). (b) IR map corresponding to the wavenumber at 1740 cm^{-1}. (c) Based on local spectra acquired, indicated by a white square, a heatmap was generated for the wavenumber 1740 cm^{-1} displaying the respective band heights.

3.3 Aim of this Work

Classical biochemical methods for investigating ferroptosis-induced cell development in particular regarding lipid peroxidation are already in use. However, they lack spatial resolution and the possibility to localise lipid peroxidation occurrences. Some are of destructive nature and cannot provide localised, label-free chemically analysis. Due to these reasons the aim of this work is the establishment of an optimized and validated experimental protocol for sample preparation as well as instrumental conditions for two different analysis techniques O-PTIR (Mirage®, Photothermal Spectroscopy Corp.) and AFM-IR (nanoIR2/Anasys Instruments and ICON-IR/Bruker nano). This protocol is then intended to be tested on two different T-ALL model cell line types (NOTCH1 mutated and non-mutated) for lipid peroxidation, membrane changes and their chemical composition after ferroptosis treatment.

4 Methodology and Protocol for the Analysis of Ferroptosis-Induced Lipid Peroxidation in Immortal Model T-cells

4.1 Optimisation and Validation of the Cell Sample Preparation

Since to best of our knowledge no analysis on this cellular material has been performed using O-PTIR and AFM-IR and the methodology had to be established and optimized. The following points had to be taken into consideration.

As we cannot perform AFM-IR measurements of living cells in water or other liquids (high IR absorption of the solvent itself), the cells have to be fixed and dried. The prepared samples should be compatible with other set-ups, especially a compatibility between AFM-IR and O-PTIR must be guaranteed. The aim was to induce ferroptosis and detect lipid peroxidation impacts on the plasma membranes without drastically impairing the cell integrity. Both nucleus and plasma cell membrane should be preserved. Cell agglomerates and cell multi-layers should be avoided, as clearly defined cells and their immediate surroundings are to be analysed. Individual cells with sufficient distance between them were preferred, and a sufficient number of individual cells had to be guaranteed.

The cell preparation was optimised and validated based on an existing protocol used for other methods. Monitoring analyses were performed previously or in parallel to the optimisation process to ensure successful cell incubation, ferroptosis-treatment and fixation. By combining multiple surveillance systems, a successful optimisation of the cell preparation protocol was targeted. These activities were either performed by the author or members of institute Necker.

These included optical microscopy as a control measure of cell number and integrity after the washing steps of the incubation process and the cell fixation or flow cytometry. Classic viability tests of both cell lines performed by institute INSERM (hospital Necker) (Figure 16), already exhibit a significantly lower viability for the Jurkat than for Loucy the cell line. Non-treated control cells demonstrate less than 50% viability after incubation for 24 hours. The results further indicate that RSL3 has a stronger influence on viability than APR-246. However, it is impossible to draw any conclusions about the cell death mechanism from this alone.

AFM imaging (nanoIR2, Anasys Instruments) was utilised to examine the surface integrity and the presence of nucleus and cell membrane. Large-area scans (80x80µm, 500/500 pt. resolution) of entire cell groups and scans of individual cells (25x25µm, 500/500 pt. resolution) were performed in contact mode (0.4 Hz scan rate). Illustrative topography scans of the initial cell preparation compared to the optimised one are attached in Supplemental Material 1.

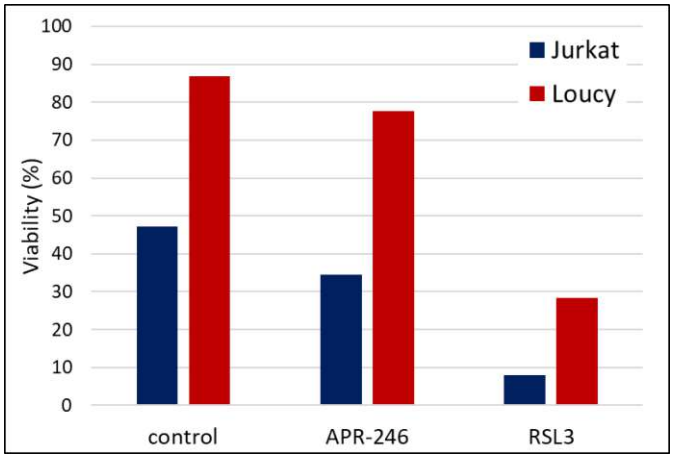

Figure 16: Viability study of both cell lines before and after exposure.
The viability of negative control samples as well as RSL3 and APR-246-treated Jurkat and Loucy cells after 24 hours incubation time were analysed. The control cells of the Jurkat cell line already exhibit a significantly reduced viability, which is further lowered by treatment with APR-246 and RSL3. While APR-246 demonstrates a limited effectiveness in the viability values of both Loucy and Jurkat, RSL3 has a significant influence.

After several protocol variations were tested, the following procedure appeared as most robust and reproducible.

4.1.1 Cell Preparation Protocol

Model cell line storage

The lymphoblastic cell lines Jurkat and Loucy are stored frozen in the vapor phase of liquid nitrogen in complete growth medium augmented with 5 vol-% dimethyl sulfoxide (DMSO) until ready for use.[38]

Growing conditions

Frozen cells, stored in the vapor phase of liquid nitrogen, were defrosted in a 37°C water bath and resuspended in a small amount of tempered RPMI-1640 base medium (Gibco™). This medium was developed to culture human leukemic cells in suspension and contains glutathione as well as high vitamine concentrations. The resuspended cells were then transferred to a 75 cm^2 culture flask containing 20-30 ml RPMI-1640 base medium mixed with fetal bovine serum to a final concentration of 10 vol-% and supplemented with 50 µg/ml streptomycin, 50 IU (international units) penicillin, 2 mM L-glutamine. The cultured cells were grown in suspension, incubated at 37°C in 5% CO_2. The population doubling time was approximately 48 hours for Jurkat and 24 – 36 hours for Loucy.[38]

Ferroptosis treatment

The cell cultures were exposed to the ferroptosis inducers APR-246 and RSL3, control reagent DMSO as well as without added substances (negative control). The influence of DMSO was tested as the solvent was used when preparing the inducer stock solutions and also as high-percentage chemical additive during freeze storage. Suitable stock solutions (10 mM, initial substances diluted in pure DMSO) were prepared for each ferroptosis inducer. 5 ml per model cell line suspension (approximate concentration 1 million cells/ml) were transferred into a separate well of a 6-well-plate for each ferroptosis treatment to where the following amount of inducer stock solution were added:

Table 3: Quantity of reagents required for ferroptosis treatment for cell cultures

Inducer	added volume of stock solution per well	final inducer concentration per well
APR-246	10 µl	20 µM
RSL3	0.5 µl	1 µM

For DMSO-treated cells, a volume of 10 µl was added, which corresponds to the equivalent amount of DMSO in the APR-246 stock solution. The cell cultures were incubated for 6 hours at 37°C with both inducers and DMSO.

Fixation on CaF_2 substrates

For the fixation, the incubated cells were resuspended and 2.5 $\overline{M}$[1] cells per condition were transferred to a well of a 6-wells plate in which a CaF_2 substrate (CRYSTRAN Limited, 13mm dia x 0,5mm polished window) was placed. 3 mL of phosphate-buffered saline (PBS buffer, 1x: pH 7.4, containing 137 mM NaCl, 2.7 mM KCl, 10 mM Na_2HPO_4, and 1.8 mM KH_2PO_4) was added to each well, the plate was gently agitated, centrifuged for 5 min at 1500 rpm and the supernatant was removed. The cells were fixed with 2 mL of 4% paraformaldehyde solution (PFA dissolved in PBS, 4°C, Thermo scientific) for 10 min before again adding 3 mL PBS buffer to stop the fixation process. Centrifugation was repeated as before, and the batches were examined for the number and distribution of cells using a light microscope. In the following washing steps, the concentration of PBS was gradually decreased in order to remove PBS residues without inducing stress to the cells. The cells were washed with 3 mL 50/50 vol-% PBS/water, carefully agitated, centrifuged (5 min, 1500 rpm) and the supernatant was

[1] $\overline{M}$ = Mio. cells

removed. This procedure was repeated with 25/75 vol-% PBS/water and twice with pure distilled water. During the last washing step, instead of removing the supernatant, the CaF_2 substrate was directly removed from the wells, the edges dried with paper towels before being placed on a microscope slide, to avoid cell loss during the aspiration step and to keep the residual liquid quantity as low as possible. The cells were checked again using a light microscope

Once the samples were completely dried, the substrates were attached to round metal supports using adhesive films.

4.2 Instruments and Measurement Conditions

4.2.1 O-PTIR – Submicrometric Analysis

O-PTIR was used to obtain characteristic mid-IR spectra of each cell condition.

A mIRage® setup (Photothermal Spectroscopy Corp.) was used coupled with a MIRcat-QT QCL laser (Daylight solutions®) covering the spectral range between 900 – 2000 cm^{-1} (max. average power 40mW).

Spectra were recorded in a spectral range from 941 - 1905 cm^{-1} (resolution 1 cm^{-1}) with an IR laser repetition rate of 100 kHz, 400 ns pulse width and 6% IR power using an APD (avalanche photodiode) detector. The probing laser wavelength was 532 nm at 0.22% laser power capacity. The percentage values refer to setting options on the device in relation to the maximum laser power. It was not possible to specify the absolute values.

For a mean analysis of each cell condition, 10 spectra (each 4 repetitions) on arbitrary chosen locations for 15 cells were recorded.

4.2.2 AFM-IR – Nanometric Analysis

The sample analysis via AFM-IR was structured in multiple subsidiary tasks. The main part of AFM-IR measurements was performed on a nanoIR2-system (Anasys Instruments). First, an investigation of the obtained probing volumes under the tip of the used cantilever type for varying pulse frequencies, pulse widths and laser powers was performed. A control sample consisting of PMMA on silicon was chosen for this experiment to simulate equivalent mechanical sample properties as for cells on CaF_2.

Since ferroptosis-induced lipid peroxidation is a local phenomenon generally located in the phospholipid bilayer on the surface of the cell, only the cell membrane should be sampled. This can be achieved by reducing the probing depth as much as possible. If the whole cell is analysed, the signal

coming from the subjacent cytoplasm would mask the signal coming from the superficial lipid plasma membrane. Therefore, a protocol only detecting the signal from the surface has to be established.

Following this, a suitable instrumental protocol for cells was developed using the nanoIR2-system. The Jurkat cell line was used to optimise the protocol. To confirm applicability of the established protocol on cells, both cell lines were tested in multiple conditions using IR maps and local spectra (arrays). In addition, AFM-IR analysis (IR maps and local spectra) was performed on Jurkat cells treated with RSL3 using a second AFM-IR system (ICON-IR). These cells were chosen because of the classical viability experiment as well as its promising results when acquiring IR maps and local spectra on the nanoIR2. The ICON-IR was selected due to its precise tip movement ability and its minor thermal drift during long term measurements.

The nanoIR2 AFM-IR system (Anasys Instruments) is coupled with a MIRcat-QT QCL laser (Daylight solutions®) covering the spectral range between 884 – 2000 cm^{-1} (max. average power 40mW). Imaging and spectra were acquired in contact mode using gold coated cantilevers (Mikromash series HQ:CSC38, cantilever B). The used cantilevers had spring constant of 0.03 N/m (0.003 – 0.13 N/m) and 10 kHz (5 – 17 kHz) resonance frequency. The following dimension can be observed: A length of 350 µm
(1 - 355µm), width 32.5 µm (29.5 - 35.5µm) and thickness of 1µm (0.5 - 1.5 µm). The rotated tip is 15 µm (12 - 18 µm) high, displays 40° full cone angle and the tip diameter is < 35 nm.

4.2.2.1 AFM-IR Surface Analysis: Optimization of the Acquisition Parameters

This experiment aimed to optimize the different laser parameter: pulse frequencies, pulse rates and laser powers during scanning. In previous observations, it is confirmed that individual pulse rates result in stagnating amplitude signals even when sample thicknesses increase. This indicates a limited probing depth for certain conditions.

A reference sample consisting of a polymethyl methacrylate (PMMA) wedge layer on silicon was used to calibrate the previously described cantilever (Mikromash series HQ:CSC38, overall gold coated, cantilever B). The assembly of PMMA on Si was specifically chosen to approximate the mechanical behaviour of the cell on a rigid substrate (CaF_2). The increase in thickness of the PMMA film evolved steadily in an 45° angle before reaching a maximum around 600 nm.

An area of 4x40 µm was mapped at a scan rate of 0.2 Hz (nanoIR2) with a resolution of Res X/Y: 800/80 pt. The selected wave number was 1725 cm^{-1} targeting PMMAs C=O stretching bond (PLL was applied). Laser power (0.26, 0.6, 1.09 %) as well as pulse width (60 – 160 ns) were varied for

the stable cantilever frequency modes (197 kHz, 805 kHz, 1.14 MHz, 1.57 MHz). The laser power was deliberately set low to avoid damaging the sample.

The measured area is illustrated in Figure 17.

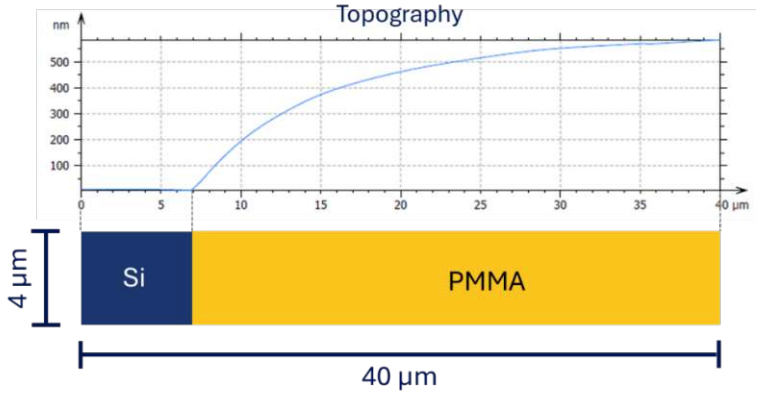

Figure 17: Schematic representation of the reference sample
The reference sample consisted of a PMMA wedge film on silicon. The transition from Si to PMMA started steadily followed by a stagnating levelling. The measured area was sized 4x40 µm and up to 600 nm in height.

For the evaluation of the probing depth only 10 lines in the centre of the IR map were considered and averaged. The reason for this was that the diverging topography differences over the entire distance of 4 µm.

Every combination of settings mentioned was systematically analysed. If it had already become apparent during the scanning of the pulse sweep (rapid search for the amplitude maximum) that individual measurement combinations were not stable, these were not included in the creation of an IR map.

The first step was to analyse the position and stability of the frequency amplitudes of the individual cantilever modes for the entire range from 0 - 2000 kHz (Figure 18). In addition to the first mode (63 kHz), six other modes were recognisable. Four modes (excluding the first) had a symmetrical shape with a slight tailing. Although the peak at 395 kHz gave a reproducible signal shape, a coupling with 599 kHz was identified. If 395 kHz or 599 kHz were selected, the excitation of the other was non-negligible, especially when the laser power was continually increased. Consequently, both frequencies (pulse rates) were excluded for the upcoming tests. Irregular peak shapes were recognized at 802 kHz, especially for lower amplitude signals. These ones were also excluded for the following IR maps.

The maxima of the selected frequencies were located at 197 kHz, 802 kHz, 1.13 MHz and 1.57 MHz, as displayed in Figure 18. The full width at half maximum (FWHM) showed a similar error margin for 197 kHz: 2.6±0.4 kHz (15%), 802 kHz: 29±3.9 kHz (13%) and 1567 kHz: 6.0±0.8 kHz (13%) Further information on the peak behaviour of the amplitudes of the different frequencies can be found in the appendix (Supplemental Material 4).

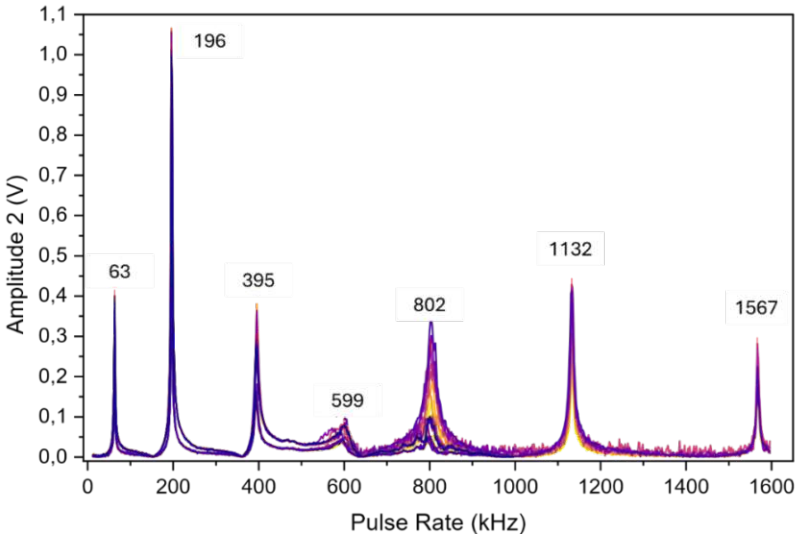

Figure 18: Resonance modes of the used cantilever
Pulse sweep (0-2000kHz) to distinguish the resonance modes of Mikromash series HQ:CSC38, cantilever B (spring constant: 0.03 N/m (0.003 – 0.13 N/m) , fundamental mode: 63 kHz) at the pulse width range from 60 - 200 ns, in each case with 0.26% and 0.6% laser power. The pulse sweep was performed in the middle of the PMMA film, in an adequate distance to the border area to Si.

In Figure 19 the topography (green), IR amplitude curve progression (blue) and resonance frequency shift (red) is illustratively described for the resonance frequency at 1565 kHz, 80 ns pulse width and 1.09 % laser power. Phase-locked loop (PLL) was used as tracking system to follow the shift in resonance frequency when transitioning from Si to PMMA.

The topography curve (green) displays an even signal increase after reaching the PMMA film, but with progressively decreasing gradient.

The IR amplitude (light blue, min. and max. values in dark blue) indicates a rapid increase, before stabilising after 1 µm distance on PMMA and maintaining this signal level despite the increasing thickness of the PMMA film. Between 30 and 40 µm measuring distance the amplitude signal declines again to a lower signal level. This behaviour has been observed repeatedly, regardless of pulse rate, pulse width and laser intensity. It was also tested whether the selected sample position was the factor of influence due to irregularities in the PMMA surface. It might originate from reflections in the thin

film or some unknown PMMA film and Si substrate interaction. Irregularities underneath the surface can also be a reason for observed signal progression.

The resonance frequency tracked via PLL (red) undergoes a change from 1569 kHz to 1565 kHz when moving the tip from Si (where no C=O signal of the PMMA should be present) to PMMA. The resonance frequency position shows afterwards subsequent levelling. This curve is proportional to the increase and stagnation of the amplitude signal. However, the position of the resonance frequency is not constant but rather oscillates before it declines like the IR amplitude intensity.

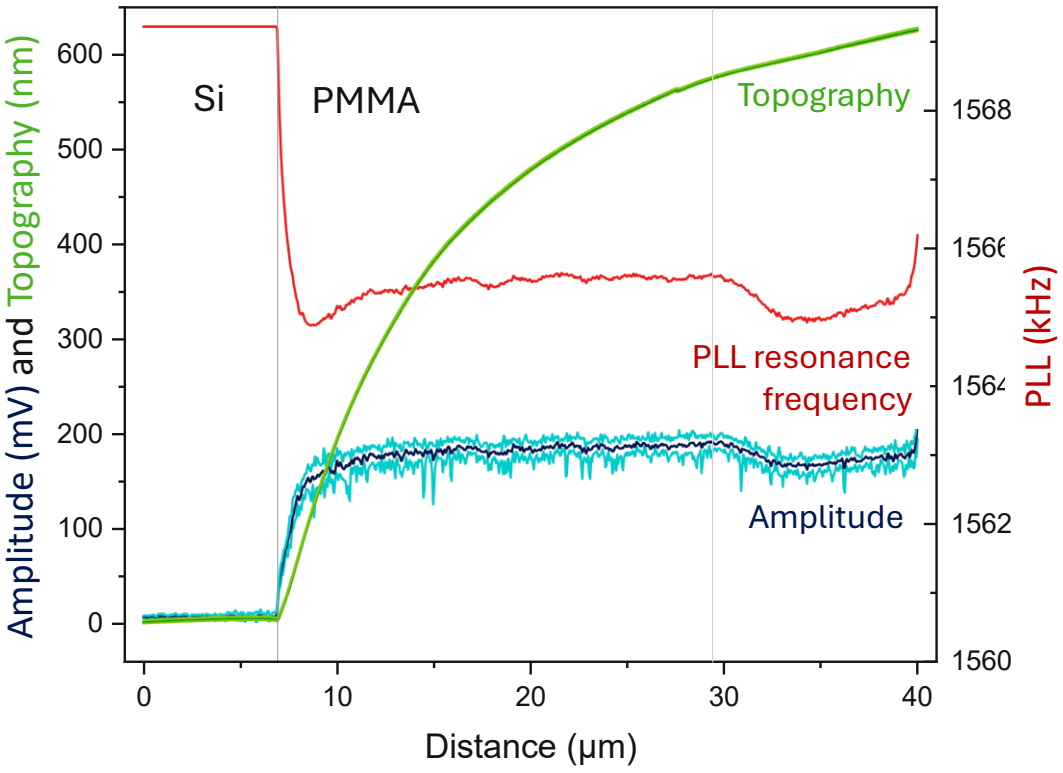

Figure 19: Topography, IR amplitude and the PLL resonance frequency curves) of the Si-PMMA transition
Illustrative representation of the topography, amplitude and PLL amplitude signal curves from Si to PMMA for mode 1565 kHz at 80 ns pulse width and 1.09 % laser power. For the amplitude the mean value (light blue) as well as minimal and maximal values (dark blue) are included. All curves appear constant for the Si area before increasing steadily (topography) or abruptly increasing/declining and then flattening (IR amplitude/PLL resonance frequency position) when scanning from Si to PMMA.

To investigate the change the frequency of the amplitude maximum in more detail, the progression of the position change was looked in more detail. While the frequency positions at the Si/PMMA border remained the unchanged at 195 kHz, 1134 kHz and 1567 kHz, the amplitude of the frequency 802 kHz shifted to values around 772 kHz. This indicates a tendency of higher stabilities of the frequency modes 195 kHz, 1134 kHz and 1567 kHz even with fluctuating mechanical sample properties. These

results also demonstrate a shift of the resonance frequencies (with relatively identical curves) to lower values with increasing pulse width.

A display of all PLL plots for the progression of the position change for each measurement setting is available in Supplemental Material 2 and 3.

To determine the PMMA film thickness at which the IR amplitude stagnation occurs, the amplitude intensity curve was scaled to the respective sample thickness and this curve was fitted according to the following equation Eq. (2). The formula was based on experiments from Dazzi et al. (Analytical Chemistry, under revision). Since the structure of the reference sample differs from Dazzi's (PS on PMMA), an additional exponential term was included, to address the impact of Si's high stiffness on the thinnest parts of PMMA.

$$y = y_0 + A_1 \cdot e^{\left(-\frac{x}{m_1}\right)} + A_2 \cdot e^{\left(-\frac{x}{m_2}\right)} \qquad \text{Eq. (2)}$$

To calculate the probing depth, the IR amplitude signal was plotted against the topography curve of the PMMA film. The curve for pulse frequency 1565 kHz at 80 ns pulse width and 1.09 % laser is illustratively displayed in Figure 20. The mean curve progression (light blue) as well as maximum and minimum limit (dark blue curves) are included. The first nanometres for the transitioning from Si on PMMA were excluded due to extensive noise as wells as the section above 550 nm film thickness. All three curves are fitted using equation Eq. (2). The fits are plotted as red dotted lines.

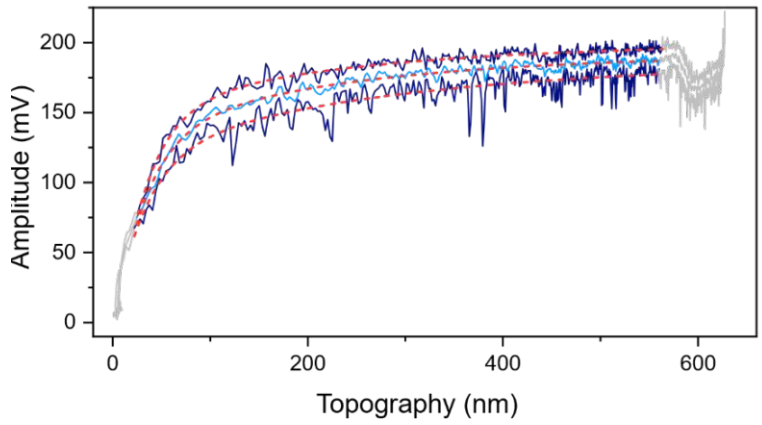

Figure 20: Illustration of the IR amplitude progression overt the PMMA height.
The illustration highlights the IR amplitude against the PMMA topography curve for the condition 1565 kHz at 80 ns pulse width and 1.09 % laser power: The mean curve progression (light blue) as well as maximum and minimum limit (dark blue). All three curves are fitted (red dotted lines) using Eq. (2). The first part on Si and the direct transition sequence are not included for fitting (shifts trough changing mechanical properties). Also, the last curve proportion was disregarded due to an unknown IR signal decrease.

The results indicate a tendency towards lower probing volumes at higher pulse frequencies. A change of power had as expected no impact on the probing depth. The influence from the pulse width variations were small and inconclusive. The values were also within the standard deviation range of each other, so no clear statement is possible. The highest impact was caused by the pulse frequency resulting in major changes of the probing depth. The probing depth was around 198 nm (range 166 – 236 nm) for 200 kHz decreasing to 64 nm (61 – 67 nm) for 800 kHz. The pulse frequency of 1155 kHz resulted in 48 nm (43 – 53 nm) probing depth and 30 nm (28– 33 nm) for 1565 kHz.

This first evaluation of the probed volume under the tip gives a preliminary estimate. No statistical statement guaranteeing quantitative reference values for other sample variations can be given, as the design and mechanical properties of the reference sample were specifically adapted to the used cell samples. Only the tendency of the probing depth can be used for cell measurements.

4.2.2.2 Optimization of an AFM-IR Protocol for the Investigation of Artificially Induced Ferroptotic Lipid Peroxidation on Cells

The optimisation of the methodology protocol for AFM-IR was carried out in several steps, whereby the signal stability of the IR amplitude was tested for different pulse width/pulse rate settings. The most suitable combinations were then tested on different areas of the cell and at the boundary to CaF_2. This was done by pulse sweeps, but IR map scans and local spectra were also recorded. To establish an instrument protocol, the model cell line Jurkat was used. Subsequently a DMSO treated Jurkat cell was analysed at several pulse rates. IR maps and mean spectra at different pulse frequencies were then compared with each other.

Based on the results of the probing depth study, a selected pool of pulse width/pulse rate/laser power combinations was chosen. These were used to perform pulse sweeps in the centre of a cell (Jurkat DMSO). The results are visualised in Figure 21.

The laser power was increased up to 5.77 % due to the reduced signal response of the cell to the excitation laser compared to PMMA. This did not result in any recognisable damage to the cells despite repeated use.

Based on the preliminary results of the cantilever probing depth study on PMMA, the frequencies 197, 841, 1153 and 1577 kHz were used for further investigations. A shift in the amplitude frequency but also a change of peak widths FWHM (54±7.2 kHz) can be seen for the mode at 841±9.3 kHz. The other three modes, display consistent amplitude positions and persistent peak shapes at 196±0.6 kHz (FWHM: 5.1±0.3 kHz), 1153±2.5 kHz (FWHM: 23±1.8 kHz) and 1577±1.1 kHz (FWHM: 11±0.9 kHz).

Although the amplitude at 397 kHz is also included in this figure, a coupling with 600-650 kHz (not marked in the image) was again be observed, which makes it not suitable for the experiments.

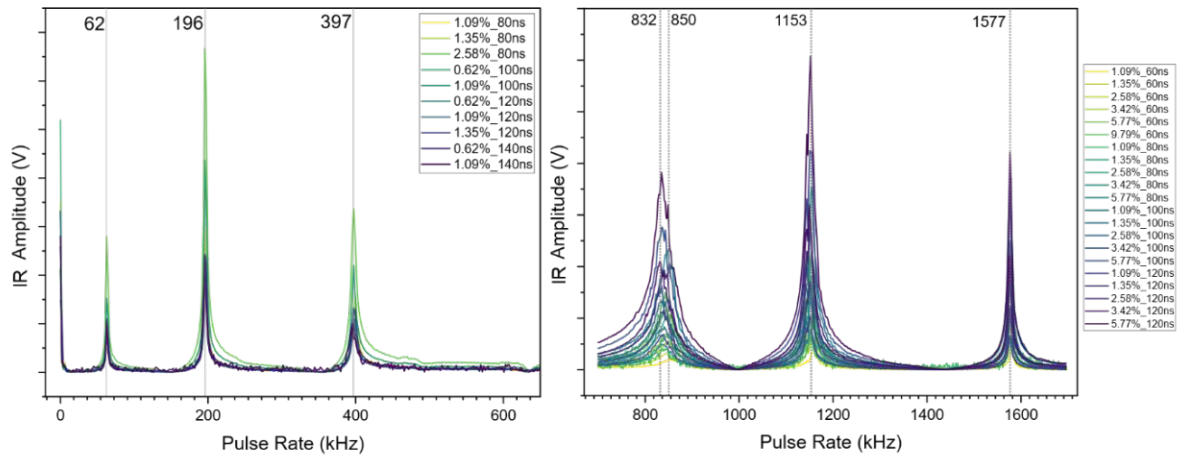

Figure 21: IR Amplitude maxima of the different pulse rates.
The IR maxima positions (wavenumber 1650 cm^{-1}) for all resonance modes of one cantilever on the cell centre (Jurkat DMSO) for pulse widths between 60 – 140 ns and laser powers ranging from 1.09% to 5.77% are presented. .

In this first investigation of cells, we clearly observe that some modes are generally more stable in maximum position and peak shape than others (196, 1153 and 1577 kHz). Stable bands with high IR amplitude maxima values were found at 100 ns and 120 ns pulse widths (low resonance frequencies) as well as 80 ns and 100 ns (high resonance frequencies). The measurement conditions are now narrowed towards these pulse widths with a special focus on 100 ns.

Subsequently, pulse sweeps (0-2000 kHz) of these restricted instrument settings were tested at several positions in the cell centre, the border between nucleus and cytoplasm as wells as the border region between cell and CaF_2. These pulse sweeps are plotted illustratively for 100 ns pulse width and 3.42% laser power in Figure 22.

Peak splitting at the cell/CaF_2 border for frequency 1146 kHz can be caused by mode overlapping due to suddenly changing mechanical behaviour of the underground. The second mode has a minimal shift of its frequency (198±1.2 kHz) and its FWHM (5.5±0.5 kHz) demonstrates reproducible peak shapes for the individual sample positions. Also, the mode at 1575 kHz is reproducible regarding frequency (1575±3.8 kHz) and FWHM (12±2.2 kHz).

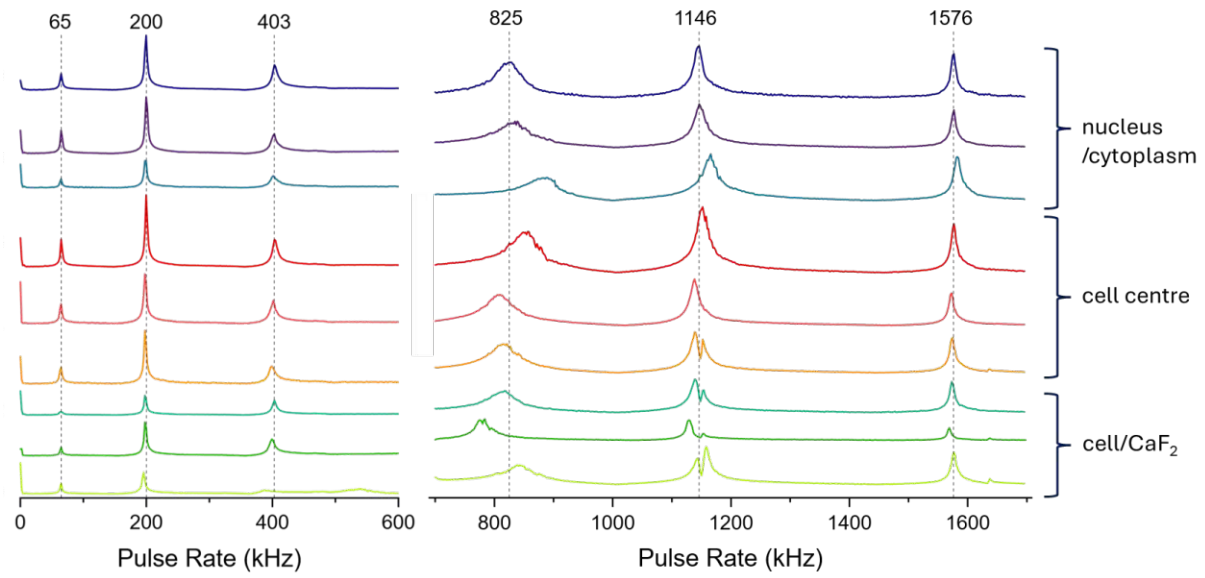

Figure 22: Amplitude maxima locations on varying cell positions
The amplitude maxima of the different frequency modes on different positions of a cell (Jurkat DMSO) are displayed for a 100 ns pulse width using 3.42% laser power at wavenumber 1650 cm^{-1}.

Since the pulse width of 100 ns provides the most reproducible values for both lower and higher frequencies also regarding different laser powers, it was chosen for the recording of IR maps and local spectra. A later discovered problem was that the first laser chip of the nanoIR2 was unreliable for these setting resulting in a cut of the spectral range (1280-1240 cm^{-1}).

These conclusions were now verified using a DMSO treated Jurkat control cell.

Probing the entire cell volume and the surface for control sample Jurkat DMSO

As a reminder the estimated probing depths were about 198 nm (range 166 – 236 nm) for 200 kHz and 30 nm (28– 33 nm) for 1565 kHz. This indicates that at 200 kHz the cytoplasm is analysed, while at 1565 kHz primarily the membrane and a small amount of cytoplasm are probed.

Dimethylsulfoxide (DMSO) treated cells were tested to verify a potential impact on cells, since the chemical was used as solvent for the ferroptosis-inducers as well as high-percentage used freeze protection agent for cell culture storage. The incubation concentration was equal to the amount in the injected ferroptosis-inducer solutions.

IR maps at 1650 cm^{-1} (amide I) and 1740 cm^{-1} (C=O stretching band, phospholipids) were recorded for the pulse rates 195, 1155 and 1565 kHz and their ratios determined. The topography as well as all IR map ratios are displayed in Figure 23 for the two modes 195 and 1565 kHz. 1155 kHz proved to be too unstable.

For both IR ratio maps, a mostly uniform signal across the whole cell is noticeable. The pulse frequency at 200 kHz showed slightly increased values and particularly ratio maxima responses in the peripheral areas of the cell. Exceptionally increased ratio for higher pulse frequencies at 1565 kHz were noticeable. These prominent values for the 1740/1650 cm^{-1} ratio can be an indication of lipid peroxidation.

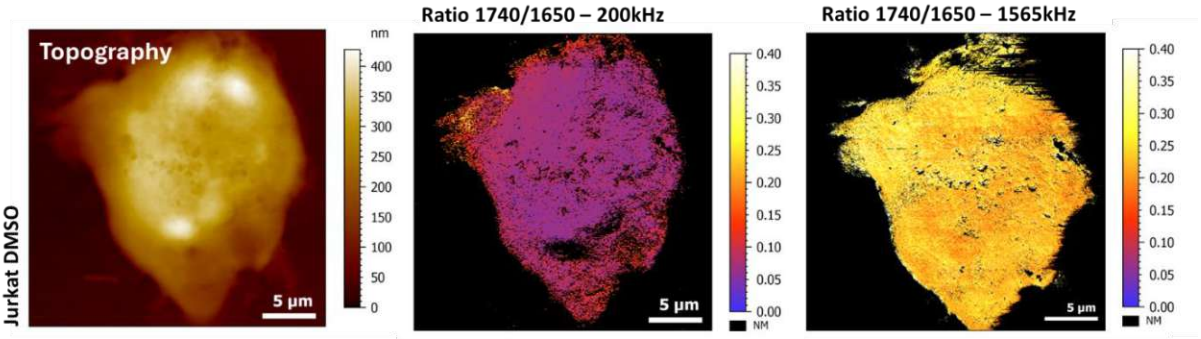

Figure 23: Topography and IR map ratios DMSO-treated Jurkat cell
The topography image as well as IR map ratios between 1740/1650 cm^{-1} of a DMSO-treated Jurkat cell for the pulse rates 200 kHz and 1565 kHz using 100 ns pulse width are presented. The IR maps were recorded at different laser powers. This was compensated for by calculating a factor of the different signal intensity of the IR background. Non measured points (NM) are displayed in black.

Mean spectra of DMSO treated Jurkat sample were calculated for each mode, based on at least 100 local spectra distributed on the main cell part (Supplemental Material 5), but they display a typical IR without a visible 1740 cm^{-1} band due to the averaging.

Since phospholipids accumulations are local phenomena on the lipidic plasma membrane bilayer, distinct local spectra at the highest pulse frequency were recorded as featured in Figure 24.

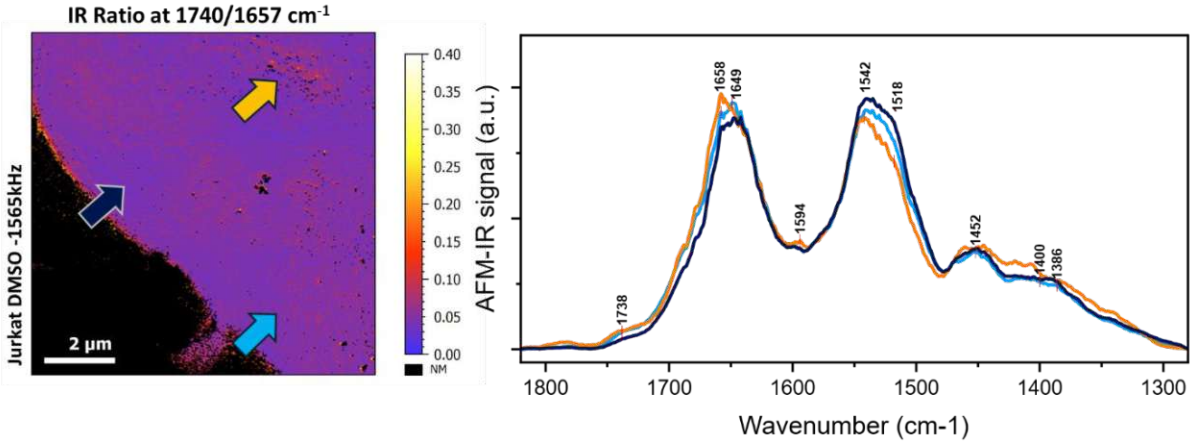

Figure 24: Local spectra on a DMSO treated Jurkat cell
Based on an IR map ratio 174/1657 cm^{-1} section on the previously presented DMSO-treated Jurkat cell measured at 1565 kHz pulse rate, spectra locations were selected. The local spectra were acquired on positions with high (dark blue), intermediate (blue) and low (orange) ratio values.

Based on these results it was proposed to use two different pulse rates for the investigation of the two model cell line at multiple treatment conditions. One to probe also the cytoplasmic volume of the cell one to only probe the surface. Since 197 kHz and 1575 kHz demonstrated the most stable modes, especially regarding the amplitude signal stability, shift and peak broadening for heterogenous mechanical sample characteristics, these specific pulse rates were chosen for further measurements.

Additional emerging difficulties in method development for IR map scanning and local spectra

- Thermal drift and diverging spectra positioning

One problem was the exact tip positioning for recording local spectra. As highlighted in Figure 25, specific positions for acquiring full spectra based on an IR map at 1740 cm^{-1} were chosen. The actual localisations based on the acquired heatmaps (marked by white rectangle) differed from the targeted positions (marked in black). That is due to thermal drift of the sample during the measurement but also imprecise targeting possibilities of the instrument itself. In the presented case, it was around 250 nm difference between the IR map at 1740 cm^{-1} and the hyperspectrum created from the local spectra array. Since lipid peroxidation accumulations are expected to be in the nanometre range, the exact setting of the nanoIR2 poses a considerable problem.

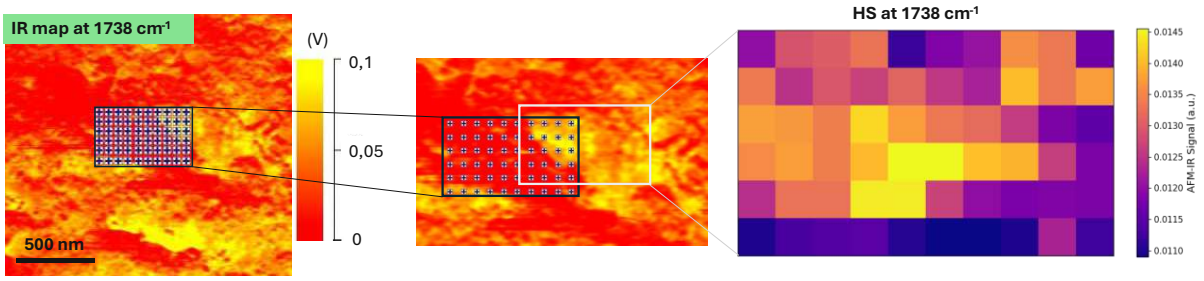

Figure 25: Illustration of thermal drift during AFM-IR measurements
The thermal drift occurring during IR map scanning as well as local spectra acquiring was a significant problem. It resulted in inaccurate spectra locations which is highlighted using an IR map with immediate subsequent measurement of an array of local spectra. The original chosen ratio is marked with a black box while the white box represents the location derived from an hyperspectrum at 1738 cm^{-1}. A clear deviation from the originally selected spectrum positions is notable.

- Instabilities for large-area scans in IR maps

Another irregularity was the incompleteness of some of the IR maps. As a result, the IR map ratios were only available in partial sections. In some cases, the PLL was unable to follow the resonance frequency as it shifted drastically during the scan (Figure 26: Jurkat APR-246). This occurred particularly with nearly hemispherical cells after the maximum of the cell topography was exceeded and especially with the wavenumber 1740 cm^{-1}. In the shown case the scan was performed from the bottom to the top, but the PLL gradually lost the resonance frequency. The second problem was loss of contact between the cantilever and the surface. The Jurkat RSL3 cell in Figure 26 illustrates that especially cell membrane irregularities (perforated indentation on the left side) and large heights cause contact losses.

An improvement in map quality was achieved by lowering the scan rate to 0.2 Hz or less, which then again significantly increased the measurement time and the thermal drift rate. For low signals, especially for 1740 cm^{-1}, the laser power was also increased up until 10% (setting of the instrument in relation to maximum laser power). By scanning smaller sections of the cells (Figure 26 last row) these irregularities were reduced. In addition, it was advantageous to decide whether to scan from top to bottom or vice versa based on the shape of the cell and to directly start the scan on the border between CaF_2 and the cell.

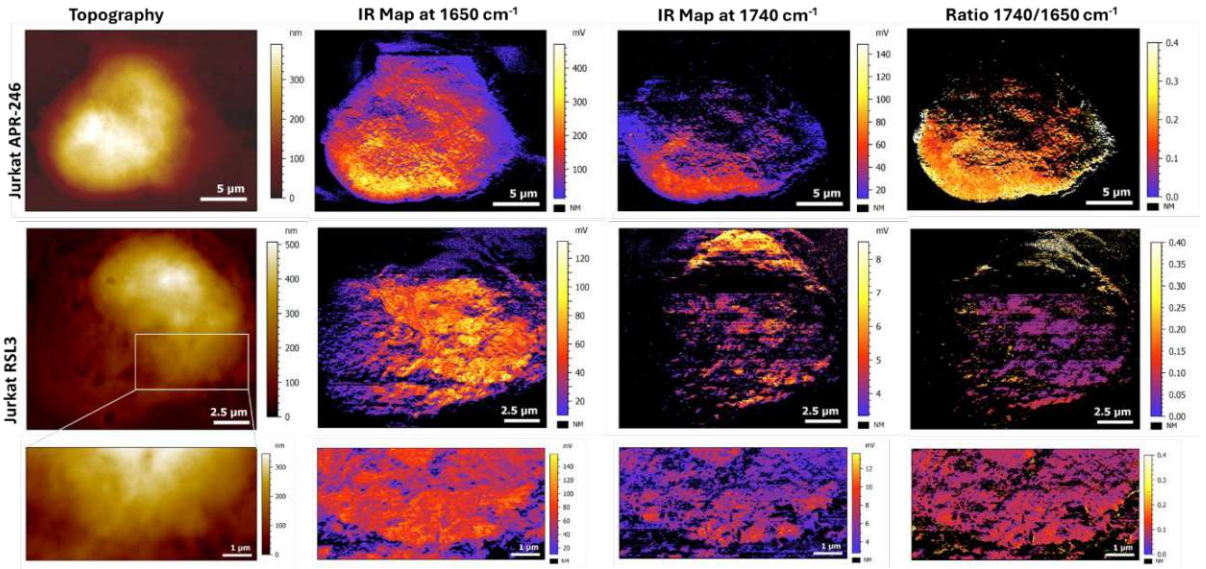

Figure 26: Evaluation of IR map irregularities based on IR map scans of Jurkat RSL3 and APR-246
From left to right: The topography as well as the individual IR maps at and 1650 cm^{-1} and 1740 cm^{-1} for 1565 kHz pulse rates are provided. The PLL was no longer able to follow the signal amplitude (1740 cm^{-1}) for Jurkat APR-246.For Jurkat RSL3 an abrupt contact loss between cantilever tip and sample in the upper cell area can be observed. The last column represents the IR map ratio between both wavenumbers of each cell. A dataset of a zoom section of Jurkat RSL3-treated is also enclosed and presents the improvement of the map quality when focussing on small sections.

4.2.2.3 Final AFM-IR Protocol

NanoIR2 Analysis

Local spectra and hyperspectral maps were recorded by fixing the AFM tip position and tuning the laser source between 1200 – 1900 cm^{-1} (resolution 1 cm^{-1}), probing the whole cell (IR laser pulse rate around 190 kHz) as well as the membrane surface (various pulse rates between 1320 kHz – 1575 kHz depending on the cantilever) at 100 ns pulse width using 3.44% laser power. IR maps were acquired by scanning the surface at fixed wavenumbers, at a scan rate between 0.15 to 0.2 Hz using up to 9.77% laser power (resonance frequency tracking by PLL).

Two to four cells per model cell line and treatment condition were examined.

ICON-IR Analysis

ICON-IR was used to analyse RSL3-treated Jurkat cells and to obtain precise local spectra also covering the spectral range 1280-900 cm^{-1}.

Additional images and spectra were recorded using an Icon-IR (Bruker Nano) coupled with an EC-QCL (Daylight Solutions®) covering the IR range from 900 cm^{-1} to 1900 cm^{-1}. Imaging as well as local spectra were recorded in contact mode using gold coated cantilevers (Mikromash series HQ:CSC38).

Spectra were acquired from 1900 to 900 cm^{-1} with a 1 cm^{-1} spectral resolution, at 1250 kHz and 100 ns laser pulse width and 1.8% laser power (setting of the instrument in relation to maximum laser power). IR maps were obtained using a scan rate of 0.3 Hz with a laser power around 0.8 – 1.8%.

Exclusively RSL3-treated Jurkat cells were analysed using the ICON-IR.

4.3 Spectral Processing and Data Analysis

4.3.1 IR maps

AFM-IR topography and IR maps were analysed using the MountainsMap software v.9.1 to v10.1 (Digital Surf).

The topography maps were height corrected, levelled and overlayed taking the topography as reference before colocalization procedure. IR maps of the same area at multiple wavenumbers taken with different laser powers were power corrected by calculating the detector response based on recorded the IR backgrounds, before compiling IR ratios and overlays of IR maps.

4.3.2 Local Spectra

All spectra were laser chip transition corrected to compensate the offset between the individual chips of the laser using a Python script made by the AFM-IR research group, Institute Chimie-Physique, Université Paris-Saclay. These occur at 1693 cm^{-1}, 1433 cm^{-1}, 1205 cm^{-1} (O-PTIR), 1675 cm^{-1}, 1477 cm^{-1}, 1171 cm^{-1} (nanoIR2) as well as 1706 cm^{-1}, 1411 cm^{-1}, 1209 cm^{-1} (ICON-IR). For pre-treatment and analysis of the data the software Orange DataMining v3.36.2, OriginPro 2023b and the programming language Python including various packages were used.

Pre-treatment of the spectra included baseline correction (Rubber band function), Savitzky–Golay smoothing (first derivative order, window size 5 (O-PTIR) or 13 (AFM-IR)) and vector normalization.

4.3.3 k-means Clustering

K-means clustering was performed on data sets of different sample conditions for cluster analysis to identify similarity structures in the given data sets.

The approved clustering algorithm k-means aims to sort a number of ‘n’ observations in a number of ‘k’ clusters by iteratively calculating the minimal mean cluster centres. The initialization starts with assigning primary, not-optimal clusters (fixed cluster set or a fluctuating number limit) and then calculating the minimum mean value of the current observation points per cluster which returns the new location of the centre cluster value. This process is repeated until a chosen convergence criterium is reached. For the application, the extension kmeans++ in Quasar (v2.16.6) was chosen, which does

not randomly select the initial cluster centres for k-means, but has a preliminary step in which a pre-assortment for the later start value of the clustering is determined.[80]

K-means clustering was carried out using the 2nd derivatives of the O-PTIR spectra from 1800-1300 cm^{-1} (additional Gaussian smoothing factor 1). Initialization was performed via the kmeans++ algorithm for 10 re-runs using a maximum of 300 iterations.

5 Application of the Established Protocols on Cell Lines Undergoing Ferroptosis-Induction

5.1 Global Analysis of the Samples using O-PTIR techniques

OPTIR was used to perform a global analysis of the cells for each condition.

5.1.1 Infrared Response of Reference Cell Lines *Loucy* and *Jurkat*

The first step entailed a comparison of the two untreated cell lines with each other (Figure 27). As stated before, Loucy was defined as reference cell line. It has no NOTCH1 mutation but instead a mutation on the oncogene p53. Jurkat has a NOTCH1 mutation and was expected to feature an enhanced sensibility to the ferroptosis-inducer, as previous results from Failla[32] stated.

For this purpose, averaged spectra from 15 cells and 10 different locations per cell (4 spectra per location) were compared. The mean spectra from Loucy and Jurkat reveal bands at 1743 cm^{-1} (C=O stretching), 1655 cm^{-1} (amide I), 1545 cm^{-1} (amide II), 1455 cm^{-1} (CH_2 scissoring), 1399 cm^{-1} (CH_3 symmetric bending), antisymmetric and symmetric phosphate bands at 1249 and 1085 cm^{-1} (shoulder at 1057 cm^{-1}) as well as 969 cm^{-1} (nucleic acid band). The 2nd derivative spectra additionally feature band shoulders at 1715 cm^{-1} and 1685 cm^{-1}. Between the amide I and II band, also bands at 1599 cm^{-1} and 1575 cm^{-1} appear. These can be assigned to antisymmetric carboxylate stretching vibrations lipidic structures.[45,50] The amide II band also features a band shoulder at 1517 cm^{-1}.

The cell species' spectra shape appears to be consistent, except for the distinctly pronounced band at 1741 cm^{-1} for Jurkat. Further, minor discrepancies including the band 1715 cm^{-1} assigned to C=O stretching of carbonic or nucleic acids (increased for Loucy), the transition between amide I and II and the symmetrical phosphate band (1085 cm^{-1}) are located within each other's standard deviation range.

The results of the viability analysis of the two cell lines (see section in 4.1) demonstrated a cell viability of around 50% for non-treated Jurkat cells. This was considerably lower than the cell viability of Loucy and could be the reason for Jurkats' already prominent 1741 cm^{-1} band, probably indicating the presence of esterified and peroxidized phospholipids.

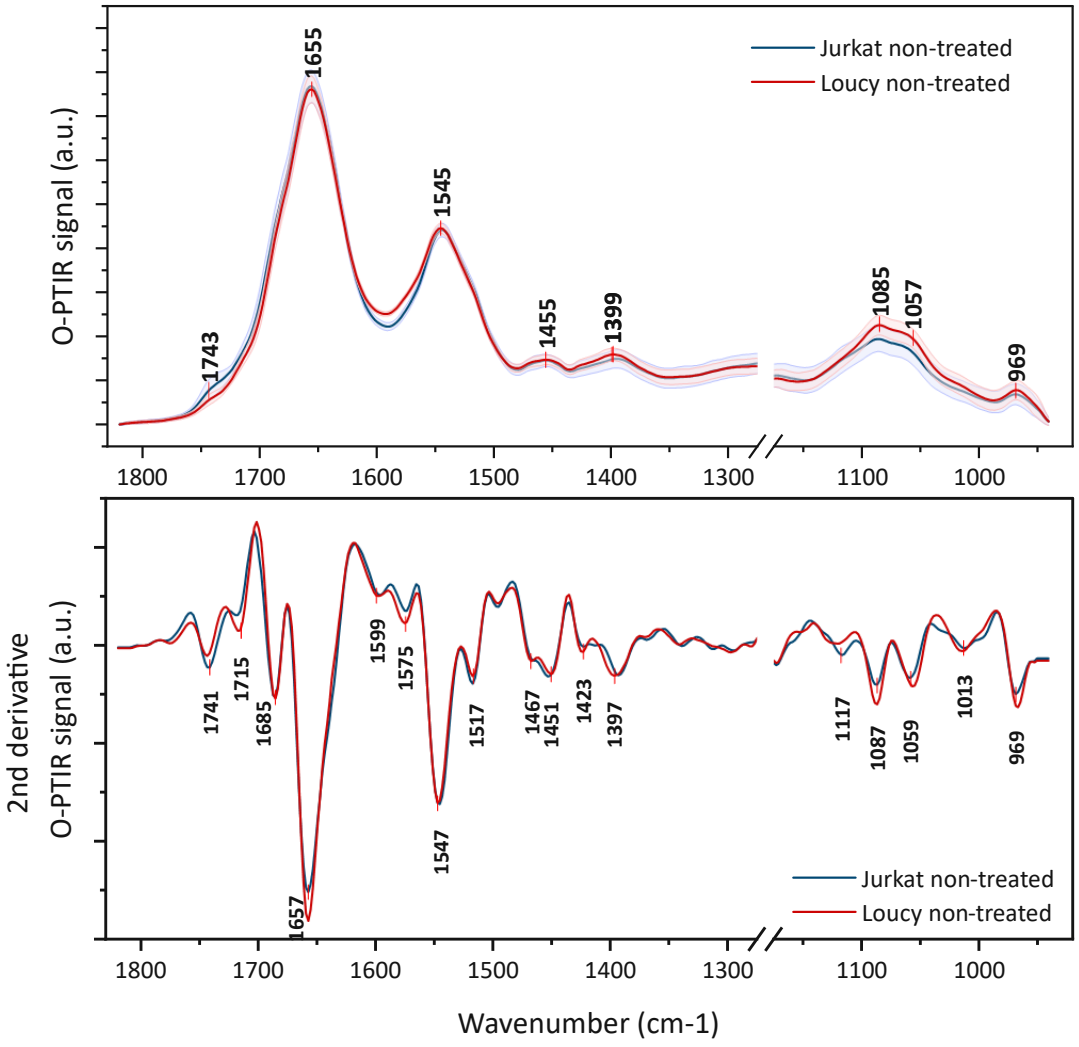

Figure 27: Comparison between non-treated Jurkat and Loucy cell line global spectra
Averaged O-PTIR spectra (15 cells, 10 locations per cell, 4 spectra repetions), as well as their 2nd derivative for non-treated Loucy and Jurkat cells are presented. Except from a higher band intensity of Jurkat for 1743 cm-1 few differences are noticeable.

5.1.2 IR Response of Cancer Cell Line Loucy Exposed to Ferroptosis Inducer

The model cell line Loucy was used as the general control T-ALL cancer cell as it did not exhibit a mutation for NOTCH1.

The mean IR response for non-treated Loucy cells did not indicate significant differences for RSL3 and APR-246 ferroptosis-induced cells. Figure 28 (a) presents the mean spectra of negative control, APR-246 and RSL3-treated Loucy cells. APR-246 treated Loucy cells are deviating from the other two in exhibiting a band shoulder at 1627 cm^{-1} assignable to protein β-sheets. The maximum of the lipidic CH_3 bending vibration slightly shifts from 1397 cm^{-1} (non-treated) to 1392 cm^{-1} (ferroptosis-induced). Differences of the symmetric PO_2^- stretching band (1085 cm^{-1}, shoulder 1060 cm^{-1}) such as band shapes, maxima intensities and shifts of the individual cell treatments are noticeable, but difficult to

allocate, as these can also originate from remaining PBS residues. When apoptosis occurs, the amide I band appears larger with a shoulder around 1620 cm^{-1}. So, the shoulder at 1627 cm^{-1} can also be an indication of a non-specific cell death.

If the concentration of peroxidised lipids increases, a more pronounced band is expected at 1740 cm^{-1} (C=O stretching vibration). In the 2nd derivative, peaks are recognisable at 1743 cm^{-1} and weakly 1715 cm^{-1} for all conditions. The maxima of all conditions are within the respective deviation range of each other, which means no definite conclusions can be drawn.

It was therefore decided to perform k-means analysis to evidence fine differences. K-means clustering was carried out using the 2nd derivatives of the O-PTIR spectra in the range of 1800 – 1300 cm^{-1}. The range below 1300 cm^{-1} was excluded due to laser instabilities (1260-1180 cm^{-1}) and the ambiguous assignment of the phosphate band proportions, due to the use of PBS during sample preparation.

Just by separating cluster of the 2nd derivative, as shown in Figure 28 (b), one can again recognize that APR-246 is deviating from non-treated and even RSL3-incubated Loucy cells, being the only one belonging to cluster 3 (13.3%). Cluster 2 exhibits the highest occurrence in all three samples and its proportion decreased in the ferroptosis induced samples (APR-246: 68.7%, RSL3: 75.3%) in contrast to non-treated Loucy cells (98%). The proportion of component 1 increased from 2% (non-treated) to 18% (APR-246) and 24.7% (RSL3).

The spectrum of cluster 3 demonstrates the largest divergence those of cluster 1 and 2 (Figure 28 c). Its 2nd derivative (Figure 28 d) features a clearly pronounced β-sheets (aggregation) shoulder of the amide I band (1627 cm^{-1}) and only a weakly pronounced band at 1715 cm^{-1}.

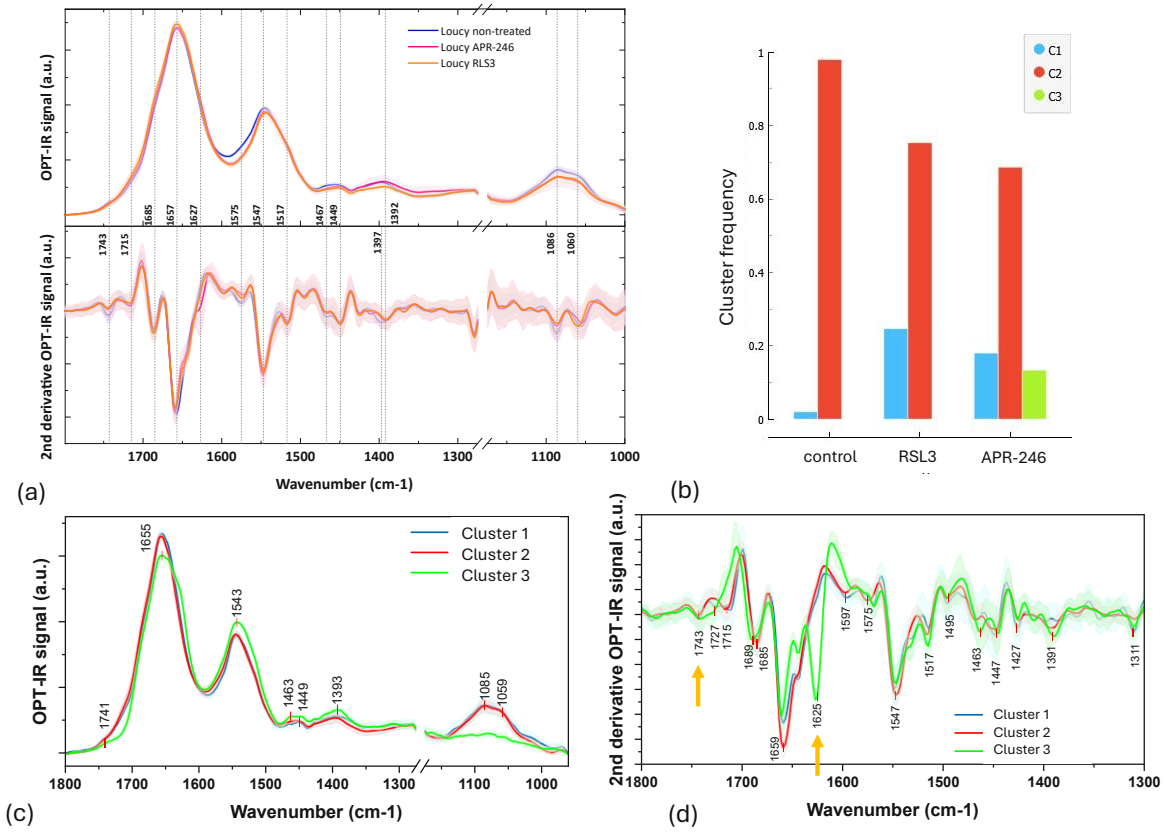

Figure 28: Cluster analysis - cell line Loucy
(a) O-PTIR spectra and their corresponding 2nd derivative from cell line Loucy in non-treated and ferroptosis-induced conditions between 1800 – 960 cm-1. (b) Histogram of the cluster distribution after k-means clustering of the ferroptosis induced and negative control Loucy cell samples. (c) O-PTIR spectrum shape of the individual cluster components. (d) 2nd derivative of the individual cluster spectra.

5.1.3 IR Response of Cancer Cell Line Jurkat Exposed to Ferroptosis Inducer

For the Jurkat model cell line, two measurements sequences were acquired. Dataset 1 included Jurkat cells treated with both ferroptosis inducers and a DMSO-treated control sample. For dataset 2 a negative control sample as well as cells treated with both ferroptosis inducers were used.

Both datasets were merged and then k-means clustering performed on them. All spectra (Figure 29 (a)) display spectra similar to the cell line Loucy. The only experimental difference between these two series is the duration between defreezing and incubation. This was three weeks for dataset 1 and one week for dataset 2. The carbonyl ester band at 1741 cm^{-1} is significantly more pronounced and the amide I band shoulder is shifted from 1685 to 1693 cm^{-1} in dataset 2 compared to dataset 1. Although the results are repeatable, the clustering procedure clearly reveals discrepancies between both data sets. This was evidenced by looking at the ratios of the RSL3-treated Jurkat cells. The cluster components distribution, in Figure 29 (b), is dataset dependent. Five clusters in total were identified. The most likely explanation for this occurrence is the different duration of defreezing and incubation

between dataset 1 (3 weeks) and dataset 2 (1 week). The conducted viability tests also indicate that Jurkat cells are difficult to maintain because of their high cell viability, thus supporting this assumption it is an even more likely reason.

Especially the spectrum and 2nd derivative (Figure 29 a and d) of cluster 4 present a distinct 1740 cm^{-1} band. This cluster shows a major proportion in the non-treated control samples (~50%) of dataset 2, which confirms a weakened state of the cells. It was therefore decided to exclude dataset 2 and concentrate on dataset 1 regarding the O-PTIR data analysis. It is difficult to draw conclusions for dataset 1 without a negative control sample and no comparison between Loucy and Jurkat is possible.

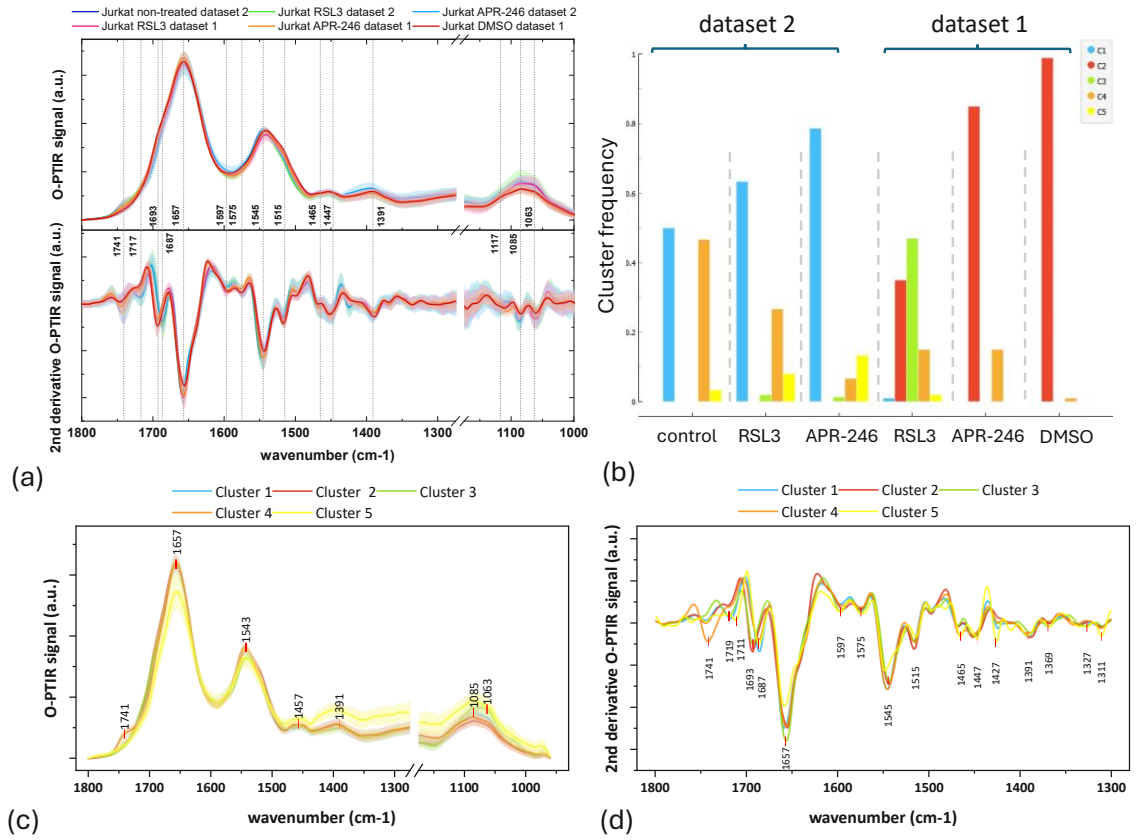

Figure 29: Cluster analysis of merged dataset from cell line Jurkat
(a) O-PTIR spectra and their corresponding 2nd derivative between 1800 – 960 cm^{-1}. (b) Histogram of the component distribution after k-means clustering of individual treated Jurkat samples. (c) O-PTIR spectrum shape of the individual cluster components. (d) 2nd derivative of the individual cluster component spectrum shapes for cell line Jurkat.

K-means clustering was repeated for dataset 1. The spectra (Figure 30 (a)) display no differentiation between RSL3, APR-246 and DMSO-treated cells. K-means clustering in Figure 30 (b) reveals an almost exclusive categorisation of DMSO-treated Jurkat cells as component 1 (97%). Cluster component 2, exhibiting the most pronounced 1741 cm^{-1} band, demonstrates a strong presence in Jurkat APR-246 (73%) together with component 1 (27%).

Component 3, displaying a prominent band at 1721 cm^{-1}, only appears for Jurkat RSL3 (52%) together with almost equal proportions of component 1 (22%) and 2 (26%).

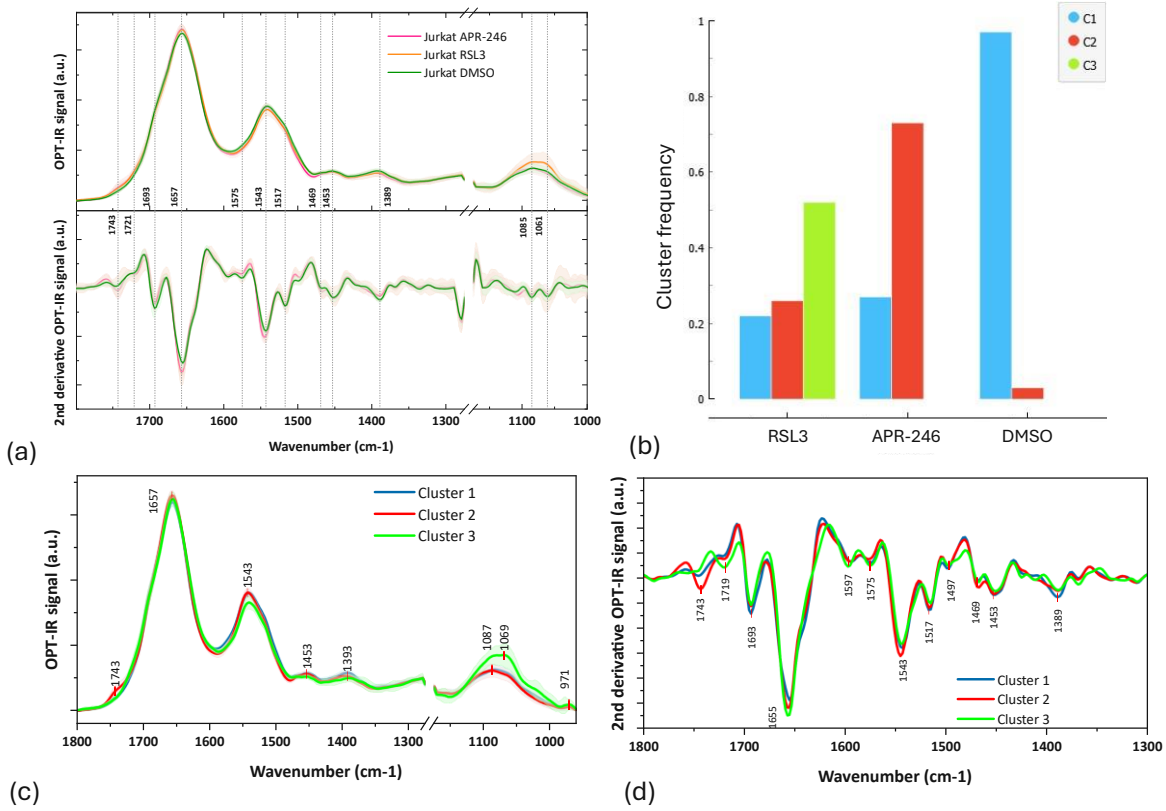

Figure 30: Cluster analysis - cell line Jurkat
(a) O-PTIR spectra and their corresponding 2nd derivative from cell line Jurkat dataset 1 between 1800 – 960 cm^{-1}. 2(b) Histogram of the component distribution after k-means clustering of the ferroptosis induced and DMSO control Jurkat cell samples. (c) O-PTIR spectrum shape of the individual cluster components. (d) 2nd derivative of the individual cluster component spectrum shapes.

5.1.4 Discussion - Global Analysis

The O-PTIR technique provided uniform IR spectra when measuring multiple, entire cells of the same condition. These were regarded as a representative mean spectrum for the individual cell type conditions. This makes it very efficient for global analysis of the individual cell conditions

The cell line Loucy provided more robust O-PTIR spectra than Jurkat, possibly due to its lower cell viability. For Loucy cells, the clustering procedure allows to discriminate APR-246 treated cells from RSL3 treated cells and negative control cells. This is to be expected as Loucy is less sensitive to ferroptosis inducers and APR-246 can also cause non-specific cell deaths. These data provide a global IR response tendency. No clear lipid peroxidation or its locations are visible. However, the measurement data from the O-PTIR analysis could be used to conclude the general quality of the applied cell line.

For Jurkat a higher lipid peroxidation should be observed. A precise statement on this cannot be made, as the cell culture quality was not as good as expected. Although the two Jurkat datasets are not comparable due to the different time frames between defreezing and incubation, it gives an indication of the global response of the cells regarding the sample treatment and fixation protocol. Since the Jurkat negative control sample was not in suitable conditions, no comparisons between the model cell lines Loucy and Jurkat are possible. A complete set of both model cell lines has to be studied several times, to obtain a quantitative statement regarding the effects of the artificial ferroptosis-induction.

In order to reach this objective, the culture time for the apparently fragile Jurkat line must be improved. To ensure reproducibility of the measurement, the sample treatment has to be reviewed again. Particular attention must be paid to optimise the point of exposure to the ferroptosis inducer after cell maintenance.

No distinctive global trend can be recognized for both individual cell lines at this point, but there is still the necessity for a method with a higher spatial resolution to analyse local nanometric lipid peroxidation.

5.2 Nanoscale investigation of lipid peroxidation

Using the optimised and validated protocol for AFM-IR analysis, multiple non-treated and ferroptosis-induced cells of both cell lines were examined. The initiated effects on the plasma membranes by different inducers were investigated. Although an impairment of the cell culture Jurkat was observed, the cells are informative enough to test the capability of the established sample preparation protocol and the analysis system.

5.2.1 Validation of the AFM-IR Procedure for Cell Measurements

5.2.1.1 Model Cell Line Loucy

Loucy is considered to react less sensitive to ferroptosis.

The topographies of three cells in Figure 31 highlight typical cell appearances of nontreated and treated cells: Those cells exhibit clearly demarcated, partially enlarged nuclei, a shrunken cytoplasm with pseudopodia (protrusions of eukaryotic cells, typical for leukocytes) on the peripheral cell border.[81] The filament-like protrusions are hallmarks of cell migration, cancer invasion and metastasis.[82]

IR maps were acquired at 1657 cm^{-1} (amide I) representative for the total protein content and at 1740 cm^{-1} representative for esterified and peroxidized lipids (C=O stretching vibration). This was done

at two laser repetition frequencies: at 200 kHz to probe the entire cell and at 1565 kHz to explore the top-most surface layer, mainly the membrane.

The IR maps ratios between 1740 and 1657 cm^{-1} were calculated at low and high pulse frequencies (Figure 31 middle and right column). The ratio at 200 kHz for non-treated cells is around 0.1 and is homogeneously distributed. For APR-246 the ratio is up to two times higher and also homogeneously distributed in the centre. Higher values appear on the border. This could indicate a further effect of APR-246 in the inner cytoplasmic region. For RSL3, the ratio is around 0.1 on the nucleus but higher in its surroundings. At pulse frequencies of 1565 kHz, the untreated Loucy cells exhibited large areas with values between 0 - 0.1, but small individual hotspots with ratios of up to 0.4 were recognisable. APR-246 treated cells display a significantly greater incidence of ratios 0.2 and higher, but individual sections with ratios below 0.05 are also evident. The RSL3-treated Loucy cells had a typical cell shape (~7 µm diameter, up to 650 nm height), which made it difficult to create large-area IR maps. The ratios which could be determined for these cells are exclusively above 0.2.

Peroxidised phospholipids are expected to accumulate on the cell membrane on the surface. Therefore, the acquired IR ratios at higher pulse frequency, having less probing depth, are of particular interest.

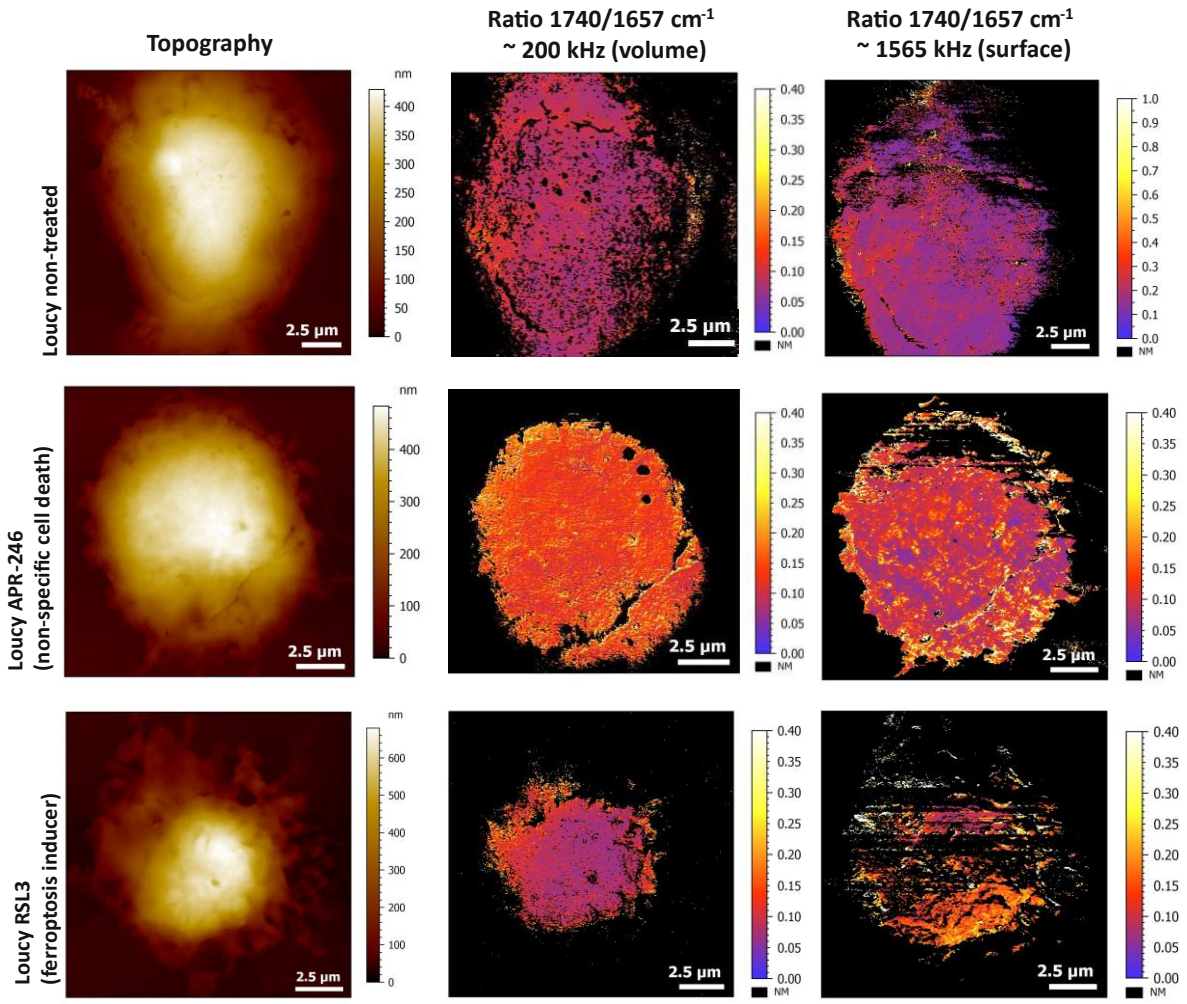

Figure 31: IR map ratios of non-treated, RSL3/APR-246 incubated Loucy cells
Topography images and IR map ratios (1740/1657 cm^{-1}) for the cell line Loucy in the conditions non-treated, APR-246-treated and with inducer RSL3 at lower pulse frequency (middle column) and high frequencies (right column) are displayed. While the IR map ratios at low pulse rates mostly appear intact, those at high pulse rates have missing sections.

To look at local phospholipid peroxidation, a series of local spectra at high pulse rates was acquired.

In contrast to the previous O-PTIR mean spectra, the average spectra at high pulse frequency (Figure 32), demonstrate different band shapes for the individual conditions. Particular the spectrum of the negative control sample differs from the ferroptosis-induced Loucy cells. There, a more distinct CH_2 scissoring band at 1462 cm^{-1}, accompanied by a fluctuation (1642 and 1636 cm^{-1}) of amide I band is observed. Differences in the range 1700-1750 cm^{-1} of the spectra can be recognised but cannot be precisely specified.

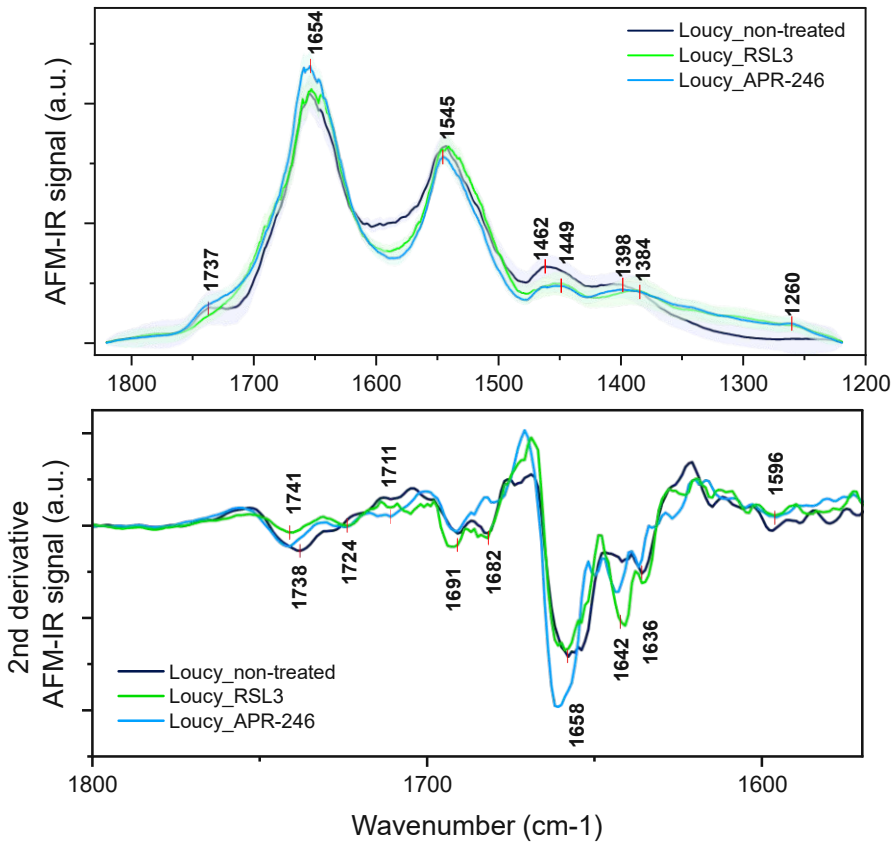

Figure 32: Averaged spectra of individual Loucy conditions
Comparison of averaged AFM-IR spectra as well as their 2nd derivative for Loucy non-treated cells as well as cells incubated with RSL3 and APR-246 for a pulse frequency of 1565 kHz, 100 ns pulse width and 3.4% laser power. At least 100 spectra at varying cell locations were averaged. .

Averaging of the spectra leads to an unintentional loss of essential information, especially regarding the 1740 cm^{-1} band. Since miniscule hotspots with accumulated phospholipids are all over the surface, a localisation of only these areas is lost in the mean spectra.

It is therefore more advantageous to look at spectra at specific locations identified on the IR maps. As highlighted in Figure 33, individual spectra at location of varying ratio intensity of 1740/1657 cm^{-1} were acquired. The locations were selected at positions with high (orange), intermediate (light blue) and low (dark blue) ratio values.

Significant differences in the C=O stretching band at 1737 cm^{-1} can already be observed for the negative control cell. These can originate from the cancer cell itself due to oxidative stress, a reduced cell quality or indicate remaining effects from sample preparation (DMSO). The band at 1463 cm^{-1} (CH_2 scissoring vibration, lipids) rises. Local pinpointing on an APR-246 treated cell emphasises, besides the increased 1740 cm^{-1} band at higher IR map ratios, an enhancement of the amide I/II ratio. While for negative control Loucy cells the band 1465 cm^{-1} decreases for local spectra on positions displaying lower IR map ratios, the bands 1451 cm^{-1} and 1393 cm^{-1} increase for APR-246 incubated ones.

Acquisitions of the phosphate bands below 1200 cm^{-1} and other possible peroxide bands in this range were unfortunately not possible.

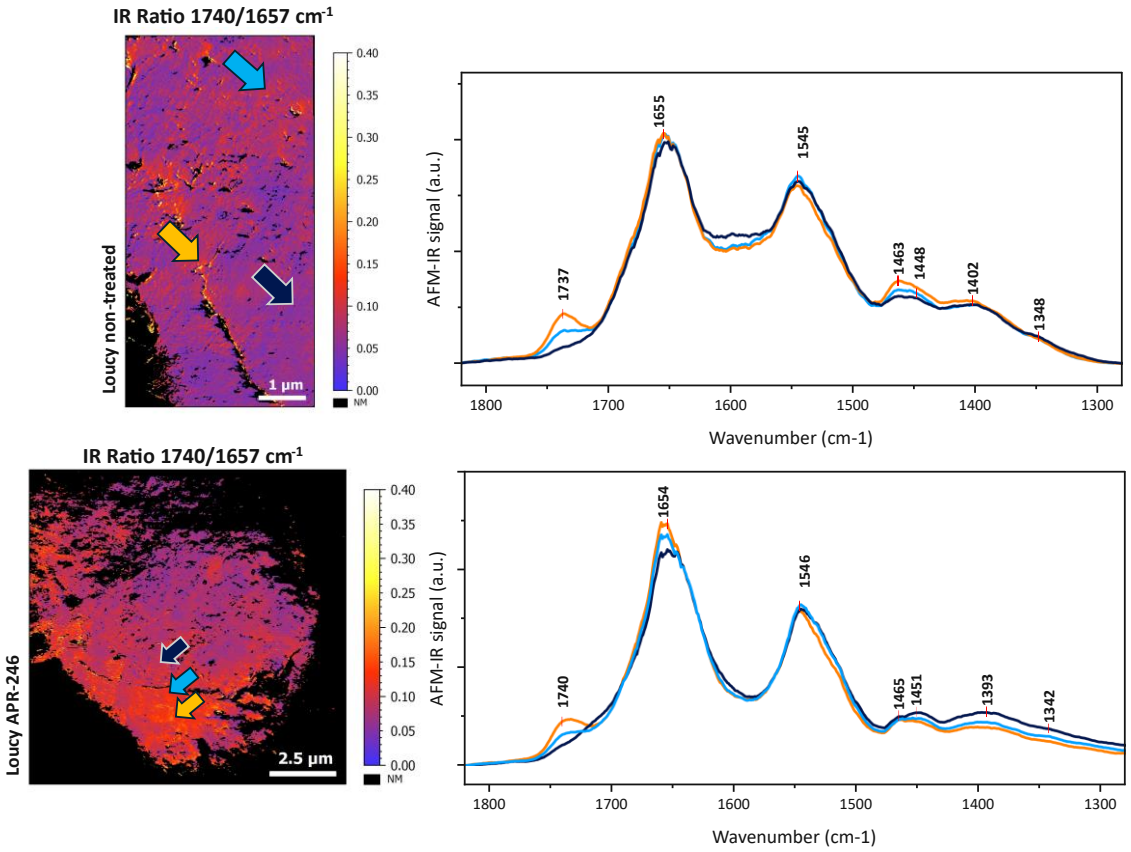

Figure 33: Local spectra on Loucy non-treated and Loucy APR-246
Comparison of local spectra on a non-treated Loucy cell to an APR-246 incubated Loucy cell. The locations were selected at positions with high, intermediate and low ratio values, based on IR map ratios 1740/1657 cm^{-1}. Spectra were acquired around 1565 kHz, 100 ns pulse width and 3.4% laser power.

5.2.1.2 Model Cell Line Jurkat

Jurkat is considered to react more sensitive to ferroptosis inducers due to its NOTCH1 mutation.

AFM-IR analysis confirmed the low quality of dataset number two. The topographies of non-treated and APR-246 ferroptosis-induced Jurkat cells in Figure 34 already display impaired cell structures. No clearly defined nucleus can be recognised, and the cell remains appear flat. The cell membrane has noticeable perforations and is spread over a large area. A further indication for an irregularity with this data set can be recognised from the IR maps at higher pulse rates:

The IR map ratio of 1740/1657 cm^{-1} for non-treated cells at 1565 kHz on the remaining nucleus is around 0.07. However, in areas of membrane impairment, the ratio increases up to 0.2. For APR-246 the band is ratio homogeneously distributed and with values mostly under 0.05. Single 'lines' with ratio values up to 0.3 are visible but expected to be electronic noise. For RSL3, the ratio on the

nucleus is around 0.12, but has clearly distributed and highly localised hotspots with ratios up to 0.3 in the peripheral cell space. The located lipid peroxide accumulations are about 100 nm in diameter. Encapsulated structures in the pseudopodia area with concise 1740/1657 cm^{-1} ratios are also recognisable (marked by arrow).

It was widely assumed that DMSO has a low cell toxicity when used in concentration below 10%.[83] Recent *in vitro* studies on model cell lines and synthetic membranes have proven an influence of DMSO on plasma membranes, proteins and even nucleic acids down to 0.1% DMSO concentration.[84,85] This could mean that all cells were influenced by DMSO, which could also explain the impaired response of negative control Jurkat cells (see topography as well as IR Map ratio at 1565 kHz in Figure 34: IR map ratios of non-treated, RSL3/APR-246 incubated Jurkat cellsFigure 34).

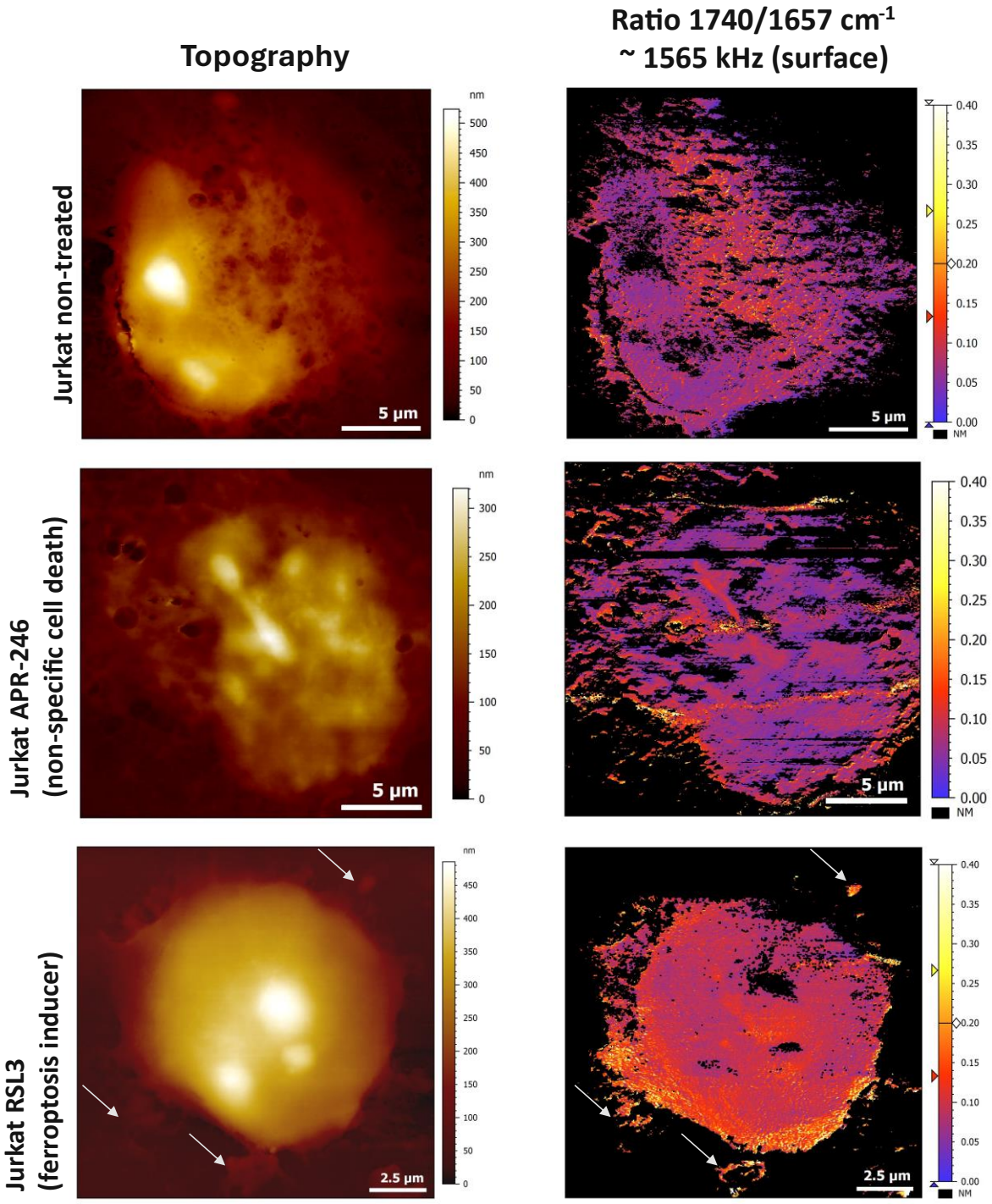

Figure 34: IR map ratios of non-treated, RSL3/APR-246 incubated Jurkat cells
Topography images and IR ratios 1740/1657 cm^{-1} for the cell line Jurkat in the conditions non-treated, APR-246-treated and with inducer RSL3 at pulse frequencies around 1565 kHz and 100 ns pulse width. Laser power varied between 3.4 and 9.7%.

Local spectra of the negative control sample in Figure 35 reveal an atypically high occurrence of the C=O stretching band at 1740 cm^{-1} as indicated by the IR map ratios at 1565 kHz. The band intensity is comparable to that of local hotspots of RSL3-treated Jurkat cells. This could indicate a problem that occurred during the cell preparation.

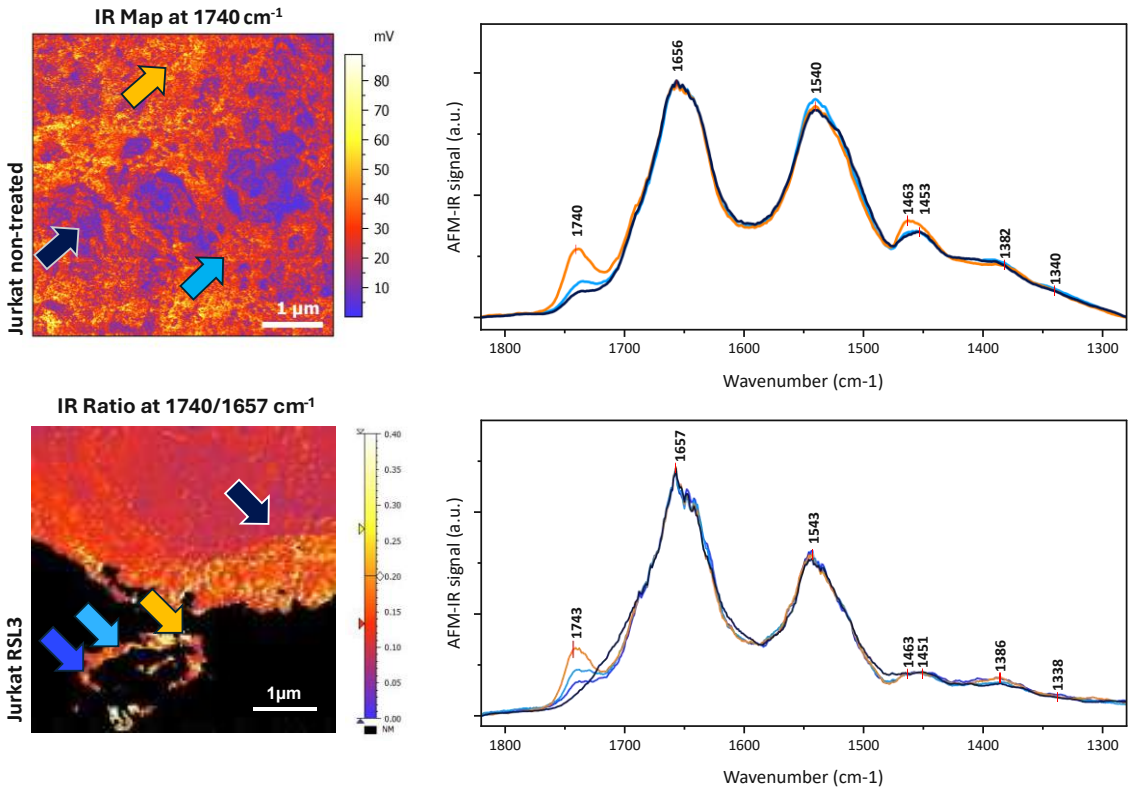

Figure 35: Local spectra on Jurkat non-treated and Jurkat RSL3
Comparison of local spectra on a non-treated control as well as a RSL3-ferroptosis induced Jurkat cell at locations with high, intermediate and low amplitude signal on the main cell as well as pseudopodia area based on an IR map (ratio) for the C=O stretching band (1740 cm^{-1}). Local spectra were acquired around 1565 kHz, 100 ns pulse width and 3.4% laser power.

5.2.1.3 Summary – nanoIR2 Characterisation

With those results we have demonstrated the potential of the AFM-IR technique. The detectability of lipid peroxidation using the developed method can be demonstrated.

A trend of the results in agreement with the expectations can be observed. Less phospholipid peroxidation for Loucy while higher responses for Jurkat cells can be noted, especially for ferroptosis inducer RSL3 and to a less extent also for APR-246. So far, these results represent trends and need to be confirmed with repeated experiments, to gain statistically more significant results.

The optimised protocol confirms that it is possible to investigate changes at the subcellular level via IR maps as well as local IR spectra. However, more stable instruments are required, especially in the IR map recording of the entire cell: The contact between cantilever tip and surface can be lost or the contact frequency is shifting so much that PLL-tracking was no longer possible. The shifts of the resonance frequency during the analysis can be caused by varying mechanical properties of the sample material.[70] These occurred more frequently for the cell type Loucy as well as for IR maps acquired at 1740 cm^{-1}. This may be related to the fact that the protocol was developed with Jurkat and optimised for its mechanical surface properties and responses coupled to mid-IR radiation. When

mapping cells of the cell line Loucy, a more adhesive behaviour of the sample surface on the cantilever was observed.

But the main issue is the permanent thermal drift observed during the acquisitions of maps. It is crucial to not to underestimate this especially when trying to locate nanosized peroxidation hotspots. The sample in the AFM moves even though being fixed to a substrate and the microscope, due to thermal expansion due to ambient temperature changes. This can lead to movements up to hundreds of nm per minute. During the recording of extensive spectra arrays, despite recurring mappings after certain numbers of repetitions, it leads to uncertain spectra positioning. This can significantly distort the results. More AFM-stable systems like ICON-IR have minor restrictions in this context and were used in a second approach to solve this problem.

5.2.2 Detailed Analysis of the Membrane Impairment

Analysis using the ICON-IR were included to finely probe the impairment of the membrane generated by the peroxidation. For the ICON-IR analysis, only one cell condition (Jurkat RSL3) was chosen based on its expected higher impact on cell membranes leading to lipid peroxidation.

The first step was performing IR maps at 1740 and 1657 cm^{-1} of cell clusters and then progressively zooming in to regions of interests on the cell as displayed in Figure 36. At large scale, the 1740 cm^{-1} map seems to exhibit a homogeneous signal except for some specific positions circled in white on Figure 36.

Focusing on just one section of a cell (Figure 36 centre column) the cell membrane contains a crack and several trough-shaped indentations on the main cell part as well as a smaller round nodule and a capsule-shaped external cell structure (vesicle). The vesicle exhibits a strong uniform signal intensity, while the tangled nodule structure and the main cell part next to it contain several hotspots of the 1740 cm^{-1} band. Signal distribution on the main cell reveals individual, very intense hotspots, but also large areas of slightly increased intensity.

A zoom confirms the presence of intense hotspots (high absorbance at 1740 cm^{-1}) without any significant topographical changes on the membrane. The hotspots are approximately 100-150 nm in diameter.

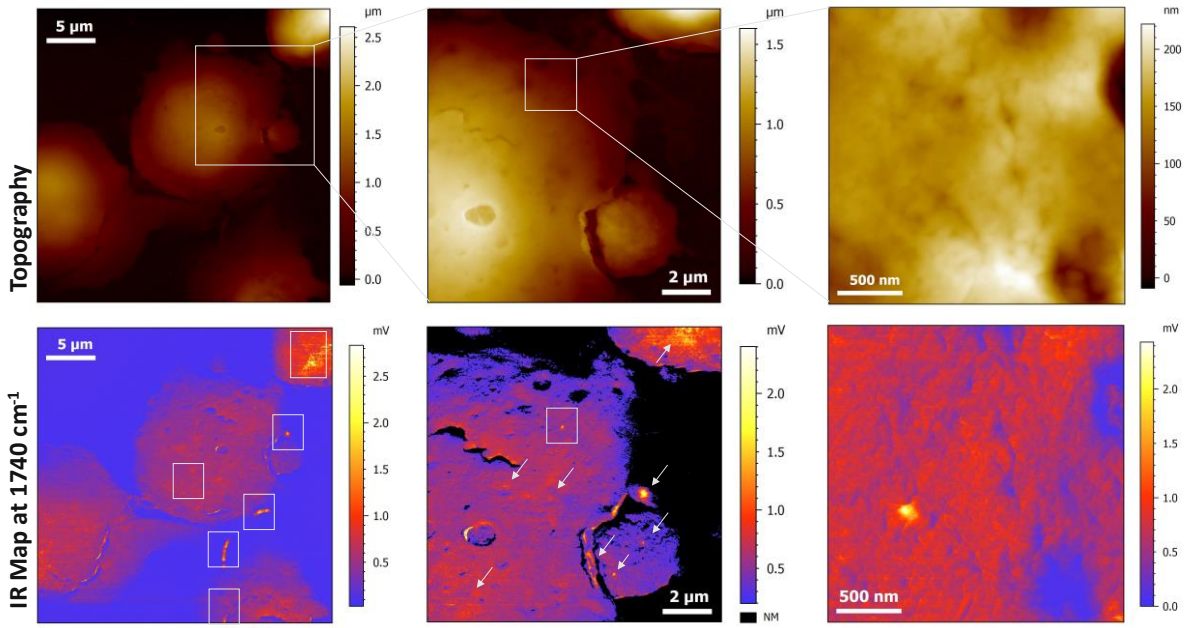

Figure 36: Topography and IR response of Jurkat RSL3 cells via ICON-IR acquisition
Accumulations of Jurkat RSL3 cells with increasing magnification of a specific cell section. The top row displays the topography, while the bottom row indicates the corresponding IR maps at 1740 cm^{-1}.

The maps displaying the ratio 1740/1657 cm^{-1} (see Figure 37) clearly illustrated the presence of those hotspots, spread all over the cell. In particular vesicles around the cell displaying strongly increased ratios (see arrows) can be observed. On the main cell part, particularly increased ratio domains are visible around the areas that already show membrane damage, which again indicates that stronger lipid peroxidation might be associated with membrane impairment.

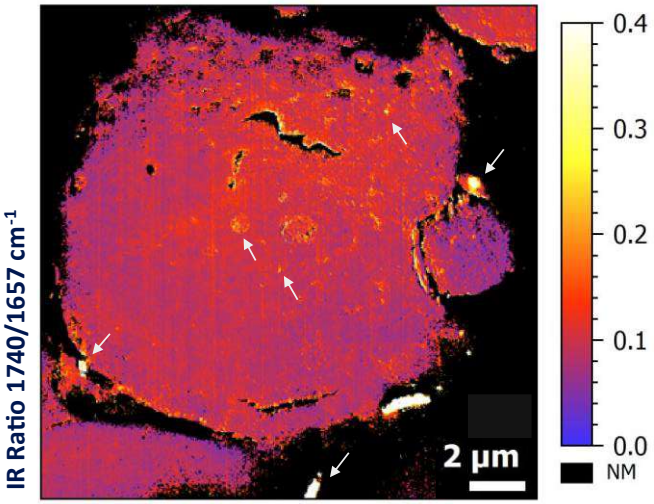

Figure 37: IR map ratio – ICON-IR Jurkat RSL3
Ratio of IR maps between characteristic ester band (1740 cm^{-1}) and total protein content (1657 cm^{-1}) of an Jurkat RSL3 type cell. Images were acquired using 1.8% laser power, 100 ns pulse width and 1255 kHz pulse frequency.

A line (spacing 20 nm) was recorded over the hotspot to analyse the changes in the individual bands. These are plotted in Figure 38 (b). When reaching the centre of the hotspot, the absorbance at 1738 cm^{-1} increases simultaneously with the absorption at 1248 cm^{-1}. The 1248 cm^{-1} band is corresponding to antisymmetric PO^{2-} stretching of phospholipids but also C-O stretching vibrations of lipid hydroperoxides. Furthermore, a strong variance in the shape of the symmetric PO_2^- stretching band (1085 cm^{-1} showing a band shoulder at 1047 cm^{-1}) can be observed. This band can be influenced by possible PBS residues and does not proportionally follow the course of the 1740 cm^{-1} band. Besides 1248 and 1085 cm^{-1}, two more bands appear at 1185 cm^{-1} and 1132 cm^{-1} when going through the hotspot. The 1185 cm^{-1} band could indicate, among others, C-O stretching of peroxyacids, while the 1132 cm^{-1} band can be associated with C-O stretching vibrations of alkyl peroxides. An amide I band broadening could also indicate lipid peroxidation but is not apparent in this case.

A superposition of the local spectra at the intensity hotspot of the IR map at 1740 cm-^{1} (Figure 38 (c)) displays an increase of the bands 1248, 1183 and 1132 cm^{-1} proportionally with 1738 cm^{-1}.

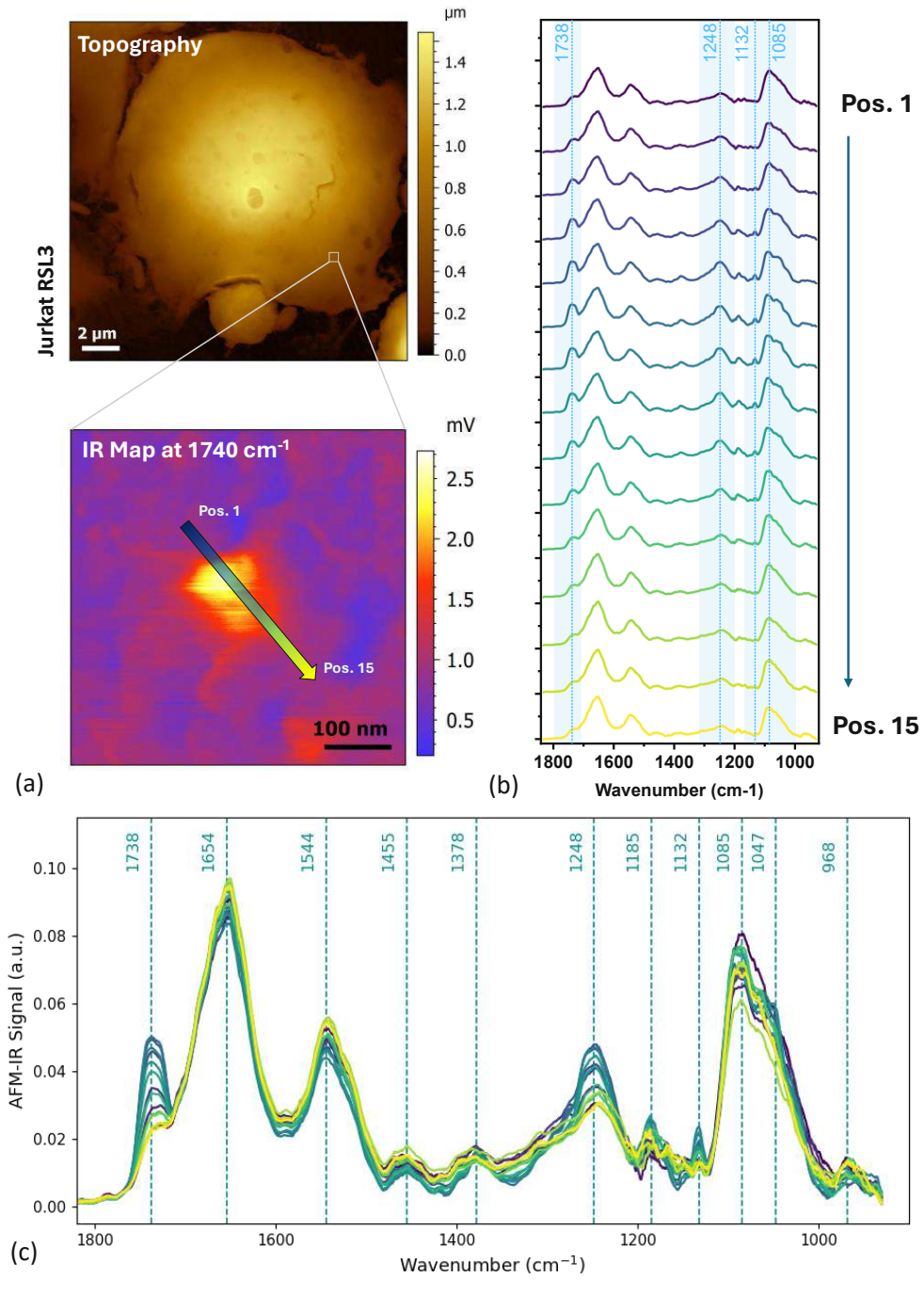

Figure 38: Characterisation of a phospholipid hotspot on Jurkat RSL3

(a) *Topography of a Jurkat RSL3 cell with a magnified section of an IR map at 1740 cm^{-1} showing the course of an array of local spectra. Images were acquired using 1.8% laser power, 100 ns pulse width and 1255 kHz pulse frequency. (b) Plot of the individual spectra with highlights of specific bands. The spacing between the spectra was 20 nm. (c) Markings of all band maxima of the forementioned spectra.*

The 2nd derivatives of the local spectra (Figure 39 A) highlight the complex structure of the 1740 cm^{-1} absorbance band with several maxima at 1747, 1738, 1732 and 1724 cm^{-1}. While the appearance of 1738 and 1730 cm^{-1} bands is expected, maxima at 1747 and 1724 cm^{-1} have not been on the membrane.

The amide I band centred at 1650 cm^{-1} shows less divergence with several band shoulders at 1686, 1666 and 1636 cm^{-1}. Between amide I and II (Figure 39 B) three bands are visible at 1611, 1589 and 1572 cm^{-1}. These might be assigned to antisymmetric carboxylate stretching vibrations lipidic structures.[45,50]

Different intensities depending on the spectral location are noticeable for antisymmetric and symmetric PO^{2-} stretching bands at 1248 cm^{-1} and 1086 cm^{-1} as well as the band shoulder at 1048 cm^{-1} (see Figure 39 D). Natural occurring phospholipids can absorb at 1740 cm^{-1}, 1724-1729 cm^{-1} and 1082 cm^{-1}.[49,52] To distinguish peroxidised lipids from natural phospholipids a comparison of the 1740/1082 cm^{-1} ratios between ferroptosis-induced cells to control cells is necessary. This was not possible due to the compromised control samples in this study (Figure 39).

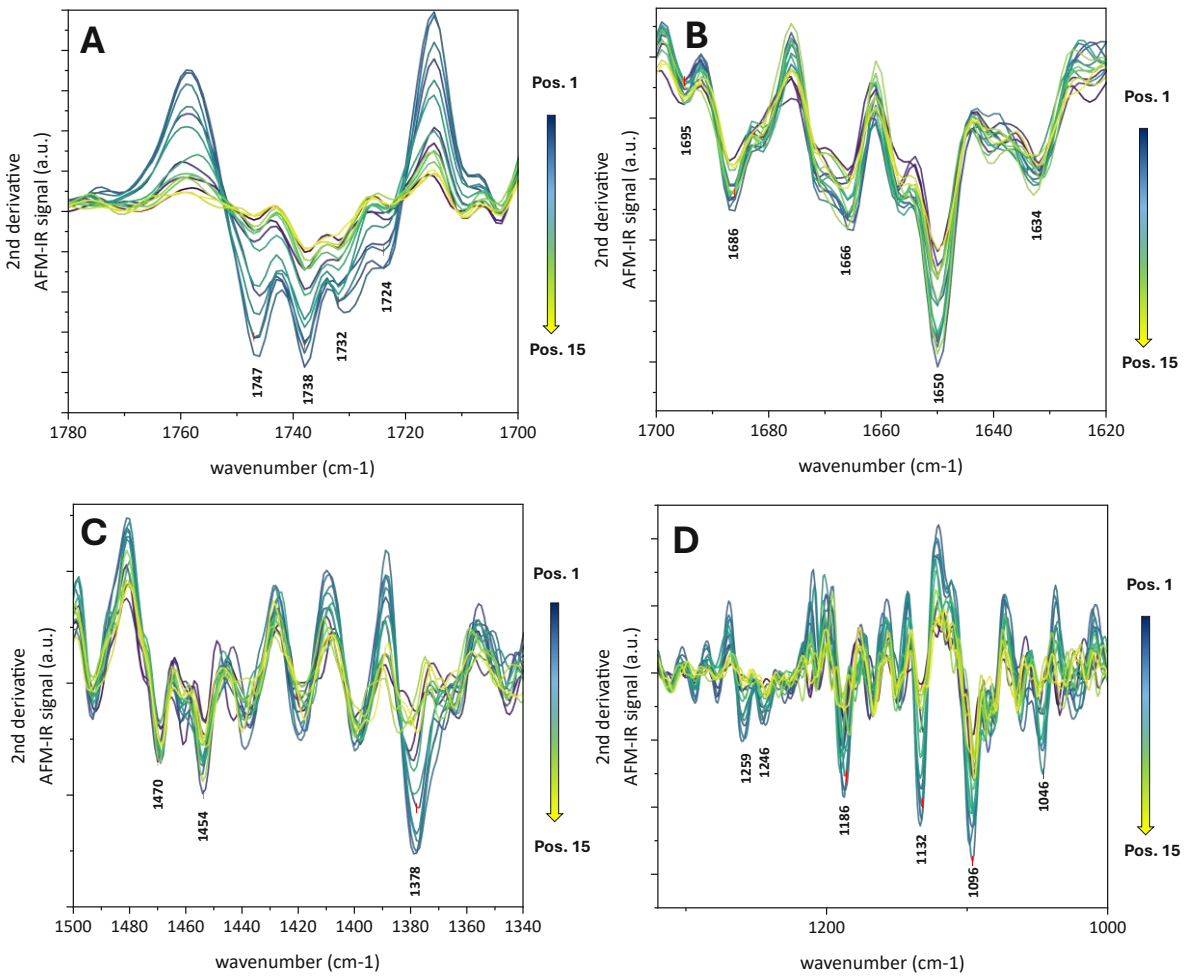

Figure 39: Investigation of the Jurkat RSL3 hotspot via its 2nd derivatives progression
A-D: *The progression of the 2nd derivatives of the spectra in Figure 38 for the carbonyl ester band region (1780-1700 cm-1), the amide I band, as well as CH_3/CH_2 and phosphate bands.*

By plotting the five most significantly changing bands based on Figure 38 (c), against amide I, differences in the magnitude of various band ratios calculated from 1738, 1248, 1180 and 1130 cm^{-1} at different measurement positions including the hotspot and its surrounding area can be observed (Figure 40 (a)). The progression of ratio 1085/amide I is not as distinctive. Interestingly also the ratio between the CH_3 (1378 cm^{-1}) and CH_2 (1455 cm^{-1}) assigned bands (Figure 40 (b)) changes proportional to the 1740/amide I ratio. This ratio provides information about the aliphatic chain length. This ratio increase on the hotspot could indicate a shortening of the lipid chains during phospholipid peroxidation. Additional lipidomic analysis could be a complementary method for further analysis.

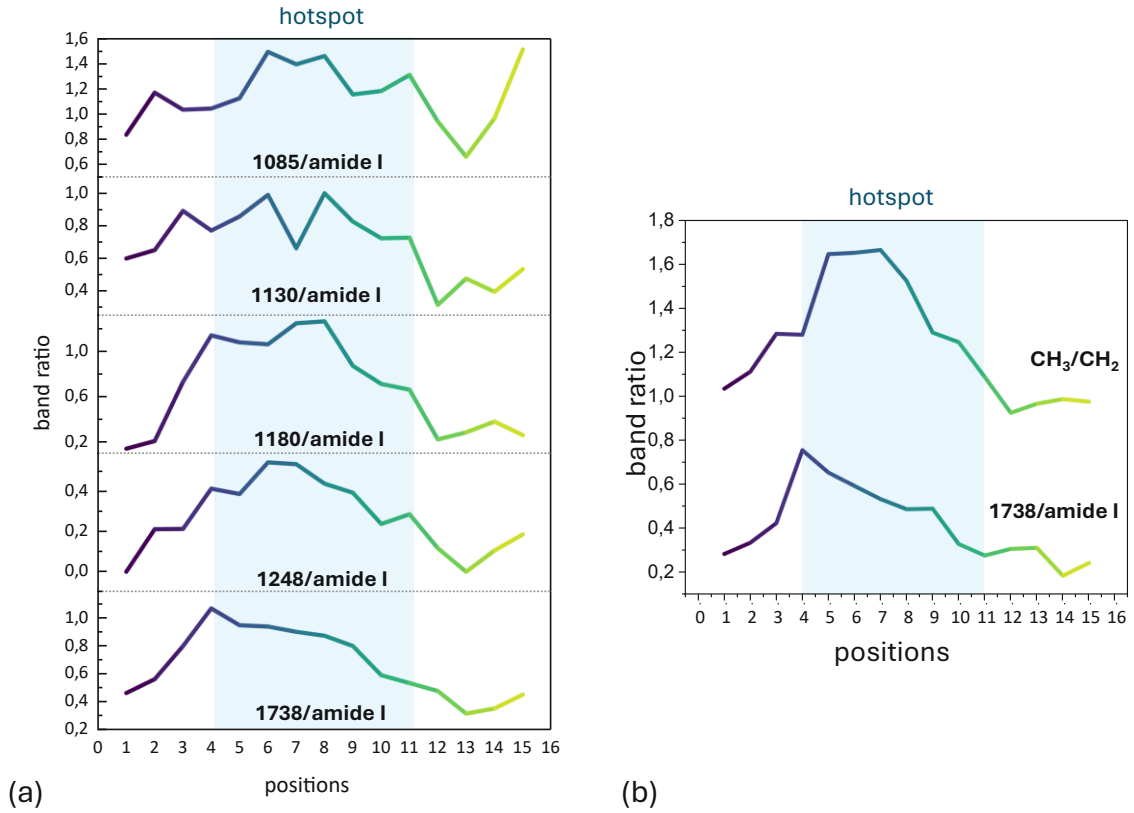

Figure 40: Band ratio over lipid peroxidation hotspot - Jurkat RSL3
(a) *Band ratios between distinctly changing bands over the hotspot referred to the corresponding amide I band. For the bands 1738, 1248, 1185 and 1130 cm^{-1} a ratio increase on the hotspot area is noticeable (marked in blue). That observation is not distinctive for the ratios 1085/amide I. (b) The ratio between CH_3/CH_2 (1378/1455 cm^{-1}) as well as 1740/amide exhibits proportionally increasing ratio values for the line array.*

Those analysis confirm the importance of using a more stable AFM: A notably lower thermal drift less than 1 nm/min was measured, 10 times better than the other system. That allows a more precise targeting and tip positioning for local spectra which is advantageous for analysing nanosized phospholipid hotspots.

Using the second system (ICON-IR) it was possible to identify peroxidised and oxidised species at 1740 cm^{-1}, 1250 cm^{-1}, 1170 cm^{-1} and 1133 cm^{-1} likely connected to lipid peroxidation. Another advantage was the use of the complete spectral range from 1900 – 900 cm^{-1}. This is essential for visualising the progression of the phosphate bands in this range. It is also essential as several bands linked to lipid peroxidation can be detected in this spectral area.

Moreover, compared to the nanoIR2 system a more accurate band separation was achieved in larger spectral range which allowed the analysis of trends in absorption strength between more bands.

On the other hand, problems regarding contact loss or mechanical instabilities remain.

Still no biological conclusions can be proposed. However, this second system provided a more advanced setup as an additional tool to study the accumulation of phospholipids on cell membranes. In order to use it in a more targeted approach, the robustness and repeatability of the protocol needs to be improved, particularly with regard to the cell treatments. As a further factor, the statistical relevance must be elevated by a higher number of analysed cells per cell series and condition as well as multiple and repeat measurements.

5.2.3 AFM-IR Analysis of Extracellular Vesicles

Multiple extracellular vehicles (EVs) exhibiting prominent C=O stretching bands at 1742 cm^{-1} were also observed around several cells from different treatments (Jurkat as well as Loucy).

EVs are membrane-enclosed, nano-sized vesicles released by cells into the extracellular space and are generally accepted as intercellular communication mediators between cells. They can be categorized in microvesicles, exosomes and apoptotic bodies and vary in their biogenesis, release pathways, size, content and function.[86] Especially tumor-derived EVs play an important role in transferring intercellular biological information between individual cells regarding cancer development and progression via transporting different oncoproteins, oncogenes or chemokine (small signal proteins) receptors.[85] It would be therefore interesting, to determine the transported load of EVs after ferroptosis-induced lipid peroxidation.

The first EVs were found while performing AFM scans during the optimisation process of the sample preparation. Then, they were also observed for Jurkat cells exposed to DMSO (EVs marked on the topography in Figure 41) or RSL3 as well as Loucy cells treated with APR-246. They had an average length of 1.9±0.4 µm and a width of 1.0±0.3 µm. The height of the EVs was between 60 – 100 nm. None could be found for ‘non-treated’ Loucy and Jurkat cells.

Multiple EVs were localised around single cells. As displayed in Figure 41 one cell from Jurkat DMSO is surrounded by several EVs, with differences in their corresponding signal for the C=O stretching band (1740 cm^{-1}) and the amide I band (1657 cm^{-1}). Two EVs (ROI 1) displayed a higher absorption at 1657 cm^{-1} (see Figure 41, IR Map 1657 cm^{-1}) while the three others displayed a higher occurrence of lipids with characteristic esterified or peroxidized lipids (ROI 2, IR map 1740 cm^{-1}, Figure 41 centre column). This could either mean they are transporters for different molecule classes or belong to different EV categories.

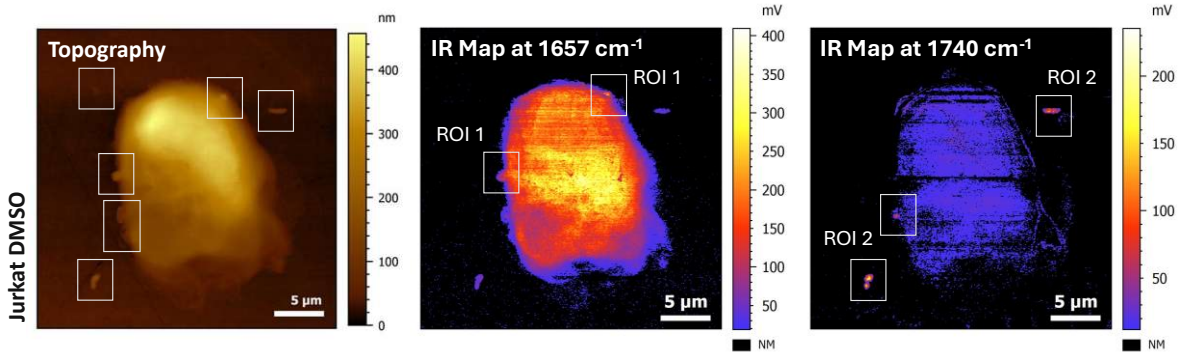

Figure 41: Localisation of extracellular vesicles around Jurkat DMSO via topography and IR maps
The topography of a DMSO treated Jurkat cell and its corresponding IR maps at 1657 cm^{-1} and 1740 cm^{1} are presented. Some EVs display a higher response at 1657 cm^{-1} (ROI 1) while other display a higher absorption at 1740 cm^{-1} (ROI 2).

But not only intervesicle divergences are observed, also intravesicle differences. One specific extracellular vesicle on the left cell border earlier associated with ROI 2 (Figure 42 (a)) reveals clearly separated internal structures when mapping at 1740 and 1657 cm^{-1} (Figure 42 (b)). In both IR maps, a circular structure (diameter ~450 nm) with an intense amide I signal as well as a pronounced 1740 cm^{-1} signal are recognisable in the centre of the EV. Further smaller circular signals with diameters between 50-100 nm of ester or amide I signal hotspots can be identified. In contrast to before, those are not colocalized. The ratio of the two mappings (1740/1657 cm^{-1}) again demonstrates the highest ratio values for the circular structure and two smaller formations above it.

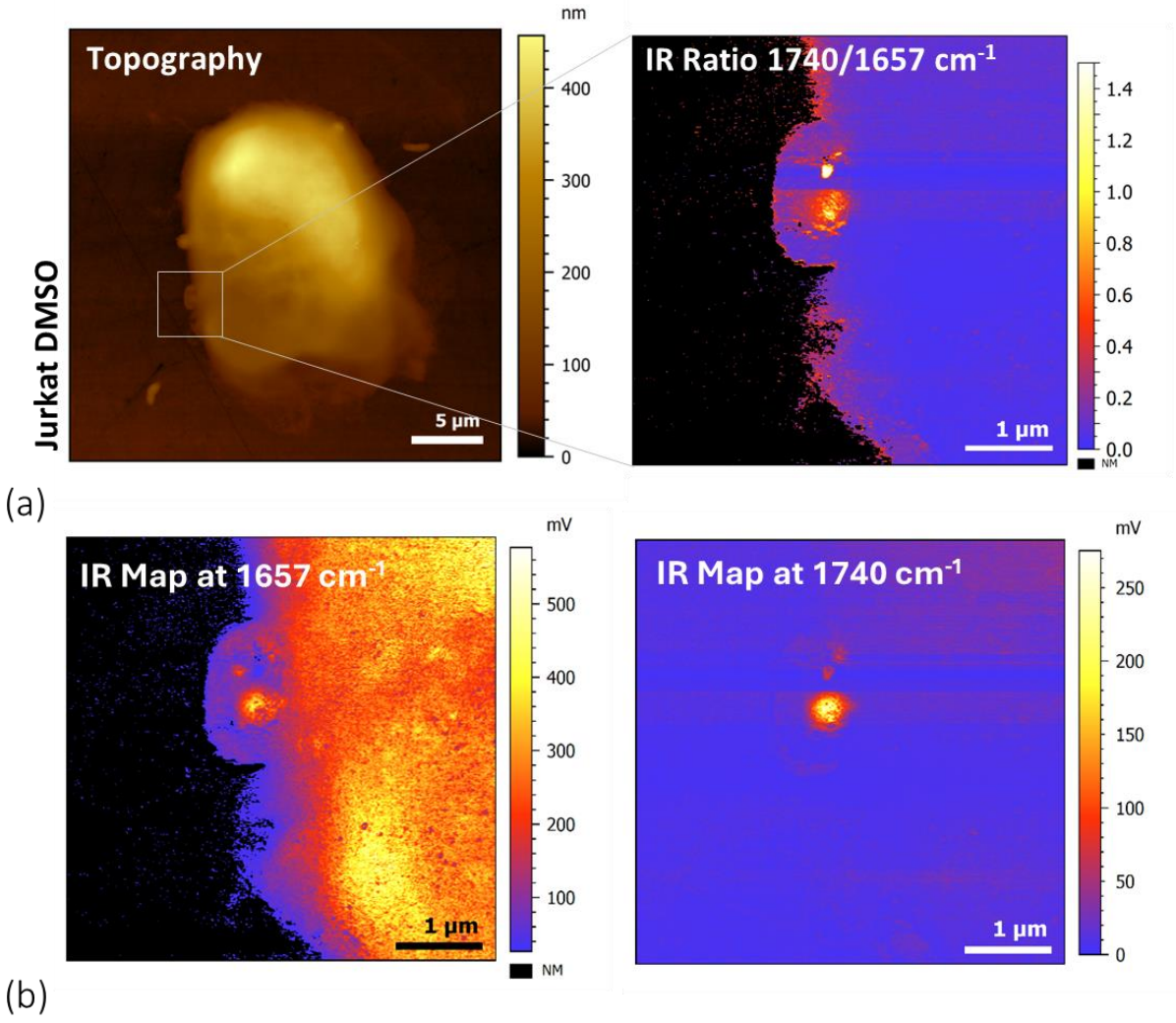

Figure 42: Characteristic IR responses of an EV (Jurkat DMSO-treated) at 1657 cm^{-1} and 1740 cm^{-1}
(a) Topography of a Jurkat DMSO-treated cell surrounded by multiple EV in the extracellular space as well as near the outer cell membrane. From one of the EVs near the membrane the IR ratio between 1740/1657 cm^{-1} is displayed in an enlarged image section. (b) IR maps at 1657 and 1740 cm^{-1} of the same zoomed section. The laser pulse rate was 200 kHz at 100 ns pulse width. The laser powers were 9.79% for 1740 cm^{-1} and 5.77% for 1657 cm^{-1}.

To precise the content of the EVs, local spectra were recorded on ROI 2 EVs (Figure 43). A significant increase in the carbonyl ester stretching band at 1740 cm^{-1} with a simultaneous decrease in the amide I and II bands is observed (Figure 43 (b)). Further differences are recognizable: a clear structure for CH bending bands is visible at 1455 cm^{-1} (CH_2 scissoring/CH_3 antisymmetric bending vibration, lipids/proteins), 1384 cm^{-1} (CH_3 symmetric bending, lipids) and 1307 cm^{-1} (associated with C-H wagging vibrations), which are evolving in the same direction as the carbonyl ester band. A weak band at 1264 cm^{-1} could be assigned to C-O stretching of lipid hydroperoxides or O-H bending (in plane) and is associated to 1740 cm^{-1}, whereas the increase of 1384 cm^{-1} can be associated with shortened lipidic fatty acids causing more CH_3 groups.[54] The band area ratio between 1384/1455 cm^{-1} is significantly increased for EV 1 (ratio 2.48) and less for EV 2 (1.34) while EV 3 and the main cell have comparably

low ratio values of 0.57 and 0.60. For further experiments IR mappings at 1455 cm^{-1} and 1384 cm^{-1} could be proposed to compare the chain length of the lipids.

The amide I band exhibits an unusual structure: centred at 1660 cm^{-1} with a shoulder at 1684 cm^{-1}. This wavenumber can be associated with the secondary β-turn structure of proteins[51], or what was also observed in the literature, is, that during cell apoptosis, the FWHM of the amide I band increases. Since the transition from laser chip three to four of the mid-IR excitation laser is also located in this area, this band shoulder could have been artificially created or unintentionally amplified during the break correction of the chip transition.

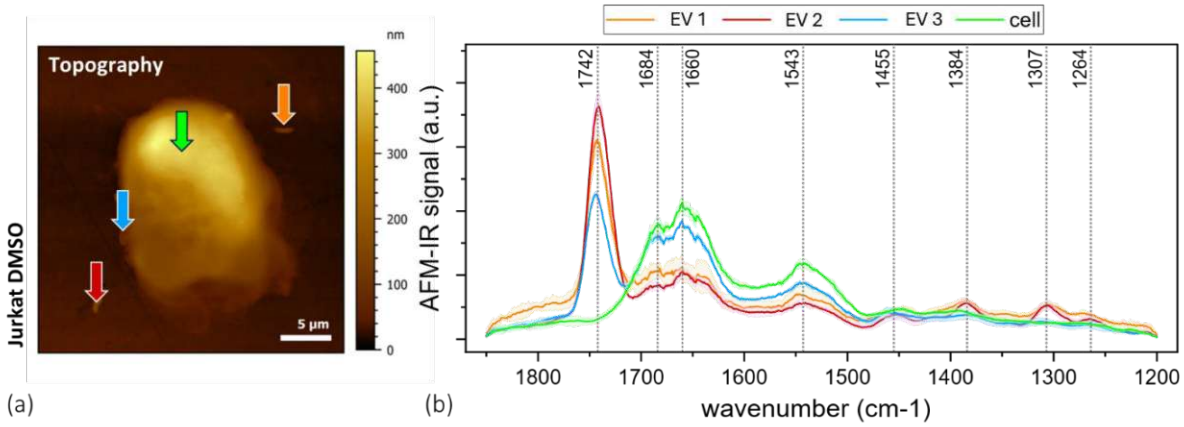

Figure 43: Local spectra of EVS compared to the response at the main cell.
(a) Topographic representation of the cell and surrounding EVs with position labelling of the local spectra. (b) Chemical characterisation of the previously defined ROI 2 in comparison to averaged cell spectrum.

Multiple extracellular vesicles were found next to cells or in the extracellular space for several treatment conditions on both model cell lines. These exhibited partly pronounced amide I signals and partly a pronounced signal for carbonyl ester bands.

Local spectra demonstrate a clear rise in the carbonyl ester band with a simultaneous increase, shift, or appearance of the bands 1384, 1306 and 1264 cm^{-1}. It can therefore be concluded that the EVs transport different substance groups. Within the EVs, also internal structures with different IR responses could be identified.

6 Summary and Conclusion

T-ALL is a malignant haematological cancer disease displaying low survival rates, particularly in relapsed or refractory cases. In previous studies, it was demonstrated that T-ALL were more susceptible to ferroptosis, which caused lipid peroxidation of the phospholipid cell membranes. Thus, a new generation of therapeutic agent was proposed that trigger ferroptosis in those cells. However, the actual effects of ferroptosis inducers on membranes and the chemical 'point-of-no-return' had not been investigated in detail.

So, to have a better understanding of those processes, this thesis explored the lipids peroxidation using two advanced vibrational techniques called O-PTIR and AFM-IR. Those techniques allowed investigation of the chemical composition of a sample at the sub-micrometre scale. While O-PTIR gave a general response of the cell, AFM-IR allowed a fine localisation of the peroxidised phospholipids on the cell surface. The aim of this work was the establishment, optimization and validation of an experimental protocol for sample preparation as well as instrumental conditions for the two analysis techniques. Two immortal T-ALL cell lines were selected for the study. Cell line Loucy was expected to react less sensitive to the ferroptosis inducer, while Jurkat should have responded stronger to them, due to a mutation on NOTCH1. Both cell lines were treated with the ferroptosis inducers RSL3 and APR-246.

A successful protocol for the sample pretreatment of the cells as well as the instrumental settings for O-PTIR and AFM-IR was established to detect phospholipid accumulations on the plasma membranes of *in vitro* model cell lines. Since lipid peroxidation occurs strictly localized on the cell membranes, the AFM-IR settings have to be finely tuned. Since AFM-IR probes the whole absorbing volume underneath the tip, a discrimination of the signal from the membrane from the one of the cytoplasm has to be made. Using a reference sample whose mechanical characteristics were similar to those of the cell samples, it was demonstrated that at higher pulse frequencies (1565 kHz), mainly the plasma membrane and small portions of the cytoplasm were probed. Instability of the measurements occurred particularly during IR mapping, since the technique is particularly sensitive to changes of the mechanical properties of the sample. These instabilities were compensated by reducing the scan rate, increasing the laser power and acquiring zoomed sections of the cells. Because of lacking instrument stability (Anasys nanoIR2) and high thermal drifts, a second, alternative AFM-IR system (Bruker ICON-IR) was used. That system allowed a more precise targeting and tip positioning for acquiring local spectra of well-defined positions.

The O-PTIR technique provided a global analysis for the individual cell type conditions. For the cell line Loucy, k-means clustering allowed the separation of the response to the two ferroptosis-inducers, also indicating a non-specific cell death for APR-246. The spatial resolution of O-PTIR was insufficient to localize peroxidation on cell membranes. An impairment of the cell culture Jurkat was observed, possible due to an insufficient maintenance period between defreezing and artificial ferroptosis induction. Although the Jurkat cell line generally exhibited lower cell viability, minimal maintenance times between cell storage and treatment proved to have an unquantifiable effect on the resulting phospholipid peroxidation. A higher lipid peroxidation is expected but cannot be stated with certainty as the negative control sample was not in suitable condition.

The optimised AFM-IR protocol confirms the sample problem for the Jurkat cell line. For this cell line, IR map ratios 1740/1657 cm^{-1} (characteristic C=O band for esterified and peroxidized phospholipids/total protein content) at 1565 kHz reveal high responses of phospholipid peroxidation already for non-treated cells. Concise phospholipid peroxide accumulations on the cell body as well as in the pseudopodia region were also observed for RSL3-treated Jurkat cells. Less phospholipid peroxidation can be noted for Loucy cells. Local spectra on intense ratio hotspots, particularly for ferroptosis-induced Jurkat cells, revealed a proportional enhancement of the bands at 1248, 1180 and 1130 cm^{-1}, in addition to an increased 1740 cm^{-1} band. These bands might be assigned to the C-O stretching vibrations of different peroxide species.

Multiple extracellular vesicles exhibiting prominent C=O stretching bands at 1742 cm^{-1} were observed around several cell conditions on both model cell lines. These displayed intervesicle as well as intravesicle differences in IR maps as well as in local spectra. The differences indicate that they belong to different categories or are transporters for different molecule classes.

However, the following aspects still need to be included in further investigations:

The negative samples of the Jurkat cell line posed a limited value, since it already revealed distinct signs of lipid peroxidation in IR maps as well as in local spectra. This was caused either due to an impaired cell integrity or remaining effects from DMSO, which was used as antifreeze agent as well as a solvent for the ferroptosis-inducer preparation. A repetition of the measurements should therefore have a maintenance period of at least three weeks and the amount of DMSO has to be reduced to a minimum in the ferroptosis inducer stock solutions.

In order to compare results between treatment-conditions and cell lines, not only the integrity of the negative control samples must be guaranteed, also the statistical significance of the investigation has to be improved. For a significant conclusion about the statistical relevance of the obtained findings, at

least four different cell cultures must be analysed for each treatment condition (control, DMSO, RSL3 and APR-246). For a global analysis, each repetition of the respective cell culture condition should be analysed on three consecutive days. In this study three to five cells per condition and cell line were investigated. To obtain valid repetitive information at intracellular level regarding the local distribution of lipid peroxidation, the number of analysed cells has to be significantly increased.

For further studies the inclusion of alternative treatment durations and concentrations can be considered. Peroxidised phospholipids require a certain time period to accumulate at the membrane in order to be detectable after being exposed to the ferroptosis-inducer. This must be taken into account for repeated analysis. At the same time the cell integrity must remain intact.

The continuation of EV investigations could be an exciting extension for subsequent series of experiments. Since only EVs next to or far from the main cell were investigated in this study, an attempt could be made to investigate EVs during their formation, ergo the protrusion of the external or endosomal membrane. Related to this, the effects of a higher concentration of the ferroptosis inducer or duration could be tested on EV behaviour, formation, and their transported load.

Bibliography

(1) Ravid, K.; Licht, J. D. *Transcription Factors: Normal and Malignant Development of Blood Cells*; Wiley-Liss: New York, 2001.

(2) Sun, L.; Su, Y.; Jiao, A.; Wang, X.; Zhang, B. T Cells in Health and Disease. *Signal Transduct. Target. Ther.* **2023**, *8* (1), 235. https://doi.org/10.1038/s41392-023-01471-y.

(3) *Immunobiology: The Immune System in Health and Disease*, 5. ed.; Janeway, C. A., Ed.; Garland Publ. [u.a.]: New York, NY, 2001.

(4) Ehsanpour, A.; Saki, N.; Bagheri, M.; Maleki Behzad, M.; Abroun, S. The Expression of Microvesicles in Leukemia: Prognostic Approaches. *Cell J. Yakhteh* **2019**, *21* (2), 115–123. https://doi.org/10.22074/cellj.2019.5847.

(5) de Araújo, N. D.; Gama, F. M.; de Souza Barros, M.; Ribeiro, T. L. P.; Alves, F. S.; Xabregas, L. A.; Tarragô, A. M.; Malheiro, A.; Costa, A. G. Translating Unconventional T Cells and Their Roles in Leukemia Antitumor Immunity. *J. Immunol. Res.* **2021**, *2021*, 6633824. https://doi.org/10.1155/2021/6633824.

(6) Van Vlierberghe, P.; Ferrando, A. The Molecular Basis of T Cell Acute Lymphoblastic Leukemia. *J. Clin. Invest.* **2012**, *122* (10), 3398–3406. https://doi.org/10.1172/JCI61269.

(7) Abolhasani, S.; Hejazian, S. S.; Karpisheh, V.; Khodakarami, A.; Mohammadi, H.; Gholizadeh Navashenaq, J.; Hojjat-Farsangi, M.; Jadidi-Niaragh, F. The Role of SF3B1 and NOTCH1 in the Pathogenesis of Leukemia. *IUBMB Life* **2023**, *75* (3), 257–278. https://doi.org/10.1002/iub.2660.

(8) Raetz, E. A.; Teachey, D. T. T-Cell Acute Lymphoblastic Leukemia. *Hematology* **2016**, *2016* (1), 580–588. https://doi.org/10.1182/asheducation-2016.1.580.

(9) Pui, C.-H. Treatment of Acute Lymphoblastic Leukemia. *N Engl J Med* **2006**.

(10) Cordo', V.; van der Zwet, J. C. G.; Canté-Barrett, K.; Pieters, R.; Meijerink, J. P. P. T-Cell Acute Lymphoblastic Leukemia: A Roadmap to Targeted Therapies. *Blood Cancer Discov.* **2021**, *2* (1), 19–31. https://doi.org/10.1158/2643-3230.BCD-20-0093.

(11) Chiaretti, S.; Foà, R. T-Cell Acute Lymphoblastic Leukemia. *Haematologica* **2009**, *94* (2), 160–162. https://doi.org/10.3324/haematol.2008.004150.

(12) Zhou, B.; Lin, W.; Long, Y.; Yang, Y.; Zhang, H.; Wu, K.; Chu, Q. Notch Signaling Pathway: Architecture, Disease, and Therapeutics. *Signal Transduct. Target. Ther.* **2022**, *7* (1), 95. https://doi.org/10.1038/s41392-022-00934-y.

(13) Paganelli, F.; Lonetti, A.; Anselmi, L.; Martelli, A. M.; Evangelisti, C.; Chiarini, F. New Advances in Targeting Aberrant Signaling Pathways in T-Cell Acute Lymphoblastic Leukemia. *Adv. Biol. Regul.* **2019**, *74*, 100649. https://doi.org/10.1016/j.jbior.2019.100649.

(14) Wang, Z.; Hu, H.; Heitink, L.; Rogers, K.; You, Y.; Tan, T.; Suen, C. L. W.; Garnham, A.; Chen, H.; Lieschke, E.; Diepstraten, S. T.; Chang, C.; Chen, T.; Moujalled, D.; Sutherland, K.; Lessene, G.; Sieber, O. M.; Visvader, J.; Kelly, G. L.; Strasser, A. The Anti-Cancer Agent APR-246 Can Activate Several Programmed Cell Death Processes to Kill Malignant Cells. *Cell Death Differ.* **2023**, *30* (4), 1033–1046. https://doi.org/10.1038/s41418-023-01122-3.

(15) National Center for Biotechnology Information. *Prima-1met*. PubChem Compound Summary for CID 52918385. https://pubchem.ncbi.nlm.nih.gov/compound/52918385 (accessed 2024-04-28).

(16) Freed-Pastor, W. A.; Prives, C. Mutant P53: One Name, Many Proteins. *Genes Dev.* **2012**, *26* (12), 1268–1286. https://doi.org/10.1101/gad.190678.112.

(17) Cooper, G. M. Oncogenes. In *The Cell: A Molecular Approach. 2nd edition*; Sinauer Associates, 2000.

(18) Jiang, X.; Stockwell, B. R.; Conrad, M. Ferroptosis: Mechanisms, Biology and Role in Disease. *Nat. Rev. Mol. Cell Biol.* **2021**, *22* (4), 266–282. https://doi.org/10.1038/s41580-020-00324-8.

(19) Dixon, S. J.; Lemberg, K. M.; Lamprecht, M. R.; Skouta, R.; Zaitsev, E. M.; Gleason, C. E.; Patel, D. N.; Bauer, A. J.; Cantley, A. M.; Yang, W. S.; Morrison, B.; Stockwell, B. R. Ferroptosis: An Iron-Dependent Form of Nonapoptotic Cell Death. *Cell* **2012**, *149* (5), 1060–1072. https://doi.org/10.1016/j.cell.2012.03.042.

(20) Yang, W. S.; Stockwell, B. R. Ferroptosis: Death by Lipid Peroxidation. *Trends Cell Biol.* **2016**, *26* (3), 165–176. https://doi.org/10.1016/j.tcb.2015.10.014.
(21) Lei, G.; Zhuang, L.; Gan, B. Targeting Ferroptosis as a Vulnerability in Cancer. *Nat. Rev. Cancer* **2022**, *22* (7), 381–396. https://doi.org/10.1038/s41568-022-00459-0.
(22) Stockwell, B. R.; Friedmann Angeli, J. P.; Bayir, H.; Bush, A. I.; Conrad, M.; Dixon, S. J.; Fulda, S.; Gascón, S.; Hatzios, S. K.; Kagan, V. E.; Noel, K.; Jiang, X.; Linkermann, A.; Murphy, M. E.; Overholtzer, M.; Oyagi, A.; Pagnussat, G. C.; Park, J.; Ran, Q.; Rosenfeld, C. S.; Salnikow, K.; Tang, D.; Torti, F. M.; Torti, S. V.; Toyokuni, S.; Woerpel, K. A.; Zhang, D. D. Ferroptosis: A Regulated Cell Death Nexus Linking Metabolism, Redox Biology, and Disease. *Cell* **2017**, *171* (2), 273–285. https://doi.org/10.1016/j.cell.2017.09.021.
(23) Rodriguez, R.; Schreiber, S. L.; Conrad, M. Persister Cancer Cells: Iron Addiction and Vulnerability to Ferroptosis. *Mol. Cell* **2022**, *82* (4), 728–740. https://doi.org/10.1016/j.molcel.2021.12.001.
(24) Sui, X.; Zhang, R.; Liu, S.; Duan, T.; Zhai, L.; Zhang, M.; Han, X.; Xiang, Y.; Huang, X.; Lin, H.; Xie, T. RSL3 Drives Ferroptosis Through GPX4 Inactivation and ROS Production in Colorectal Cancer. *Front. Pharmacol.* **2018**, *9*, 1371. https://doi.org/10.3389/fphar.2018.01371.
(25) Dai, E.; Meng, L.; Kang, R.; Wang, X.; Tang, D. ESCRT-III–Dependent Membrane Repair Blocks Ferroptosis. *Biochem. Biophys. Res. Commun.* **2020**, *522* (2), 415–421. https://doi.org/10.1016/j.bbrc.2019.11.110.
(26) Dolma, S.; Lessnick, S. L.; Hahn, W. C.; Stockwell, B. R. Identification of Genotype-Selective Antitumor Agents Using Synthetic Lethal Chemical Screening in Engineered Human Tumor Cells. *Cancer Cell* **2003**, *3* (3), 285–296. https://doi.org/10.1016/S1535-6108(03)00050-3.
(27) Lauritzen, S. P.; Boye, T. L.; Nylandsted, J. Annexins Are Instrumental for Efficient Plasma Membrane Repair in Cancer Cells. *Semin. Cell Dev. Biol.* **2015**, *45*, 32–38. https://doi.org/10.1016/j.semcdb.2015.10.028.
(28) Dixon, S. J.; Stockwell, B. R. The Role of Iron and Reactive Oxygen Species in Cell Death. *Nat. Chem. Biol.* **2014**, *10* (1), 9–17. https://doi.org/10.1038/nchembio.1416.
(29) Yang, W. S.; SriRamaratnam, R.; Welsch, M. E.; Shimada, K.; Skouta, R.; Viswanathan, V. S.; Cheah, J. H.; Clemons, P. A.; Shamji, A. F.; Clish, C. B.; Brown, L. M.; Girotti, A. W.; Cornish, V. W.; Schreiber, S. L.; Stockwell, B. R. Regulation of Ferroptotic Cancer Cell Death by GPX4. *Cell* **2014**, *156* (1–2), 317–331. https://doi.org/10.1016/j.cell.2013.12.010.
(30) Kumada, H.; Itoh, M.; Tohda, S. Effect of Ferroptosis Inducers and Inhibitors on Cell Proliferation in Acute Leukemia. *Anticancer Res.* **2024**, *44* (3), 1003–1010. https://doi.org/10.21873/anticanres.16895.
(31) Jiang, L.; Kon, N.; Li, T.; Wang, S.-J.; Su, T.; Hibshoosh, H.; Baer, R.; Gu, W. Ferroptosis as a P53-Mediated Activity during Tumour Suppression. *Nature* **2015**, *520* (7545), 57–62. https://doi.org/10.1038/nature14344.
(32) Failla, M. The Oncogene NOTCH1 Conveys a Vulnerability to Ferroptosis: An Iron-Solid Strategy to Tackle T Cell Acute Lymphoblastic Leukemia, 2023.
(33) Yang, W. S.; Stockwell, B. R. Synthetic Lethal Screening Identifies Compounds Activating Iron-Dependent, Nonapoptotic Cell Death in Oncogenic-RAS-Harboring Cancer Cells. *Chem. Biol.* **2008**, *15* (3), 234–245. https://doi.org/10.1016/j.chembiol.2008.02.010.
(34) National Center for Biotechnology Information. *(1S,3R)-Rsl3*. PubChem Compound Summary for CID 1750826. https://pubchem.ncbi.nlm.nih.gov/compound/1750826 (accessed 2024-04-28).
(35) Michels, J.; Venkatesh, D.; Liu, C.; Budhu, S.; Zhong, H.; George, M. M.; Thach, D.; Yao, Z.-K.; Ouerfelli, O.; Liu, H.; Stockwell, B. R.; Campesato, L. F.; Zamarin, D.; Zappasodi, R.; Wolchok, J. D.; Merghoub, T. APR-246 Increases Tumor Antigenicity Independent of P53. *Life Sci. Alliance* **2023**, *7* (1), e202301999. https://doi.org/10.26508/lsa.202301999.
(36) Li, X.-L.; Zhou, J.; Chan, Z.-L.; Chooi, J.-Y.; Chen, Z.-R.; Chng, W.-J. PRIMA-1met (APR-246) Inhibits Growth of Colorectal Cancer Cells with Different P53 Status through Distinct Mechanisms. *Oncotarget* **2015**, *6* (34), 36689–36699.
(37) Schneider, U.; Schwenk, H. U.; Bornkamm, G. Characterization of EBV-Genome Negative "Null" and "T" Cell Lines Derived from Children with Acute Lymphoblastic Leukemia and Leukemic

Transformed Non-Hodgkin Lymphoma. *Int. J. Cancer* **1977**, *19* (5), 621–626. https://doi.org/10.1002/ijc.2910190505.
(38) ATCC®. *Jurkat, Clone E6-1 - TIB-152™*. www.atcc.org. https://www.atcc.org/products/tib-152 (accessed 2024-01-24).
(39) ATCC®. *Loucy - CRL-2629™*. www.atcc.org. https://www.atcc.org/products/crl-2629 (accessed 2024-01-24).
(40) Thompson, J. M. *Infrared Spectroscopy*; Pan Stanford publishing: Singapore, 2018.
(41) Bacsik, Z.; Mink, J.; Keresztury, G. FTIR Spectroscopy of the Atmosphere. I. Principles and Methods. *Appl. Spectrosc. Rev.* **2004**, *39* (3), 295–363. https://doi.org/10.1081/ASR-200030192.
(42) Levin, I. W.; Bhargava, R. Fourier Transform Infrared Vibrational Spectroscopic Imaging: Integrating Microscopy and Molecular Recognition. *Annu. Rev. Phys. Chem.* **2005**, *56*, 429–474. https://doi.org/10.1146/annurev.physchem.56.092503.141205.
(43) Baker, M. J.; Trevisan, J.; Bassan, P.; Bhargava, R.; Butler, H. J.; Dorling, K. M.; Fielden, P. R.; Fogarty, S. W.; Fullwood, N. J.; Heys, K. A.; Hughes, C.; Lasch, P.; Martin-Hirsch, P. L.; Obinaju, B.; Sockalingum, G. D.; Sulé-Suso, J.; Strong, R. J.; Walsh, M. J.; Wood, B. R.; Gardner, P.; Martin, F. L. Using Fourier Transform IR Spectroscopy to Analyze Biological Materials. *Nat. Protoc.* **2014**, *9* (8), 1771–1791. https://doi.org/10.1038/nprot.2014.110.
(44) Naumann, D. Ft-Infrared and Ft-Raman Spectroscopy in Biomedical Research. *Appl. Spectrosc. Rev.* **2001**, *36* (2–3), 239–298. https://doi.org/10.1081/ASR-100106157.
(45) Socrates, G.; Socrates, G. *Infrared and Raman Characteristic Group Frequencies: Tables and Charts*, 3rd ed.; Wiley: Chichester ; New York, 2001.
(46) Wang, R.; Wang, Y. Fourier Transform Infrared Spectroscopy in Oral Cancer Diagnosis. *Int. J. Mol. Sci.* **2021**, *22* (3), 1206. https://doi.org/10.3390/ijms22031206.
(47) Toyran, N.; Lasch, P.; Naumann, D.; Turan, B.; Severcan, F. Early Alterations in Myocardia and Vessels of the Diabetic Rat Heart: An FTIR Microspectroscopic Study. *Biochem. J.* **2006**, *397* (3), 427–436. https://doi.org/10.1042/BJ20060171.
(48) Olsztyńska-Janus, S.; Pietruszka, A.; Kiełbowicz, Z.; Czarnecki, M. A. ATR-IR Study of Skin Components: Lipids, Proteins and Water. Part I: Temperature Effect. *Spectrochim. Acta. A. Mol. Biomol. Spectrosc.* **2018**, *188*, 37–49. https://doi.org/10.1016/j.saa.2017.07.001.
(49) Lewis, R. N. A. H.; McElhaney, R. N. The Structure and Organization of Phospholipid Bilayers as Revealed by Infrared Spectroscopy. *Chem. Phys. Lipids* **1998**, *96* (1), 9–21. https://doi.org/10.1016/S0009-3084(98)00077-2.
(50) Paluszkiewicz, C.; Piergies, N.; Chaniecki, P.; Rękas, M.; Miszczyk, J.; Kwiatek, W. M. Differentiation of Protein Secondary Structure in Clear and Opaque Human Lenses: AFM – IR Studies. *J. Pharm. Biomed. Anal.* **2017**, *139*, 125–132. https://doi.org/10.1016/j.jpba.2017.03.001.
(51) Kong, J.; Yu, S. Fourier Transform Infrared Spectroscopic Analysis of Protein Secondary Structures. *Acta Biochim. Biophys. Sin.* **2007**, *39* (8), 549–559. https://doi.org/10.1111/j.1745-7270.2007.00320.x.
(52) Oleszko, A.; Olsztyńska-Janus, S.; Walski, T.; Grzeszczuk-Kuć, K.; Bujok, J.; Gałecka, K.; Czerski, A.; Witkiewicz, W.; Komorowska, M. Application of FTIR-ATR Spectroscopy to Determine the Extent of Lipid Peroxidation in Plasma during Haemodialysis. *BioMed Res. Int.* **2015**, *2015* (1), 245607. https://doi.org/10.1155/2015/245607.
(53) Dazzi, A.; Prater, C. B.; Hu, Q.; Chase, D. B.; Rabolt, J. F.; Marcott, C. AFM–IR: Combining Atomic Force Microscopy and Infrared Spectroscopy for Nanoscale Chemical Characterization. *Appl. Spectrosc.* **2012**, *66* (12), 1365–1384. https://doi.org/10.1366/12-06804.
(54) Valenta, H.; Dupré-Crochet, S.; Abdesselem, M.; Bizouarn, T.; Baciou, L.; Nüsse, O.; Deniset-Besseau, A.; Erard, M. Consequences of the Constitutive NOX2 Activity in Living Cells: Cytosol Acidification, Apoptosis, and Localized Lipid Peroxidation. *Biochim. Biophys. Acta BBA - Mol. Cell Res.* **2022**, *1869* (9), 119276. https://doi.org/10.1016/j.bbamcr.2022.119276.
(55) Faroux, J. M.; Ureta, M. M.; Tymczyszyn, E. E.; Gómez-Zavaglia, A. An Overview of Peroxidation Reactions Using Liposomes as Model Systems and Analytical Methods as Monitoring Tools.

Colloids Surf. B Biointerfaces **2020**, *195*, 111254. https://doi.org/10.1016/j.colsurfb.2020.111254.
(56) Lasch, P.; Naumann, D. Spatial Resolution in Infrared Microspectroscopic Imaging of Tissues. *Biochim. Biophys. Acta BBA - Biomembr.* **2006**, *1758* (7), 814–829. https://doi.org/10.1016/j.bbamem.2006.06.008.
(57) Watt, I. M. *The Principles and Practice of Electron Microscopy*, 2nd ed.; Cambridge University Press: Cambridge, 1997. https://doi.org/10.1017/CBO9781139170529.
(58) Tamburini, F.; Anzolin, G.; Umbriaco, G.; Bianchini, A.; Barbieri, C. Overcoming the Rayleigh Criterion Limit with Optical Vortices. *Phys. Rev. Lett.* **2006**, *97* (16), 163903. https://doi.org/10.1103/PhysRevLett.97.163903.
(59) Dazzi, A.; Prazeres, R.; Glotin, F.; Ortega, J. M. Local Infrared Microspectroscopy with Subwavelength Spatial Resolution with an Atomic Force Microscope Tip Used as a Photothermal Sensor. *Opt. Lett.* **2005**, *30* (18), 2388. https://doi.org/10.1364/OL.30.002388.
(60) Schwaighofer, A.; Brandstetter, M.; Lendl, B. Quantum Cascade Lasers (QCLs) in Biomedical Spectroscopy. *Chem. Soc. Rev.* **2017**, *46* (19), 5903–5924. https://doi.org/10.1039/C7CS00403F.
(61) Bai, Y.; Zhang, D.; Li, C.; Liu, C.; Cheng, J.-X. Bond-Selective Imaging of Cells by Mid-Infrared Photothermal Microscopy in High Wavenumber Region. *J. Phys. Chem. B* **2017**, *121* (44), 10249–10255. https://doi.org/10.1021/acs.jpcb.7b09570.
(62) Bai, Y.; Yin, J.; Cheng, J.-X. Bond-Selective Imaging by Optically Sensing the Mid-Infrared Photothermal Effect. *Sci. Adv.* **2021**, *7* (20), eabg1559. https://doi.org/10.1126/sciadv.abg1559.
(63) Dazzi, A.; Glotin, F.; Carminati, R. Theory of Infrared Nanospectroscopy by Photothermal Induced Resonance. *J. Appl. Phys.* **2010**, *107* (12), 124519. https://doi.org/10.1063/1.3429214.
(64) Photothermal spectroscopy Corp. mIRage® Data Sheet, 2022. https://www.photothermal.com/home/mirage/ (accessed 2024-07-09).
(65) *O-PTIR non-contact submicron visible probe infrared spectroscopy*. Optical photothermal infrared and Raman spectroscopy with the mIRage. https://www.photothermal.com/home/o-ptir/ (accessed 2024-04-25).
(66) Kansiz, M.; Prater, C.; Dillon, E.; Lo, M.; Anderson, J.; Marcott, C.; Demissie, A.; Chen, Y.; Kunkel, G. Optical Photothermal Infrared Microspectroscopy with Simultaneous Raman – A New Non-Contact Failure Analysis Technique for Identification of <10 Mm Organic Contamination in the Hard Drive and Other Electronics Industries. *Microsc. Today* **2020**, *28* (3), 26–36. https://doi.org/10.1017/s1551929520000917.
(67) Lossius, S. Investigating Subcellular Structures in Micro-Organisms Using Infrared Spectroscopy-Based Techniques - Comparison between the Latest Micro and Nano Infrared Technologies, 2023.
(68) Eaton, P.; West, P. *Atomic Force Microscopy*; Oxford University Press, 2010. https://doi.org/10.1093/acprof:oso/9780199570454.001.0001.
(69) Magonov, S. N.; Whangbo, M. *Surface Analysis with STM and AFM: Experimental and Theoretical Aspects of Image Analysis*, 1st ed.; Wiley, 1995. https://doi.org/10.1002/9783527615117.
(70) Ramer, D. G. Development and Characterization of a Near-Field Infrared Microscope by the Coupling of AFM and QCL Spectroscopy, Technical University Vienna, Vienna, 2016.
(71) Katzenmeyer, A. M.; Holland, G.; Chae, J.; Band, A.; Kjoller, K.; Centrone, A. Mid-Infrared Spectroscopy beyond the Diffraction Limit via Direct Measurement of the Photothermal Effect. *Nanoscale* **2015**, *7* (42), 17637–17641. https://doi.org/10.1039/C5NR04854K.
(72) Lu, F.; Belkin, M. A. Infrared Absorption Nano-Spectroscopy Using Sample Photoexpansion Induced by Tunable Quantum Cascade Lasers. *Opt. Express* **2011**, *19* (21), 19942–19947. https://doi.org/10.1364/OE.19.019942.
(73) Mathurin, J.; Deniset-Besseau, A.; Bazin, D.; Dartois, E.; Wagner, M.; Dazzi, A. Photothermal AFM-IR Spectroscopy and Imaging: Status, Challenges, and Trends. *J. Appl. Phys.* **2022**, *131* (1), 010901. https://doi.org/10.1063/5.0063902.
(74) Rhee, W.; Yu, Z. *Phase-Locked Loops: System Perspectives and Circuit Design Aspects*, 1st ed.; Wiley, 2024. https://doi.org/10.1002/9781119909071.

(75) Quaroni, L. Understanding and Controlling Spatial Resolution, Sensitivity, and Surface Selectivity in Resonant-Mode Photothermal-Induced Resonance Spectroscopy. *Anal. Chem.* **2020**, *92* (5), 3544–3554. https://doi.org/10.1021/acs.analchem.9b03468.
(76) Zhang, J.; Khanal, D.; Banaszak Holl, M. M. Applications of AFM-IR for Drug Delivery Vector Characterization: Infrared, Thermal, and Mechanical Characterization at the Nanoscale. *Adv. Drug Deliv. Rev.* **2023**, *192*, 114646. https://doi.org/10.1016/j.addr.2022.114646.
(77) Dazzi, A.; Prazeres, R.; Glotin, F.; Ortega, J. M.; Al-Sawaftah, M.; de Frutos, M. Chemical Mapping of the Distribution of Viruses into Infected Bacteria with a Photothermal Method. *Ultramicroscopy* **2008**, *108* (7), 635–641. https://doi.org/10.1016/j.ultramic.2007.10.008.
(78) Dazzi, A.; Prazeres, R.; Glotin, F.; Ortega, J. M. Subwavelength Infrared Spectromicroscopy Using an AFM as a Local Absorption Sensor. *Infrared Phys. Technol.* **2006**, *49* (1), 113–121. https://doi.org/10.1016/j.infrared.2006.01.009.
(79) Hermes, M.; Morrish, R. B.; Huot, L.; Meng, L.; Junaid, S.; Tomko, J.; Lloyd, G. R.; Masselink, W. T.; Tidemand-Lichtenberg, P.; Pedersen, C.; Palombo, F.; Stone, N. Mid-IR Hyperspectral Imaging for Label-Free Histopathology and Cytology. *J. Opt.* **2018**, *20* (2), 023002. https://doi.org/10.1088/2040-8986/aaa36b.
(80) Jin, X.; Han, J. K-Means Clustering. In *Encyclopedia of Machine Learning*; Sammut, C., Webb, G. I., Eds.; Springer US: Boston, MA, 2010; pp 563–564. https://doi.org/10.1007/978-0-387-30164-8_425.
(81) Coughlin, M. F.; Schmid-Schönbein, G. W. Pseudopod Projection and Cell Spreading of Passive Leukocytes in Response to Fluid Shear Stress. *Biophys. J.* **2004**, *87* (3), 2035–2042. https://doi.org/10.1529/biophysj.104.042192.
(82) Mimae, T.; Ito, A. New Challenges in Pseudopodial Proteomics by a Laser-Assisted Cell Etching Technique. *Biochim. Biophys. Acta BBA - Proteins Proteomics* **2015**, *1854* (6), 538–546. https://doi.org/10.1016/j.bbapap.2014.10.009.
(83) Galvao, J.; Davis, B.; Tilley, M.; Normando, E.; Duchen, M. R.; Cordeiro, M. F. Unexpected Low-dose Toxicity of the Universal Solvent DMSO. *FASEB J.* **2014**, *28* (3), 1317–1330. https://doi.org/10.1096/fj.13-235440.
(84) Tunçer, S.; Gurbanov, R.; Sheraj, I.; Solel, E.; Esenturk, O.; Banerjee, S. Low Dose Dimethyl Sulfoxide Driven Gross Molecular Changes Have the Potential to Interfere with Various Cellular Processes. *Sci. Rep.* **2018**, *8* (1), 14828. https://doi.org/10.1038/s41598-018-33234-z.
(85) Willms, E.; Cabañas, C.; Mäger, I.; Wood, M. J. A.; Vader, P. Extracellular Vesicle Heterogeneity: Subpopulations, Isolation Techniques, and Diverse Functions in Cancer Progression. *Front. Immunol.* **2018**, *9*, 738. https://doi.org/10.3389/fimmu.2018.00738.
(86) Doyle, L. M.; Wang, M. Z. Overview of Extracellular Vesicles, Their Origin, Composition, Purpose, and Methods for Exosome Isolation and Analysis. *Cells* **2019**, *8* (7), 727. https://doi.org/10.3390/cells8070727.

List of Figures

List of Tables

Appendix

I. Supplemental Material

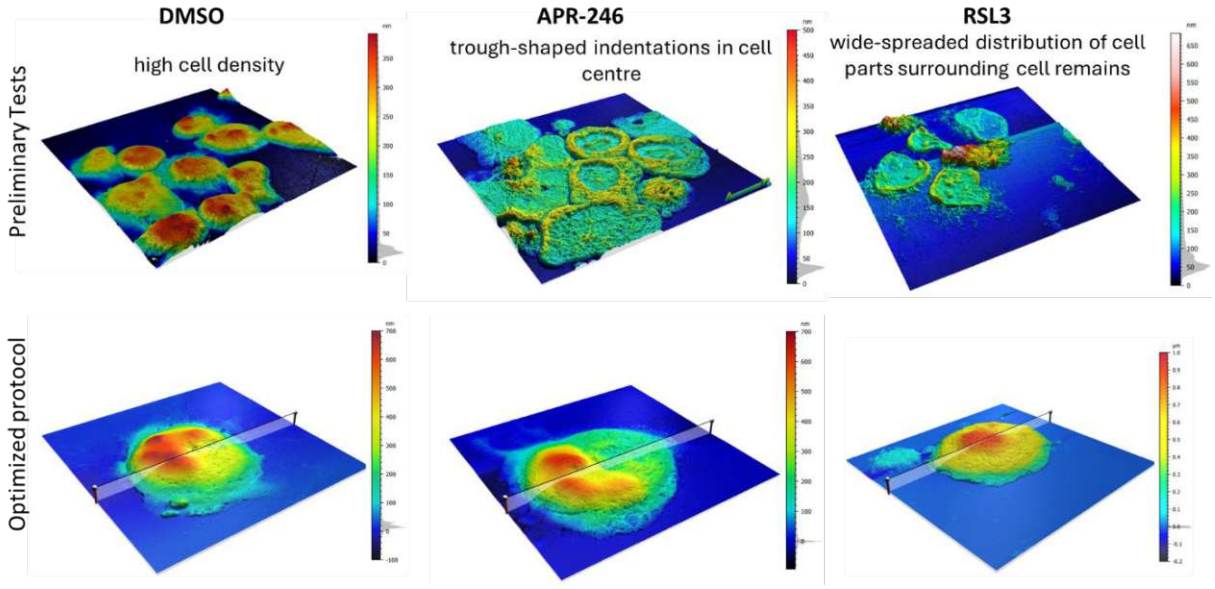

Supplemental Material 1: Comparison of the cells fixed on CaF_2 carriers prior to the optimised protocol in initial experiments. In the first experiments, mainly cell agglomerates were found, partly destroyed cells with missing nuclei or only membrane remnants. Using the optimised protocol, single cells with preserved cell integrity were obtained. The topography images are displayed in 3D and multicolour scale was used for better visualisation.

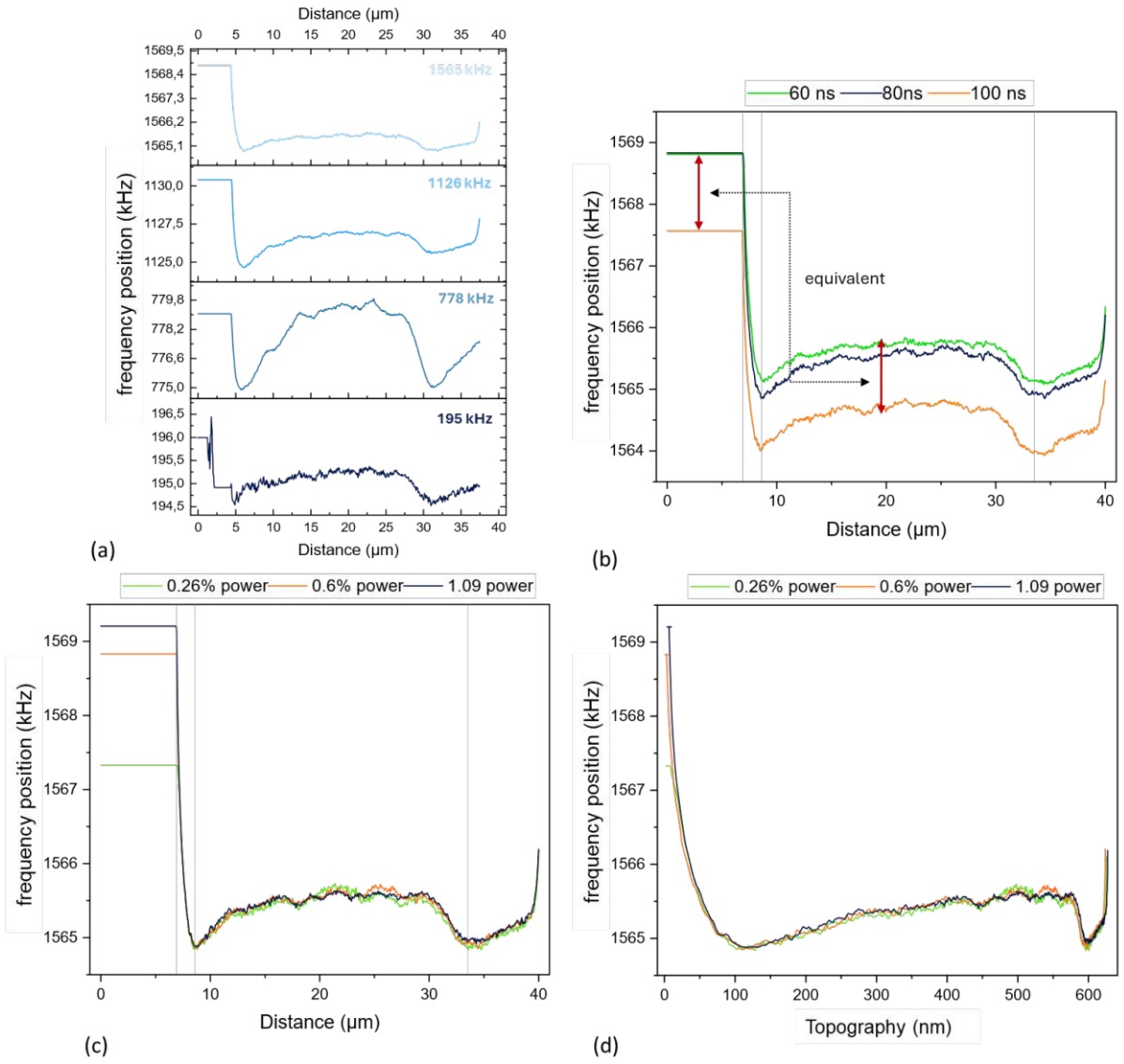

Supplemental Material 2: Evolution of the position shifts of the amplitude maxima of individual modes tracked via PLL. Comparison of different pulse rates, with fixed pulse width and laser power (80 ns, 0.6%) (b) Comparison of different pulse widths (60, 80 and 100 ns) at the same pulse rate 1565 kHz and power 0.6%. (c) Curves for different laser powers at 1565 kHz and 80 ns. (d) Comparison of the curves at different laser powers at 1565 kHz and 80 ns but plotted against the film thickness of the PMMA film instead of the measuring range distance.

A first observation is the shifting amplitude positions during the mapping in contrast to the previous pulse sweep, which was performed on a position in the centre of the PMMA film (ergo high film thickness). While the frequency positions at the Si/PMMA border remained the unchanged at 195 kHz, 1134 kHz and 1567 kHz, the amplitude of the frequency 802 kHz shifted to values around 772 kHz. This indicates a tendency of higher stabilities of the frequency modes 195 kHz, 1134 kHz and 1567 kHz even with fluctuating mechanical sample properties.

These results demonstrate a shift in frequency position amplitude (with relatively identical curves) to lower values with increasing pulse width. Notable is although the offset between 60/80 ns to 100 ns. This could be caused by the cantilever fixation or electrical components. There is no change in position with varying laser power at the same pulse width (see (c)).

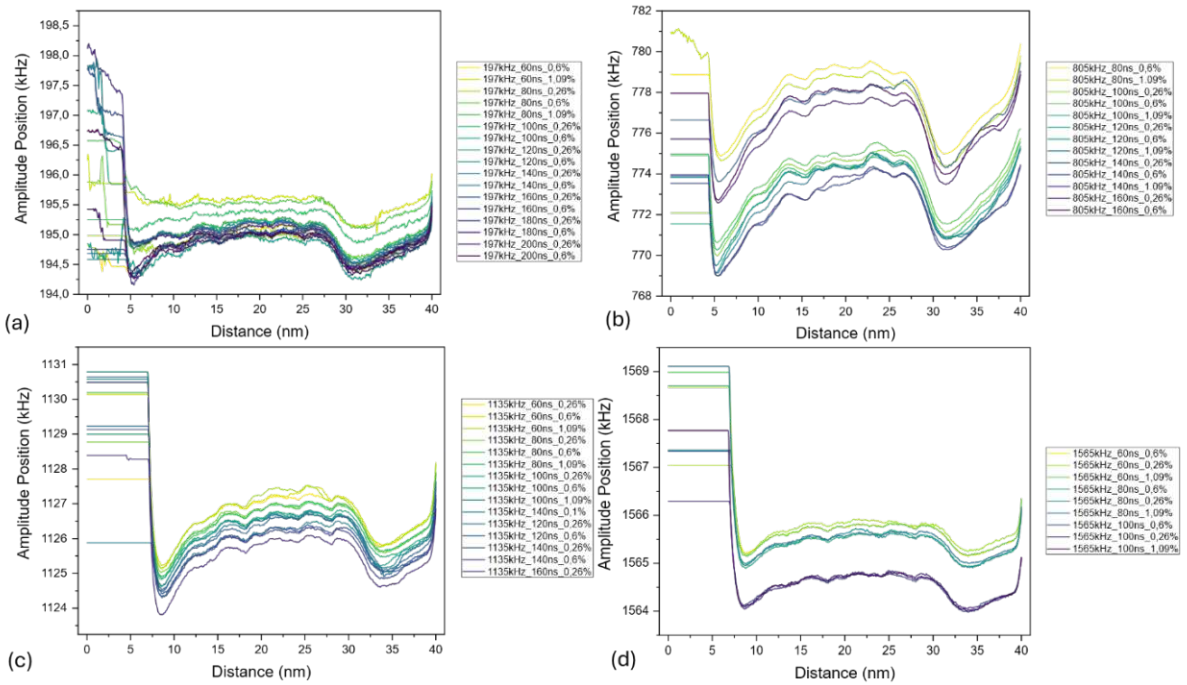

Supplemental Material 3: Illustration of all amplitude maximum shifts recorded during IR mapping via PLL. All the curves demonstrate steady values in the Si region before a sudden drop occurs at the start of the PMMA layer. The curves now reveal an oscillating behaviour with initially slowly increasing values before they level off around a certain value. From a certain distance away from Si (and thus a certain thickness of the PMMA layer), another shift to lower amplitude values occurs, which then increase linearly. The strong increase at a distance of 40 µm from the starting value can be explained by possible edge effects. (a) The plot of the 2nd cantilever mode particular shows r discontinuities in the area of the Si. The measurement settings exhibit identical curves, which are slightly shifted between 194.5 - 195.5 kHz. This curve is almost continuously shifted to lower values with higher pulse width and higher laser power. (b) A ratio of the position shift for 775 kHz cannot be determined exactly from the pulse width and laser power, but the course of the curves is identical. The plot of the amplitude shifts for 1127 kHz (c) and 1565 kHz (d) confirm the findings already given. For both blocks, a correlation of the shift to smaller values with increasing pulse width and laser power can be observed.

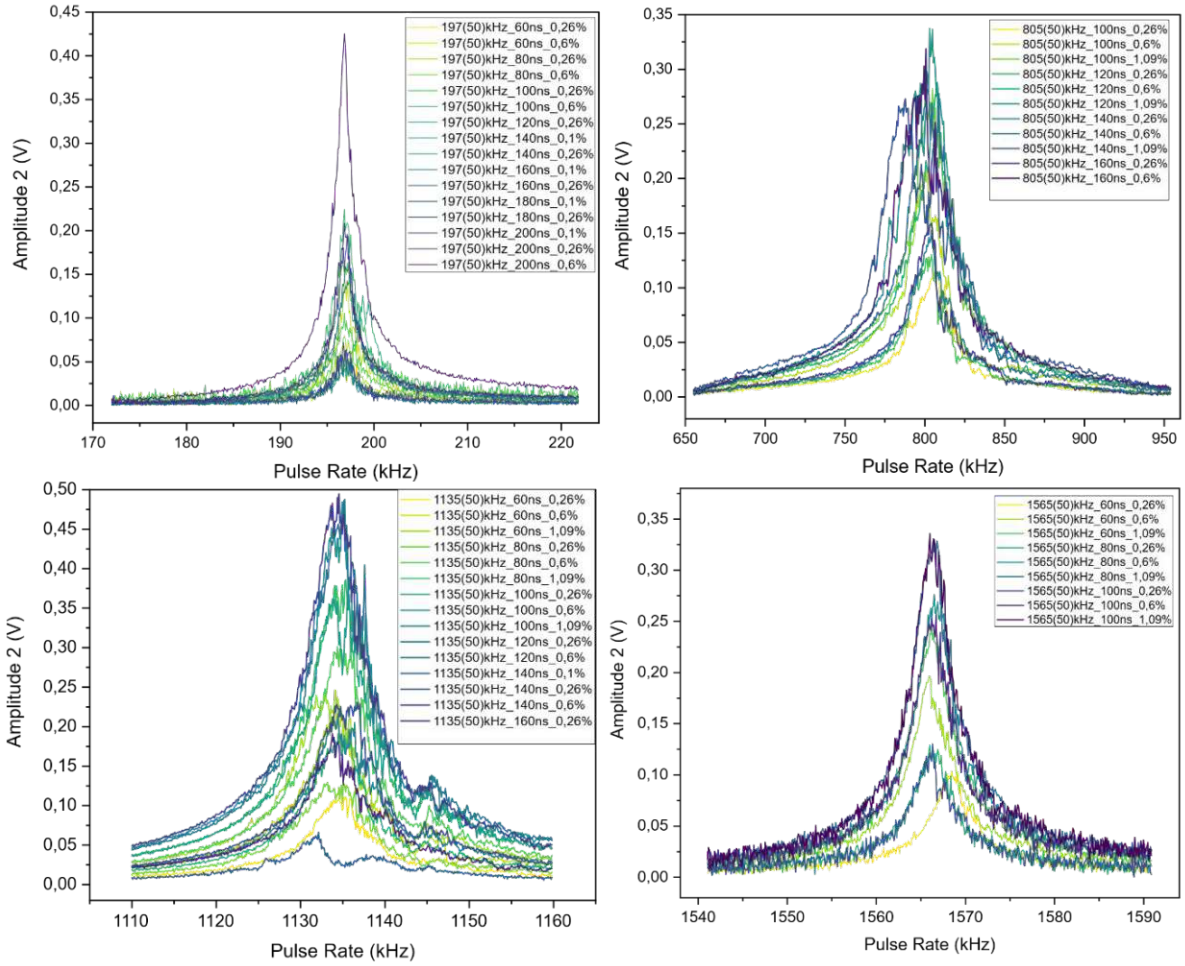

Supplemental Material 4: Presentation of the amplitude's maxima position and their corresponding peak shape for the selected cantilevers resonance frequencies around 200 kHz, 800 kHz, 1135 kHz and 1565 kHz. Either the pulse width (60 – 200 ns) or the laser power (0.1 – 1.09%) was changed for the individual acquisitions.

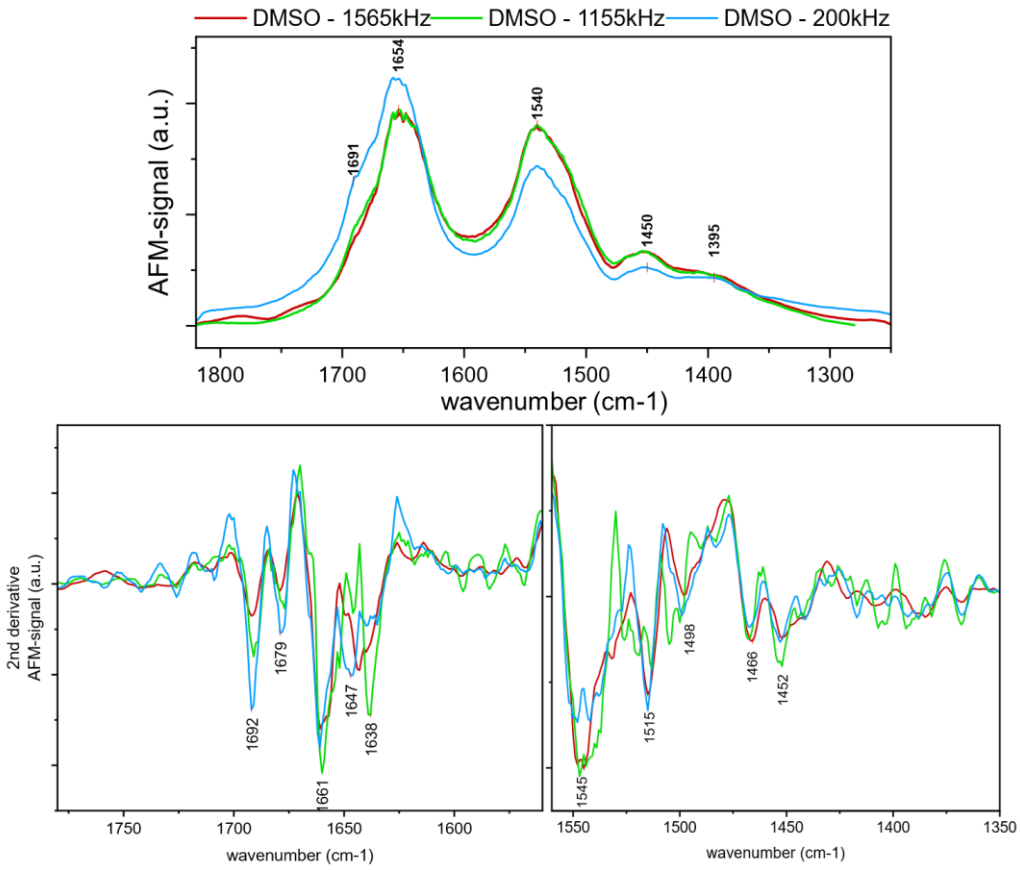

Supplemental Material 5: Average spectra of DMSO-treated Jurkat cells

Mean averages of multiple local spectra on various cell positions for the pulse rate 200kHz, 1155kHz and 1565kHz, using 100ns pulse width on a DMSO-incubated Jurkat cell are on display. While the averages of 1155 kHz and 1565 kHz are almost identical, the averages of 200 kHz deviate primarily regarding the amide I and II band ratio. The 2nd derivative displays constant positions of the individual bands. Deviations between the pulse rates occur especially regarding the band shoulders of the amide I (1647-1638 cm-1) and amide II (1515-1498 cm-1) bands. A broad band was identified for 1565 kHz between 1730 – 1750 kHz.

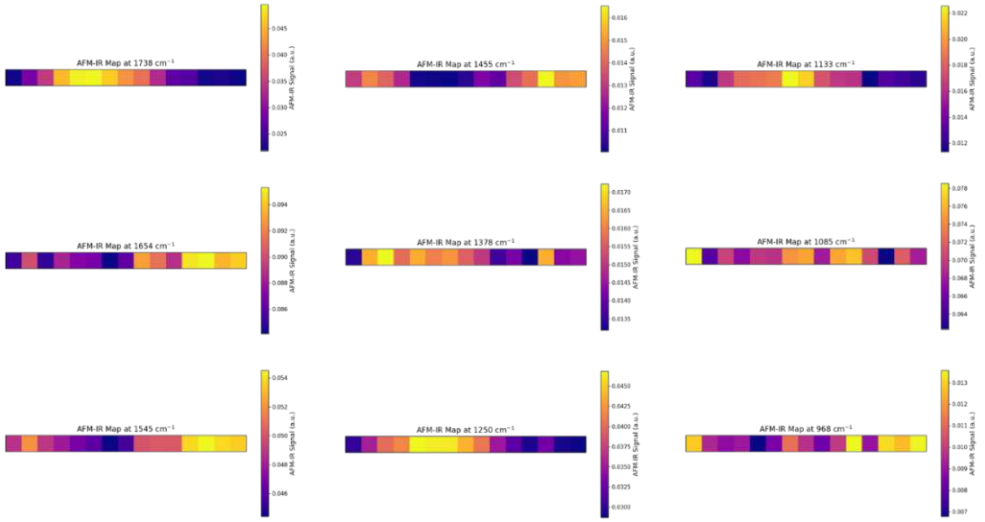

Supplemental Material 6: Hyperspectra of significant bands of an ICON-IR Line Array (Jurkat RSL3) over hotpot displaying a pronounced carbonyl ester band (1740 cm-1)